



HAL
open science

Three-dimensional Polarized Light Imaging: Towards Multiscale and Multimodal Analysis with Diffusion Magnetic Resonance Imaging

Abib Alimi

► **To cite this version:**

Abib Alimi. Three-dimensional Polarized Light Imaging: Towards Multiscale and Multimodal Analysis with Diffusion Magnetic Resonance Imaging. Medical Imaging. Inria Sophia Antipolis - Méditerranée, Université Côte d'Azur, 2020. English. NNT: . tel-03078802

HAL Id: tel-03078802

<https://inria.hal.science/tel-03078802>

Submitted on 16 Dec 2020

HAL is a multi-disciplinary open access archive for the deposit and dissemination of scientific research documents, whether they are published or not. The documents may come from teaching and research institutions in France or abroad, or from public or private research centers.

L'archive ouverte pluridisciplinaire **HAL**, est destinée au dépôt et à la diffusion de documents scientifiques de niveau recherche, publiés ou non, émanant des établissements d'enseignement et de recherche français ou étrangers, des laboratoires publics ou privés.

PHD THESIS

Three-dimensional Polarized Light Imaging: Towards Multiscale and Multimodal Analysis with Diffusion Magnetic Resonance Imaging

Abib Olushola Yessouffou ALIMI

Inria Sophia Antipolis – Méditerranée, Athena Project Team

**Submitted in partial fulfillment
of the requirements for the degree
of Doctor of Science Specialized in
Automatic, Signal and Image Processing
of the** Université Côte d'Azur

Advisor : Rachid Deriche
Co-advisor: Samuel Deslauriers-Gauthier

Tentative date of defense :
27/05/2020

In front of a Jury composed of:

Rachid Deriche, Inria Research Director, Inria
Sophia Antipolis - Thesis Advisor
Samuel Deslauriers-Gauthier, Inria Sophia
Antipolis - Thesis Co-advisor
Gloria Menegaz, Professor, Università di Verona,
Italia - Reviewer
Théodore Papadopoulo, Inria Research Director,
Inria Sophia Antipolis - Examiner
Ragini Verma , Professor, SBIA, University of
Pennsylvania, USA - Examiner
Yeumin Zhu, CNRS Research Director, CREATIS
Lab, INSA Lyon - Reviewer



Abstract

Diffusion Magnetic Resonance Imaging (dMRI) is the only non-invasive and in-vivo imaging modality able to provide human brain structural connectivity information. This is done via an estimation of the fiber orientation distribution (FOD) of white matter and dMRI tractography. In this thesis, three-dimensional Polarized Light Imaging (3D-PLI) is investigated and, thanks to its high spatial resolution, is presented as a complementary and potential technique for validation and guidance of dMRI fiber orientation estimates and tracking. The main goal of this work is, thus, to propose a strategy to close the resolution gap between dMRI and 3D-PLI and to investigate metrics for their quantitative comparison and, henceforth, to pave the way for multiscale and multimodal image analysis.

Contributions in this thesis are manifold. First, we study the 3D-PLI fiber orientation and propose a method to disentangle the sign ambiguity of its inclination angle for an accurate determination of the 3D orientation. Second, we introduce an analytical and fast technique to compute the FOD from microscopic 3D-PLI orientation estimates to the meso- or macroscopic dimensions of dMRI. Third, we perform tractography at multiple scales from 3D-PLI human brain data to demonstrate the preservation of the fiber tracts architecture regardless of the decrease in resolution. Finally, we investigate how these obtained tractograms can be inspected using homology theory for a quantitative evaluation between them. Overall, we develop original and efficient dMRI and 3D-PLI methods, validate on both synthetic and human data and lay the foundations for multiscale and multimodal studies between dMRI and 3D-PLI.

Keywords: 3D-PLI, polarized light imaging, diffusion MRI, fiber orientation distribution, tractography.



Résumé

L’Imagerie par Résonance Magnétique pondérée en diffusion (IRMd) est la seule modalité in-vivo et non invasive offrant des informations sur la connectivité structurelle du cerveau humain. Cela est effectué via l’estimation de la distribution des orientations de fibres (FOD) de la matière blanche et leur suivi ou tractographie. Dans cette thèse, l’Imagerie tridimensionnelle en Lumière Polarisée (3D-PLI) est, grâce à sa haute résolution, considérée comme une potentielle technique complémentaire et de validation de l’estimation et du suivi des orientations de fibres par l’IRMd. Ainsi, notre travail a pour but principal de combler l’écart de résolution et d’étudier des critères de comparaison quantitative entre l’IRMd et la 3D-PLI pour ainsi ouvrir la voie à une analyse multi-modale et multi-échelle.

Nos contributions sont multiples. D’abord, nous étudions l’orientation des fibres produites par 3D-PLI et proposons une méthode pour lever l’ambiguïté du signe de l’inclinaison pour une estimation plus précise. Puis, nous développons une méthode analytique de calcul de la FOD des mesures microscopiques de 3D-PLI à la résolution meso- ou macroscopique de l’IRMd. Ensuite, à partir des données PLI du cerveau, nous effectuons la tractographie à diverses échelles et montrons la conservation de l’architecture structurelle des fibres malgré la baisse de résolution. Enfin, nous nous intéressons à la théorie de l’homologie en vue d’évaluation quantitative des résultats de tractographie. En somme, nous développons des méthodes en IRMd et 3D-PLI, et les validons sur des données synthétiques et réelles tout en établissant les bases d’études multi-échelles et multi-modales entre IRMd et 3D-PLI.

Mots-clés: 3D-PLI, imagerie en lumière polarisée, IRM de diffusion, distribution des orientations de fibres, tractographie.

Acknowledgements

This work was partly supported by ANR "MOSIFAH" under ANR-13-MONU-0009-01, the ERC under the European Union's Horizon 2020 research and innovation program (ERC Advanced Grant agreement No 694665:CoBCoM)

We gratefully acknowledge professor Markus Axer and his group for providing the brain 3D-PLI data and the computing time granted through JARA-HPC on the supercomputer *JURECA* ([Jülich Supercomputing Centre, 2016](#)) at Forschungszentrum Jülich.



Contents

I	Introduction	19
1	Introduction	21
II	Background	25
2	Diffusion Magnetic Resonance Imaging	27
2.1	Principles of Diffusion MRI	27
2.1.1	Diffusion Process, and Gradient Sequence	27
2.1.2	Diffusion Weighted Imaging, Apparent Diffusion Coefficient	28
2.1.3	Ensemble Average Propagator	29
2.2	Local Fiber Orientation Estimation	30
2.2.1	Diffusion Tensor	30
2.2.2	Diffusion ODF	32
2.2.3	Fiber ODF	33
2.3	Fiber Tractography	34
2.3.1	Principles and Technical Considerations	34
2.3.2	Fiber-tracking Algorithms	35
2.3.3	Limitations	35
3	Three-Dimensional Polarized Light Imaging	37
3.1	Polarization Optics	37
3.1.1	Polarization of Light	37
3.1.2	Birefringence	38
3.2	Polarimetric Measurements	40
3.2.1	(Brain) Tissue Preparation	40
3.2.2	Measurement Setup	41
3.3	3D-PLI Signal Analysis	42
3.3.1	Matrix Calculus	43
3.3.2	Application of Müller-Stoke Calculus	44
3.3.3	Fourier Analysis of the Signal	45

III Contributions	49
4 On 3D-PLI Inclination Sign Ambiguity	51
4.1 Introduction	51
4.1.1 3D-PLI on Human Heart	51
4.1.2 Inclination Sign Estimation	52
4.1.3 Tilting Process	52
4.2 Method: Inclination Sign Restoration	53
4.2.1 Rudin-Osher-Fatemi model	54
4.2.2 ROF on sectional fiber orientation map	54
4.3 Results and discussion	55
4.3.1 On synthetic data	55
4.3.2 On human heart data	56
4.4 Conclusion	57
5 Analytical Fiber Orientation Distribution in 3D-PLI	59
5.1 Introduction	59
5.2 Analytical FOD in 3D-PLI	60
5.2.1 Spherical Harmonics	61
5.2.2 Analytical Fiber Orientation Distribution	61
5.3 Methods	63
5.3.1 Datasets Description	63
5.3.2 Performance Evaluation	64
5.4 Results	65
5.4.1 Simulations	65
5.4.2 Human Brain Data	67
5.5 Discussion and Conclusion	70
6 Fiber ODF methods in 3D-PLI: performance assessment	75
6.1 Introduction	75
6.2 Reconstruction Methods	76
6.3 Performance Assessment	77
6.3.1 Synthetic Data Experiments	77
6.3.2 Human Brain Data Experiments	79
6.4 Results	79
6.4.1 Single Fiber Orientation	79
6.4.2 Crossing Fiber Orientations	80
6.4.3 Computational Runtimes	82
6.4.4 Brain Deep White Matter	83
6.5 Discussion and Conclusion	84

7	Multiscale Analysis: bridging the diffusion MRI–3D-PLI resolution gap	89
7.1	Introduction	89
7.2	Methods	90
7.2.1	Analytical FOD	90
7.2.2	Multi-scale fiber-tracking	90
7.2.3	Homology analysis	91
7.2.4	Human brain dataset	92
7.3	Results and Discussion	92
7.4	Conclusion	94
IV	Conclusion	95
8	Conclusion	97
	Appendices	99
A	Regularizing the pliODF	101
B	Synthetic Data Generation	103
C	Publications	105

List of Figures

2.1	Pulsed Gradient Spin-Echo (PGSE) sequence introduced by Stejskal and Tanner (Stejskal and Tanner, 1965). Image taken from (Johansen-Berg and Behrens, 2013).	28
2.2	Diffusion tensor representation from (Descoteaux, 2008)	31
2.3	60° fibre crossing configuration visualized using dODF and fODF profiles. Taken from (Dell’Acqua and Tournier, 2019).	33
3.1	Unpolarized light is transmitted through a polaroid filter to emerge as polarized light with vibrations in a single plane.	38
3.2	Rotational index ellipsoid of a positive uniaxial birefringent material. Depending on the orientation of the optic axis relative to the direction of propagation \mathbf{k} , the refractive index $n_e(\theta)$ of the extraordinary ray varies.	39
3.3	Unpolarized light beam traversing a birefringent medium is split into an ordinary ray in blue and an extraordinary ray in red with orthogonal linear polarization states. Adapted from (Hecht, 1998).	39
3.4	The human brain sectioning. Anatomical planes and directions along which the brain is sliced. Taken from (Menzel, 2018).	41
3.5	(a) Schematic of the Large-Area Polarimeter used in the INM-1 laboratory, Jülich, Germany: the specimen stage containing a brain tissue slice can be tilted around two axes and is placed between the pair of crossed linear polarizers and a quarter-wave retarder ($\lambda/4$ -retarder). During a measurement, the filters are rotated by discrete rotation angles ρ . (b, c) Measured sinusoidal signal whose phase φ (in red) correlates with the in-plane direction and amplitude with the out-of-plane inclination α (in blue) of the prevailing fiber orientation. Image adapted from (Menzel, 2018).	42
3.6	Parameter maps of a coronal section from the right hemisphere of the human brain imaged at $64 \times 64 \times 70 \mu m^3$ resolution: (a) normalized transmittance $I_N = I(\rho)/I_T$, (b) in-plane direction angle φ , (c) retardation r , and (d) out-of-plane inclination angle α	47

4.1	An example of simulated FOM enabling a clear vector visualization of the 3D fiber orientation vectors in a histological tissue slice. Adapted from (Dohmen, 2013)	53
4.2	Percentage of wrongly estimated inclination signs as noise increases. Each data point corresponds to the mean and standard deviation over 100 noisy realizations.	56
4.3	Inclination angle maps of a coronal ventricular slice: (A) Absolute inclination. (B) and (D) Signed α from tilting measurements. (C) and (E) Signed α after TV restoration. The white rectangle represents the region of interest displayed in (D) and (E). The angle is coded in gray scale (0° to 90°) in (A) and in false color (-90° to 90°) otherwise. The best results are achieved by the extended TV algorithm on these real data.	57
5.1	Analytical FOD reconstruction: (A) Super-voxel (SV) definition from high-resolution 3D-PLI data fiber orientation map, image taken from (Axer et al., 2016), (B) each orientation in the SV is modeled as Dirac, and aFOD as sum of these Diracs on the unit sphere, and (C) SH expansion of the aFOD in the defined SV.	62
5.2	Angular resolution of the computed aFOD as a function of the spherical harmonics order L_{max} in noise-free simulations.	65
5.3	Recovered orientations (α, φ) of 2 crossing fiber bundles from 100 noisy simulations in black crosses. The red dots represent the ground truth. The SH order is $L_{max} = 8$	67
5.4	Stratum sagittale (SS) in deep WM described by fiber ODFs at different super-voxel sizes i.e. at different spatial resolutions. (A) pictures a high-resolution retardation map while (B) to (D) show the SS at SV size of 5, 10 and 25 isotropic native voxels, respectively. The global fiber organization is preserved through the scales. FODs overlay a recomputed retardation map and are colour-coded according to their local orientation (red: left-right; green: anterior-posterior; blue: inferior-superior). The white rectangular RIO is zoomed in on Fig. 5.6.	68
5.5	FOD map of U-shaped fibers connecting adjacent gyri at varying resolutions from (B) to (D) with a high-resolution retardation map displayed in (A). The global fiber organization is preserved through the scales. FODs overlay a recomputed retardation map and are colour-coded according to their local orientation (red: left-right; green: anterior-posterior; blue: inferior-superior).	69

5.6 Zoom in on the white rectangle of Fig. 5.4: details about the layers of the stratum sagittale. The spatial resolution is $128 \times 128 \times 140 \mu m^3$ in (A), $320 \times 320 \times 350 \mu m^3$ in (B) and $640 \times 640 \times 700 \mu m^3$ in (C). The blue and the red arrows point the thinner and the more pronounced layers of the SS, respectively. By reducing the scale, the thinner layer form crossing FODs with a vertical fiber bundle. 70

6.1 pliODF generation steps. (A) High-resolution FOM is divided into regular domains or super-voxels (SV). (B) Then for each SV, a normalized directional histogram is created on the unit sphere with a discretized binning. (C) Finally, the directional histogram is approximated using a spherical harmonics expansion to give pliODFs with features dependent on L_{max} . Step (A) is common to both pliODF and aFOD. Image taken from (Axer et al., 2016). 77

6.2 (A) 3D visualization of the simulated fiber bundles crossing at angle $X = 90^\circ$. (B)-(D) The resulting Fiber Orientation Maps of 3D-PLI simulations through $60 \mu m$ sections with a crossing at $X = 30^\circ, 60^\circ$ and 90° , respectively. 78

6.3 Angular precision ϵ of single fiber ODFs as a function of the directional histogram bin size, in degrees. (A)–(C) For decreasing bin size, the ϵ of pliODF (red dotted line) converges to the constant $\epsilon < 1^\circ$ of aFOD, in green horizontal line. At $L_{max} = 12$, when bin size is very small, for both fODFs $\epsilon < 1^\circ$, this is illustrated in (D) where the blue square in (C) is zoomed in. 80

6.4 Effects of SH L_{max} on the angular resolution of the aFOD and the pliODF with bin size 3.6° estimated at different crossing configurations. 82

6.5 Angular precision of the fODF reconstructed at varying SH L_{max} from different crossing fiber configurations X 83

6.6 Stratum sagittale (SS) in deep WM described by fODF at different super-voxel sizes i.e. at different spatial resolutions. (A) pictures a high-resolution retardation map while (B) to (D) show the SS at SV sizes of 5 and 50 isotropic native voxels. The global fiber organization is preserved through the scales. fODFs are colour-coded according to their local orientation (red: left-right; green: anterior-posterior; blue: inferior-superior). The white square RIO in (D) is zoomed in (E) to present a voxel containing a crossing fiber ODF computed at different SH L_{max} 85

7.1 The number of connected components i.e. the zeroth Betti (β_0) in red and the number of holes i.e. the first Betti (β_1) in green are encoded in barcodes for varying thresholds (x-axis). Each threshold level, represented by a vertical dashed line, indicates the level of granulation of the graph illustrated in the square at its top. The barcodes are equivalent to the curves in Fig. 7.4. In the remainder of the analysis, the zeroth Betti β_0 and the threshold are the parameters of interest. Image taken from (Hylton et al., 2019). 91

7.2 Panels (A) to (C) illustrate the streamlines passing through the central coronal slice of the studied dataset with the usual orientation-based colouring. It is possible to notice the different white matter structures that are generated at different SV sizes or resolutions. The figure on the top left is the transmittance image resulting from 3D-PLI analysis and the one on the bottom left is the used white matter mask 92

7.3 The first row shows the weighted connectivity matrices corresponding to the tractograms obtained at the three studied resolutions or super-voxel sizes SV_5 , SV_{10} and SV_{25} . The second row shows the sparsity pattern of the connectomes from the first row. 93

7.4 The β_0 curves associated to the connectomes obtained at specific SV sizes. The value of the three curves at zero threshold is 67 for the resolution corresponding to SV_5 , 64 for SV_{10} and 63 for SV_{25} . The fact that the three curves terminate at different thresholds occurs because the maximal entry in the respective connectivity matrix is different for each connectome. . . . 94

List of Tables

- 5.1 The angular resolution improves with L_{max} in noise-free setting and the precision is generally high i.e. low angular deviation. 66
- 5.2 Angular resolution and associated mean and standard deviation angular precision in relation to L_{max} in noisy data. 66
- 6.1 Single fiber angular precision ϵ in degrees [$^\circ$] as a function of L_{max} . For aFODs ϵ is always $< 1^\circ$, and the difference with ϵ of pliODFs is not very significant with regard to the considered bin sizes. 81
- 6.2 Imaging spatial resolutions resulting from super-voxels. 83
- 6.3 A comparison of runtime measurements in minutes:seconds. All the analytical FODs are run in the order of seconds regardless of the super-voxel size and the SH L_{max} . pliODF takes minutes to run in small sized SV and a few seconds when the resolution is coarser. The execution time generally increases with L_{max} 84
- 7.1 Imaging spatial resolutions: from 3D-PLI's micrometer to diffusion MRI's millimeters by varying super-voxel dimensions. The tissue consists of 50 coronal sections, for a total of $1350 \times 1950 \times 50$ native voxels. 90

Part I

Introduction

Chapter 1

Introduction

Context

Brain and cardiac disorders are very common in the world and their treatment is very costly. In order to understand and cure these disorders, it is fundamentally compulsory to develop techniques which enable a better understanding of the structure as well as the function of the brain white matter and the cardiac myocardium. To this end, state-of-the-art imaging modalities which allow for a thorough analysis of these fibrous tissues on different scales are necessary. It is important to note that the first techniques proposed were based on dissection and measurements from stained histological sections of the tissues (Sachs, 1892; Gray, 1878). Most recently, (millimeter resolution) Diffusion Magnetic Resonance Imaging (MRI) (Le Bihan et al., 1986; Basser et al., 1994; Tuch et al., 2002; Jones, 2010; Hagmann et al., 2006; Tournier, 2019; Leemans, 2019) has been introduced. Diffusion MRI is a promising technique which utilizes water diffusion as a probe to assess fiber pathways in tissues such as the white matter or the myocardium, *in vivo* and *non-invasively* and to infer their respective connectivity. However, it has a relatively low spatial resolution and since no *in vivo* ground-truth of the brain (Maier-Hein et al., 2017) or the cardiac fibers is available, it is a challenging task to validate or know how reliably the reconstructed fiber pathways reflect the actual architecture of the fibers and their properties in these tissues.

Therefore, our research work investigates three-dimensional Polarized Light Imaging (3D-PLI) which was presented by Axer et al. (2011a) as a *potential candidate* for the validation of diffusion MRI results. We are here interested in the potential of 3D-PLI in the context of fiber orientation estimates and fiber tractography. 3D-PLI is an optical imaging approach that measures the birefringence property of postmortem fibrous tissues e.g. human brain or myocardium, in order to map their spatial fiber architecture. This method requires no staining of histological sections to provide quantitative measurements of 3D fiber orientations at micrometer scale.

The main goal of this thesis, therefore, is to propose strategies to close the spatial

resolution gap between diffusion MRI and 3D-PLI and to investigate metrics for their quantitative comparison in order to pave the way for a multiscale and multimodal imaging analysis.

Contributions

This thesis deals primarily with the human brain in terms of experimental dataset. That is, we focus on diffusion MRI and 3D-PLI applied to the human brain, unless specified otherwise. The main contributions of this thesis are detailed below.

First, in 3D-PLI the 3D fiber orientation in each voxel is defined by its spherical coordinates: the direction and the inclination angles. Since its sign is unknown, inclination angle presents a sign ambiguity. As a first and necessary contribution, we propose a method based on partial differential equations (PDE) to reduce the noise from tilted measurements and disentangle this ambiguity for a more precise reconstruction and interpretation of the 3D-PLI fiber orientation.

Second, for multimodal studies between diffusion MRI and 3D-PLI, it is crucial to develop common tools for analysis at different spatial resolutions. The fiber orientation distribution is a perfect means for this purpose. Here, we introduce an analytical and fast method to compute fiber orientation distributions (FOD) from microscopic 3D-PLI orientation estimates to the meso- or macroscopic scales of diffusion MRI.

Third, we propose a thorough comparative study between our analytical FOD –aFOD– to the empirically estimated pliODF. This demonstrates the ability of our aFOD to give the exact solution while outperforming the 3D-PLI state-of-the-art methods in terms of angular resolution and precision and computational runtimes and efficiency.

Then, we carry out tractography application for our aFOD at multiple scales from 3D-PLI human brain data. This study demonstrates the preservation of the architectural organization of the white matter fiber tracts regardless of the decrease in spatial resolution and suggests possible contrasting with diffusion MRI-based tractograms.

Finally, we investigate how the previously obtained 3D-PLI white matter tractograms can be inspected using homology theory. We compute topological invariants such as the number connected components out of the generated tractograms to perform a quantitative evaluation between them at different scales.

Overall, we develop methods via 3D-PLI to carry out at different resolutions the analysis of the brain/heart tissues and therefore lay the foundations for multiscale and multimodal studies between diffusion MRI and 3D-PLI.

Organization

The remainder of this thesis is organized as follows.

Chapter 2 gives the background information about diffusion MRI. First are described the physical principles which govern diffusion in materials, with a special emphasis on diffusion MRI in biological tissues. Then we present diffusion models to estimate the local fiber orientation, before their integration to infer global structural information of the brain via tractography.

Chapter 3 introduces 3D-PLI. It starts with the definition of polarization and birefringence, then presents how the postmortem tissue is prepared and the PLI signal measured. Finally, it describes the approach to analyze the signal in order to reconstruct the 3D microscopic fiber orientation vector.

Chapter 4, which constitutes our first contribution, deals with the inclination angle sign ambiguity in 3D-PLI, with an application on human heart data. The tilting setup is introduced to help recover the sign and then the PDE-based method is used to disentangle the inclination sign ambiguity both on synthetic and human heart datasets.

In Chapter 5, the analytical FOD reconstruction method is introduced. The method is presented after a brief review on the spherical harmonics which basis is used to represent the FOD. The performances of our method are then assessed on both simulated and human brain datasets and the results are finally discussed.

Chapter 6 presents a comparative study between our analytical FOD computation technique with state-of-the-art discrete pliODF method which is briefly described before. Here, both a highly realistic synthetic dataset as well as human brain 3D-PLI data are used to evaluate the performance of the algorithms.

In Chapter 7, fiber tractography is performed using our analytical FOD solution and applied on the human brain data at different spatial resolutions. This study shows an accurate reconstruction of the white matter tracts and the conservation of their global organization in the occipital lobe. Moreover, connectivity matrices are generated and homology theory used to quantify the results of multi-scale fiber-tracking.

The thesis is finally concluded with a general discussion of the results and a presentation of future directions and appendices.

Part II

Background

Chapter 2

Diffusion Magnetic Resonance Imaging

Diffusion magnetic resonance imaging (MRI) constitutes a powerful *in vivo* means to investigate the architecture of fibrous tissues such as the brain white matter or the cardiac muscle, *non-invasively*. This chapter presents the principles of diffusion MRI, its methods to represent the local fiber orientation information and to infer the overall structural connectivity of the studied tissue, more specifically, the brain white matter.

2.1 Principles of Diffusion MRI

In this section are described the physical principles which govern diffusion in materials with a special emphasis on diffusion MRI in biological tissues.

2.1.1 Diffusion Process, and Gradient Sequence

Diffusion is the natural random thermal motion, the so-called *Brownian motion*, which molecular spins undergo at temperatures above absolute zero. It gives rise to a mass transport without requiring bulk motion. This random process is described as a statistical process since only the macroscopic ensemble-averaged behaviour of a large number of spins is observable in a sample e.g. an imaging voxel at a given resolution. In 1905, [Einstein \(1905, 1956\)](#) showed that the *mean-squared displacement* of spins “freely” travelling a net distance r is proportional to the observation time τ as:

$$\langle \mathbf{r}^T \mathbf{r} \rangle = 6D\tau, \quad (2.1)$$

where D denotes the *diffusion coefficient* and $\mathbf{r} = r\mathbf{u}$ with \mathbf{u} a 3×1 vector indicating the direction of displacement. The diffusion coefficient or *diffusivity* is a measure of spins’ mobility. In free diffusion, D is a constant scalar which is direction-independent. Conversely, in cases where the medium is anisotropic, D is spatially and directionally variable and can be generalized to the so-called *diffusion tensor*.

Note that in biological tissues, the diffusion of water molecules is a very complex process as the movement of the spins may be hindered or restricted by the surrounding environment e.g. cell membranes, microtubules etc. Consequently, [Le Bihan et al. \(1986\)](#) suggested to replace the physical diffusion coefficient D with a global statistical quantity, the *Apparent Diffusion Coefficient* (ADC) presented in the next section. Using diffusion MRI, it becomes possible to probe the tissue microstructure, particularly the fiber orientation information.

Pulsed Gradient Spin Echo The pulsed gradient spin echo (PGSE) sequence pioneered by [Stejskal and Tanner \(1965\)](#) is the most prevalent imaging sequence used in diffusion MRI, illustrated in Fig. 2.1. PGSE applies two gradient pulses of strength $g = \|\mathbf{G}\|$ in T/m, length δ (s), and separated by a time Δ (s), on either side of the refocusing 180° radio-frequency (RF) pulse. The excitation 90° RF pulse tips the spins in the plane transverse to the magnetic field of the scanner and the first gradient pulse causes a phase accumulation. After the time Δ , and after the refocusing RF pulse, the second gradient pulse cancels the phase accumulation of the stationary spins. However, spins which diffused during Δ will remain out of phase and lose signal.

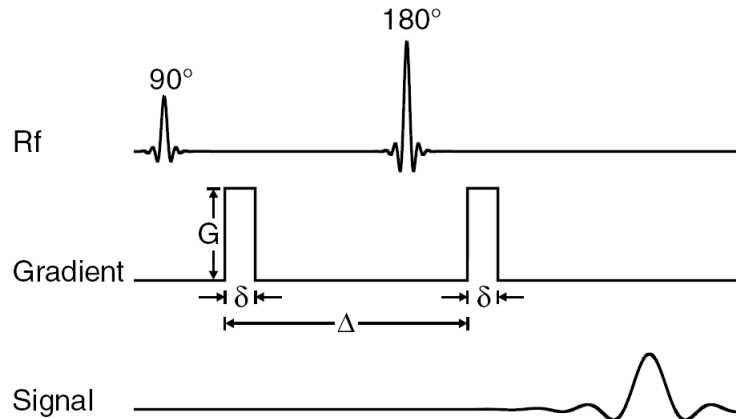


Figure 2.1: Pulsed Gradient Spin-Echo (PGSE) sequence introduced by Stejskal and Tanner ([Stejskal and Tanner, 1965](#)). Image taken from ([Johansen-Berg and Behrens, 2013](#)).

2.1.2 Diffusion Weighted Imaging, Apparent Diffusion Coefficient

The resulting PSGE signal is the *diffusion weighted imaging* (DWI) signal. The diffusion-weighting along the applied gradient direction \mathbf{u} , is encoded by the *b-value* introduced by Le Bihan¹ *et al.* in ([Le Bihan et al., 1986](#)):

$$b = \delta^2 \gamma^2 g^2 \left(\Delta - \frac{\delta}{3} \right) \quad (2.2)$$

¹Le Bihan *et al.* introduced the so-called b-value but it was already present in the seminal paper by ([Stejskal and Tanner, 1965](#)).

where γ is the nuclear gyro-magnetic ratio of water protons ^1H , measured in $\text{rad}\cdot(\text{sT})^{-1}$. The b-value is measured in s/mm^2 . The first *in vivo* diffusion MRI images of the human brain was acquired in 1986 by [Le Bihan et al. \(1986\)](#).

Using PGSE, the diffusion-weighted *signal attenuation* $E(b)$ is given by the Stejskal-Tanner equation ([Stejskal and Tanner, 1965](#)):

$$E(b) = \frac{S(b)}{S_0} = \exp(-bD) \quad (2.3)$$

where $S(b)$ denotes the diffusion-weighted signal, $S_0 = S(0)$ the image acquired without diffusion-weighting and D is known as the *Apparent Diffusion Coefficient* (ADC) which is informative about the property of the surrounding tissues.

In a medium where diffusion is free, the ADC is a scalar coefficient quantity which does not depend on the gradient direction \mathbf{u} . Conversely, in biological tissues where diffusion is anisotropic i.e. water spins are more presumably free along the direction of fibers than across them, the ADC relies not only on the diffusion-sensitizing gradient pulse $\mathbf{G} = g\mathbf{u}$ ([Moseley et al., 1990](#); [Douek et al., 1991](#)) but also on experimental parameters such as the voxel size and the diffusion time ([Le Bihan and Johansen-Berg, 2012](#)). In order to represent the directional anisotropy of diffusion in the brain white matter (WM) where axons form coherent fiber bundles running in parallel, [Basser et al. \(1994\)](#) introduced the diffusion tensor to model the ADC as,

$$D(\mathbf{u}) = \mathbf{u}^T \mathbf{D} \mathbf{u} \quad (2.4)$$

where \mathbf{D} is the diffusion tensor which leads to the *Diffusion Tensor Imaging* method presented later in Sect. 2.2.1.

2.1.3 Ensemble Average Propagator

Under the narrow pulse approximation which assumes that the gradient pulses are short enough $\delta \ll \Delta$ and that diffusion of water molecules over δ is neglected, the PGSE signal is related to the *ensemble average diffusion propagator* EAP via a Fourier relationship which is inverted to yield ([Stejskal and Tanner, 1965](#); [Stejskal, 1965](#); [Callaghan, 1993](#)),

$$P(\mathbf{r}) = \int_{\mathbf{q} \in \mathbb{R}^3} E(\mathbf{q}) \exp(2i\pi\mathbf{q} \cdot \mathbf{r}) d\mathbf{q} \quad (2.5)$$

where the EAP $P(\mathbf{r})$ denotes the probability of water molecules to undergo a net displacement \mathbf{r} in 3D space, $\mathbf{q} = (2\pi)^{-1}\gamma\delta\mathbf{G}$ the reciprocal space vector which gives rise to *q-space imaging* ([Callaghan et al., 1988](#); [Callaghan, 1993](#)) and $E(\mathbf{q}) = S(\mathbf{q})/S_0$ the normalized signal attenuation. It is then possible to represent the diffusion weighting factor or b-value (b) by combining \mathbf{q} and τ ,

$$b = 4\pi^2\tau q^2 \quad (2.6)$$

with $\tau = \Delta - \delta/3$ being the effective diffusion time ([Le Bihan et al., 1986](#); [Basser et al., 1994](#)). Note that in practice this PGSE approximation is never satisfied. However, if the number of samples in the q -space is large enough, the EAP can be derived using Eq. (2.5).

From the EAP, it can be extracted different features or microstructure indices which enable to characterize the degree of restriction of water molecules and therefore provide information about the pore shape e.g. the return-to-origine-probability (RTOP) (Özarslan et al., 2013; Fick et al., 2016; Alimi et al., 2018a). In the following sections, we will only focus on one of the most important EAP-based feature, that is, the Orientation Distribution Function to represent the local diffusion information using different reconstruction methods.

2.2 Local Fiber Orientation Estimation

In diffusion MRI, the very first description of local information was given by the ADC, which is so far one of the most common applications of diffusion in the brain, particularly for imaging of acute ischemic stroke where it gives a very crucial imaging contrast (MacIntosh et al., 2013). In this thesis, we are more interested in the modeling of the structural architecture of fibrous tissues, therefore, approaches to characterize the local fiber orientation information are of great importance. Thus, our focus will be, here, on the Diffusion Tensor (DT) and the Orientation Distribution Functions (ODF).

2.2.1 Diffusion Tensor

Diffusion Tensor Imaging (DTI) was introduced as a (simple) extension of the ADC model to fully describe the diffusion directional anisotropy in the brain (Basser et al., 1994), assuming 3D Gaussian displacement of water spins. Consequently, the ADC becomes $D(\mathbf{u}) = \mathbf{u}^T \mathbf{D} \mathbf{u}$ and the Stejskal-Tanner equation,

$$E(b) = \exp(-b\mathbf{u}^T \mathbf{D} \mathbf{u}) \quad (2.7)$$

where \mathbf{D} is the diffusion tensor, a 3×3 symmetric positive definite matrix and \mathbf{u} is the gradient direction. \mathbf{D} can be eigen-decomposed into three positive eigenvalues with associated eigenvectors. It is often represented as an ellipsoid whose axes are aligned with the eigenvectors of the tensor, with lengths corresponding to associate eigenvalues, as illustrated in Fig. 2.2.

Estimation and indices The diffusion tensor being symmetric, at least six DW images (from non-collinear directions) and one baseline image ($b = 0$ s/mm²) are required to estimate its unknown coefficients in each voxel, via simple least squares or weighted least squares approaches (Basser et al., 1994). DTI provides indices which are now acknowledged, (one of) the most commonly known and used being the *fractional anisotropy* (FA),

$$FA = \left(\frac{1}{2} \frac{(\lambda_1 - \lambda_2)^2 + (\lambda_1 - \lambda_3)^2 + (\lambda_2 - \lambda_3)^2}{\lambda_1^2 + \lambda_2^2 + \lambda_3^2} \right)^{1/2} \in [0, 1] \quad (2.8)$$

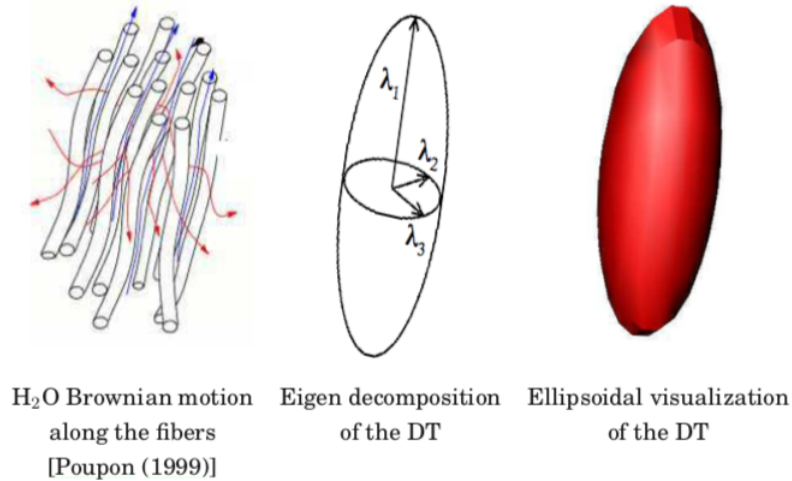


Figure 2.2: Diffusion tensor representation from (Descoteaux, 2008)

with $\lambda_1 \geq \lambda_2 \geq \lambda_3$, the three eigenvalues of \mathbf{D} . FA is a measure of the degree of directional dependence of the diffusion tensor and has become the standard measure of anisotropy (Tournier, 2019). FA is high in voxels containing strongly aligned tissue fibers e.g. in brain WM. However, it is low in voxels with differently oriented fibers or where diffusion is isotropic e.g. in cerebrospinal fluid (CSF) and grey matter (GM). Another important index is the *principal direction of diffusion* (PDD) which is the primary eigenvector \mathbf{v}_1 indicating the orientation of the main axis of the tensor. It is assumed to be the direction of the WM fiber which is followed in DT-based fiber-tracking.

Applications and limitations DT is one of the main tool used in modern neuroimaging to extract orientational information non-invasively (Assaf et al., 2019) and it provides some (anisotropic) measures. However, their interpretation in region with different fiber orientations is problematic. The observed variations in FA in pathologies could be caused by many effects (Beaulieu, 2002). Moreover, DTI can estimate the principal fiber orientation via the PDD but fails to detect complex fiber configurations such as crossings which are present in about 90% of the brain WM (Jeurissen et al., 2013).

Such limitations have motivated the development of so-called “high-order” models for the estimation of multiple fiber orientations in a given voxel. Two main classes can be distinguished: methods based on \mathbf{q} -space, and methods based on mixture models. The former provides the *diffusion ODF* as we illustrate with Q-ball Imaging, and the latter gives the *fiber ODF* as showcased bellow by the Spherical Deconvolution technique.

2.2.2 Diffusion ODF

The first alternative methods to overcome the limitations of the DT attempt to recover the angular dependence of the EAP in order to estimate the *diffusion orientation distribution function* (dODF). The dODF is defined as the radial projection of the propagator and its peaks are assumed to correspond to the fiber orientations provided by the directions of highest spin displacement.

Diffusion Spectrum Imaging (DSI) is the earliest such technique, which densely samples the \mathbf{q} -space to measure crossing fibers (Wedeen et al., 2005). However, due to its long acquisition times, DSI is clinically impractical. Therefore, alternative methods are proposed with clinically feasible protocols. For instance, Q-ball Imaging (QBI) which relies on much less time-demanding high angular resolution diffusion imaging (HARDI) strategy (Tuch, 2004). QBI acquires data over a dense set of directions at a constant q -value or *single shell* to estimate the diffusion ODF.

Analytical QBI In the analytical formulation of QBI proposed by Descoteaux et al. (2007), the diffusion signal $E(\mathbf{u}, q)$ is modeled using a real symmetric *Spherical Harmonics* (SH) basis \hat{Y}_l^m of order l and phase factor m , as follows,

$$E(\mathbf{u}, q) = \sum_{l=0, \text{even}}^N \sum_{m=-l}^l c_{lm} \hat{Y}_l^m(\mathbf{u}) \quad (2.9)$$

with

$$\hat{Y}_l^m = \begin{cases} \sqrt{2} \cdot \text{Re}(Y_l^m), & \text{if } -l \leq m < 0 \\ Y_l^0, & \text{if } m = 0 \\ \sqrt{2} \cdot \text{Im}(Y_l^m), & \text{if } 0 < m \leq l \end{cases} \quad (2.10)$$

where $\text{Re}(\cdot)$ and $\text{Im}(\cdot)$ are the respective real and imaginary parts of Y_l^m which is the general SH basis defined in Sect. 5.2.1 and c_{lm} are the $N = (l+1)(l+2)/2$ SH coefficients calculated using Laplace-Beltrami regularization scheme in least square method (Descoteaux et al., 2007). They applied the Funk-Hecke theorem and showed that, by using the estimated c_{lm} coefficients, an approximate of the diffusion ODF Φ_{dODF} can be obtained analytically,

$$\Phi_{\text{dODF}}(\mathbf{u}) = \sum_{l=0}^N \sum_{m=-l}^l c_{lm} 2\pi P_l(0) \hat{Y}_l^m(\mathbf{u}) \quad (2.11)$$

with

$$P_l(0) = (-1)^{l/2} \frac{1 \cdot 3 \cdot 5 \cdots (l-1)}{2 \cdot 4 \cdot 6 \cdots (l)} \quad (2.12)$$

where $P_l(0)$ is the Legendre polynomial of order l evaluated at 0.

2.2.3 Fiber ODF

The other class of high-order methods rely on mixture models to recover the *fiber orientation distribution functions* (fODF) directly, unlike the \mathbf{q} -space methods, by assuming a model of the diffusion signal for a single fiber bundle (or the *fiber response function* in SD, see below). Different techniques have been proposed, but we will focus here on the Spherical Deconvolution (SD) (Tournier et al., 2004) approach which is today one of the main techniques to model multiple fiber populations in a voxel and for fiber-tracking as noted by Dell’Acqua and Tournier (2019) in a recent comprehensive review on SD.

SD techniques assume that, in a given voxel, the acquired DW signal $E(\mathbf{u})$ measured on a single shell is the convolution over the sphere of a (suitable) response function $R(\mathbf{w}^T \mathbf{u})$ with the fiber orientation distribution,

$$E(\mathbf{u}) = \int_{\mathbb{S}^2} \Phi_{FOD}(\mathbf{w}) R(\mathbf{w}^T \mathbf{u}) d\mathbf{w} \quad (2.13)$$

where $\Phi_{FOD}(\mathbf{w})$ is the *fiber orientation distribution* (FOD), a continuous representation of the fODF. The idea is then to invert the process through spherical deconvolution to extract an estimation of the full FOD in each voxel, regardless of the number of underlying fiber orientations. If the fiber response is known, it is possible to deconvolve the diffusion attenuation signal with the response function to reconstruct the fiber ODF.

In diffusion MRI, the most common techniques used to resolve this problem are Constrained Spherical Deconvolution (CSD) (Tournier et al., 2007) and Richardson-Lucy Spherical Deconvolution (RL-CSD) (Dell’Acqua et al., 2007).

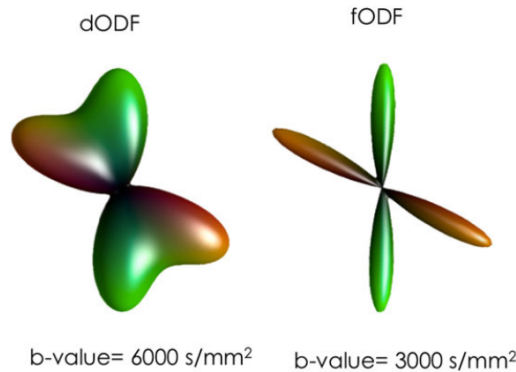


Figure 2.3: 60° fibre crossing configuration visualized using dODF and fODF profiles. Taken from (Dell’Acqua and Tournier, 2019).

SD techniques face a common criticism that is the response function may not be the same for all brain tissue types (Jeurissen et al., 2014). This has led to the extension of the approach for multi-shell data, allowing a fiber response and FOD to each brain tissue type (Jeurissen et al., 2014). Compared to the diffusion ODF methods, the SD approaches can resolve more acute crossing (Tournier et al., 2008) and the resulting fODF is sharper, see Fig. 2.3, and directly usable (and preferred) in fiber tractography (Jeurissen et al., 2019).

2.3 Fiber Tractography

Once the local fiber orientation is determined in each voxel, they are linked together to infer the global structure or connectivity in the brain via tractography (Mori and Van Zijl, 2002). Fiber tractography is able to delineate the WM fiber fascicles non-invasively, which makes it appealing for clinical applications, with great potential for neuroscience.

This section briefly presents the general principles and concepts of tractography and its limitations. For more comprehensive information about fiber tractography, the reader is referred to the works of Mori and Van Zijl (2002); Descoteaux et al. (2008) and to the recent review of Jeurissen et al. (2019) and the references therein.

2.3.1 Principles and Technical Considerations

Local fiber orientation To date, DT-based tractography is the most used method in clinical applications, specially in neurosurgery (Farquharson et al., 2013). However, diffusion MRI community has been promoting the use of “higher-order” models (Tournier et al., 2012), e.g. the FOD-based tractography, because of the aforementioned reasons in Sect. 2.2 and the more biologically plausible results given by the FOD (Farquharson et al., 2013; Jeurissen et al., 2013, 2019).

Seeding strategy Where do we start the streamline tracking? Streamline tractography algorithms start at *seed points* defining, in general, either a specific *region of interest* (ROI) or a *whole organ*. In both cases, the seeds are placed either in every voxel inside the volume or only on the surface (extremities) of the object e.g. the grey matter-white matter (GM-WM) interface in brain WM fiber tracking taking in to account anatomical constraints (Smith et al., 2012).

Streamline integration How do we step along fiber orientations in 3D space? Local information are linked together using mainly either first-order *Euler integration* scheme with constant step size or higher order *Runge-Kutta integration* method accounting for a varying step size. This results eventually in discrete measurements which are then interpolated into a continuous space via either *nearest-neighbor* (Mori et al., 1999) or *trilinear* (Jeurissen et al., 2013) interpolations algorithms.

Track termination When do we stop the streamlines? Appropriate termination of tracking process is problematic. However, some criteria still exist and the most commonly used are: a) use a mask and forbid streamlines to exit, b) apply a curvature threshold to keep the orientation of the streamlines spatially coherent and c) apply some anisotropy threshold to make sure streamlines are not propagating in isotropic tissue types, e.g. threshold the FA in tensor-based methods (Descoteaux et al., 2008); or the amplitude of the fODF (Tournier et al., 2010, 2012).

Acceptance criteria Do we accept or reject the streamline ? Most commonly used criteria are the *minimum track length* or *anatomical priors* (Smith et al., 2012) e.g. only accept streamlines/tracks which connect different GM regions of the brain (Girard et al., 2014).

2.3.2 Fiber-tracking Algorithms

The streamline is propagated in space using either a *deterministic* or a *probabilistic* approach. In deterministic streamlines tractography e.g. (Mori et al., 1999), the fibre orientation which is the most aligned with the previous direction is selected at each point and traced exactly. The same trajectory is generated in each run since uncertainties in the orientation, due to noise for example, are not accounted for. Oppositely, probabilistic streamlines tractography e.g. (Parker et al., 2003; Tournier et al., 2010) considers the uncertainty in the computed fibre orientations and randomly samples from the distributions along the trajectory. Thus, different trajectories are generated at each run.

2.3.3 Limitations

Streamline tractography faces some limitations (Descoteaux et al., 2008; Jeurissen et al., 2019). Indeed, most of the state-of-the-art algorithms generate more *false positive* fiber tracks than *true positive* ones in “whole-brain” tractography (Maier-Hein et al., 2017). Moreover, DT-based algorithms also tend to fail to identify actual connections, this is a *false negative* issue e.g. lateral portion of the cortico-spinal tract (Farquharson et al., 2013). Another issue is related to improper termination where the streamlines end e.g. in fluid-filled regions. Anatomically constrained tractography algorithms have been introduced to terminate the tracks at the GM-WM interface (Smith et al., 2012).

Chapter 3

Three-Dimensional Polarized Light Imaging

Three-dimensional Polarized light Imaging (3D-PLI) is a micrometer resolution optical imaging technique which utilizes *polarized light* to measure the *birefringence* of materials e.g. brain tissue and myocardium, in order to map their structural architecture. This chapter introduces 3D-PLI by presenting the optics of polarization, the polarimetric measurements (performed on the brain, specifically) and the signal analysis to derive the fiber orientation vector.

3.1 Polarization Optics

3D-PLI utilizes the birefringence of unstained histological slices of *fibrous* tissue in order to map its fiber architecture. This section introduces *polarization* of light and *birefringence* which are key concepts in this high-resolution imaging technique.

3.1.1 Polarization of Light

Light exhibits the properties of an electromagnetic wave consisting of both electric and magnetic field components which oscillate perpendicularly to each other. As a transverse wave, it obeys the Maxwell's equations and can be described by the complex electric field vector:

$$\mathbf{E}(\mathbf{r}, t) = \mathbf{E}_0 \exp i(\mathbf{k} \cdot \mathbf{r} - \omega t + \phi) \quad (3.1)$$

where \mathbf{r} and t are respectively space and time parameters, \mathbf{k} wave vector denoting the direction of propagation, ω the angular frequency, ϕ the phase and \mathbf{E}_0 the direction and amplitude of the electric field vector.

The polarization state of light is determined by the direction of the electric field vector \mathbf{E} . Natural light wave vibrates in *all directions* perpendicular to its direction of propagation \mathbf{k} , this light is referred to as *unpolarized* light. When the vibrations occur in a *single*

plane perpendicular to \mathbf{k} , light is polarized. Different states of polarization of light are discriminated:

- linear polarization: \mathbf{E} always points in the same direction;
- circular polarization: \mathbf{E} describes a circle;
- elliptical polarization: \mathbf{E} describes an ellipse.

Fig. 3.1 illustrates the process of polarization using a polaroid filter¹ which filters out one-half of the vibrations upon transmission of the light.

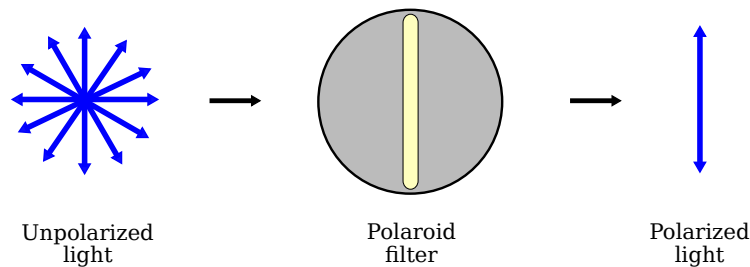


Figure 3.1: Unpolarized light is transmitted through a polaroid filter to emerge as polarized light with vibrations in a single plane.

3.1.2 Birefringence

Birefringence results from *optical anisotropy* created by the ordered arrangement of the molecules in a material, for instance calcite crystal. It is also called *double refraction*. In such a material or medium, the refractive index relies on both the state of polarization of the incident light and on the direction of propagation \mathbf{k} . This dependency can be described by the so-called *refractive index ellipsoid* or *indicatrix* (Born and Wolf, 2013).

In *uniaxial*² birefringent materials (such as brain WM), the indicatrix is an ellipsoid of revolution, as illustrated in Fig. 3.2, with a single *optical axis* i.e. the axis of rotation, and two principal refractive indices: the *ordinary* refractive index n_o and the *extraordinary* refractive index $n_e(\theta)$. The (mathematical) difference between the two refractive indices defines the birefringence Δn of a material:

$$\Delta n = n_e(\theta) - n_o \quad (3.2)$$

The ordinary refractive index is independent of the direction of propagation while the extraordinary index depends on the angle θ between the direction \mathbf{k} and the optic axis.

Light traveling through a birefringent medium experiences a phase difference called *retardance* δ between two orthogonal polarization components (ordinary and extraordinary

¹There exist different methods of polarization of light: by reflection, by refraction, by scattering etc (Born and Wolf, 2013; Göthlin, 1913; Collett, 2005)

²When the three principal axes are different, the material is *biaxially* birefringent.

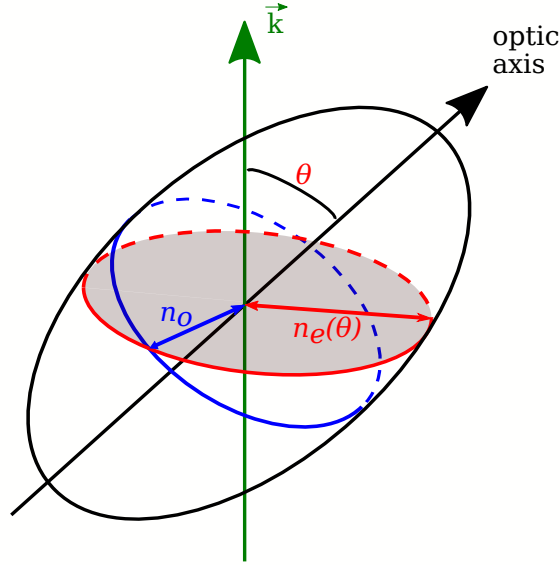


Figure 3.2: Rotational index ellipsoid of a positive uniaxial birefringent material. Depending on the orientation of the optic axis relative to the direction of propagation \mathbf{k} , the refractive index $n_e(\theta)$ of the extraordinary ray varies.

waves with refractive indices n_o and $n_e(\theta)$), see Fig. 3.3. This retardance alters the polarization state of the light, and for small values of Δn , it can be approximated as (Axer et al., 2011a; Larsen et al., 2007):

$$\delta \approx \frac{2\pi d}{\lambda} \Delta n \cos^2 \alpha \quad (3.3)$$

where d is the thickness of the birefringent medium, λ the wavelength of the incident light and $\alpha = 90^\circ - \theta$ is the out-of-plane angle of the optic axis i.e. the inclination angle of the fibers.

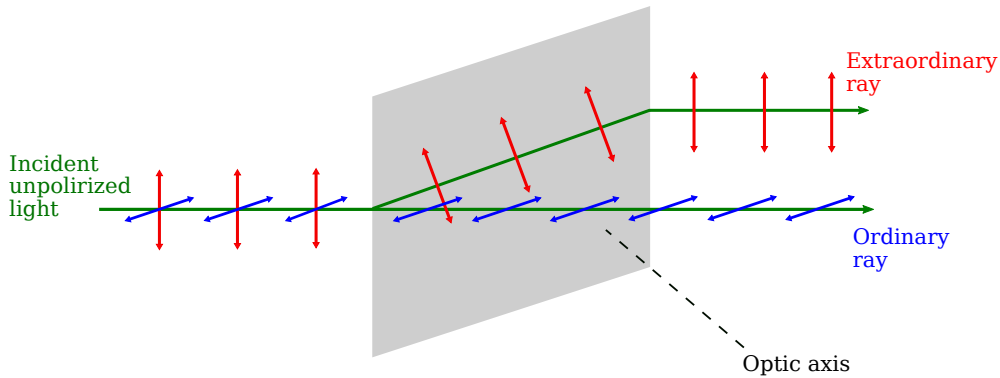


Figure 3.3: Unpolarized light beam traversing a birefringent medium is split into an ordinary ray in blue and an extraordinary ray in red with orthogonal linear polarization states. Adapted from (Hecht, 1998).

Birefringence in Human Body In the brain white matter, the *high* birefringence of the nerve fiber is predominantly *negative* uniaxial and the optic axis is oriented in the longitudinal fiber direction (Bear and Schmitt, 1936; Menzel et al., 2015; de Campos Vidal et al., 1980). This is due to the arrangement and packing of lipid molecules in the myelin sheath which surrounds most of the axons and was experimentally observed in diverse studies (Bear and Schmitt, 1936; de Campos Vidal et al., 1980). Note that, with respect to the radial optic axes, the myelin sheath displays positive uniaxial birefringence (Göthlin, 1913).

In the heart muscle, the cardiac fiber consists of myosin and collagen, exhibiting positive uniaxial and negative biaxial refringence, respectively. However, the PLI system is good at detecting uniaxial birefringence (Wang, 2013), therefore, the participation of the collagen is eliminated by embedding the heart tissue in methyl methacrylate (MMA) (Jouk et al., 1995) and the orientation of the cardiac fiber is measured from the myosin. More details in the next chapter, Sect. 4.1.1.

3.2 Polarimetric Measurements

3.2.1 (Brain) Tissue Preparation

3D-PLI transmits polarized light through unstained histological tissue sections in order to measure their birefringence. Here, we focus on the preparation of the brain tissue and later, in Chap. 4, on the human heart and its preparation. In any case, 3D-PLI is *invasive* and, therefore, restricted to postmortem tissues. The brain sections used in this work come from a human brain and its preparation is as follows:

- **Fixation:** The brain tissue is removed from the skull and dipped in buffered formalin (4% solution of formaldehyde) preferably within 24 hours after death, in order to conserve birefringence and prevent decay. Fixation should last at least 3 months.
- **Cryoprotection and freezing:** To avoid ice crystals formation, the brain is immersed in a 20% glycerin with Dimethyl sulfoxide (DMSO) for more than 3 weeks. It is then sealed in a air-tight plastic bag and frozen down to -80° Celsius for several months.
- **Sectioning:** A cryotome is used to section the frozen brain into slices of approximately $60\ \mu\text{m}$ thickness at -30° Celsius. Sectioning is done along one of the three anatomical plane: coronal, horizontal or sagittal (see Fig. 3.4), and as it causes tissue deformation, a block surface or *blockface image* is captured before cutting every slice. The blockface images are used later as reference for volumetric reconstruction.
- **Mounting:** Then every slice is mounted on a cooled glass slide and immersed in a solution of 20% glycerin to prevent dehydration. A coverslip is applied to avoid trapped air bubbles. Note that no histological staining is applied.

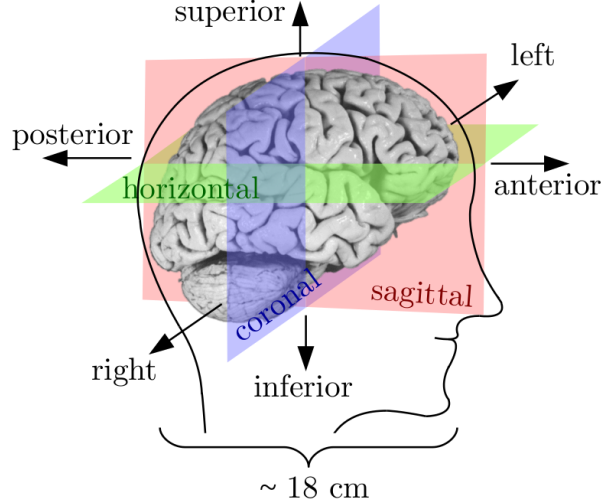


Figure 3.4: The human brain sectioning. Anatomical planes and directions along which the brain is sliced. Taken from (Menzel, 2018).

3.2.2 Measurement Setup

The experimental measurement setup is optimized for high-resolution imaging of unstained histological tissue sections. As illustrated in Fig. 3.5a, it generally consists of a (customized) **light source** with green³ wavelength spectrum to illuminate the sample, a pair of *linear* polarizers with orthogonal transmission axes i.e. the **polarizer** and the **analyzer**, a tiltable **specimen stage** between the polarizers and a **quarter-wave retarder**. A high-resolution charged-coupled device (CCD) **camera** records the transmitted light intensity. The polarizing filters i.e. the polarizer, the analyzer, and the quarter-wave retarder are simultaneously rotated by an angle $\rho \in \{0^\circ, 10^\circ, \dots, 170^\circ\}$ around the stationary sample. For each rotation angle ρ , the camera records the outgoing light intensity $I(\rho)$, yielding a series of gray scale images.

At each image pixel, the light intensity profile resulting from the N measurements acquired at equally distant rotation angles ρ_i describes a *sinusoidal signal* as illustrated in Fig. 3.5b. It can be analyzed using *discrete harmonic Fourier analysis*:

$$I(\rho) = a_0 + \sum_{n=1}^{N/2} \left(a_n \cos(n\rho) + b_n \sin(n\rho) \right), \quad (3.4)$$

$$a_0 = \frac{1}{N} \sum_{i=1}^N I(\rho_i), \quad a_n = \frac{2}{N} \sum_{i=1}^N I(\rho_i) \cos n\rho_i, \quad b_n = \frac{2}{N} \sum_{i=1}^N I(\rho_i) \sin n\rho_i, \quad (3.5)$$

where $N = 18$ in our case. Different parameter maps and the spatial fiber orientation can be computed from these Fourier coefficients. This analysis is presented in the next section.

Retardance and diattenuation The birefringent material can be considered a *wave retarder* since it causes a retardance δ which alters the polarization state of light. The phase

³A white source is used by Jouk et al, (Wang, 2013)

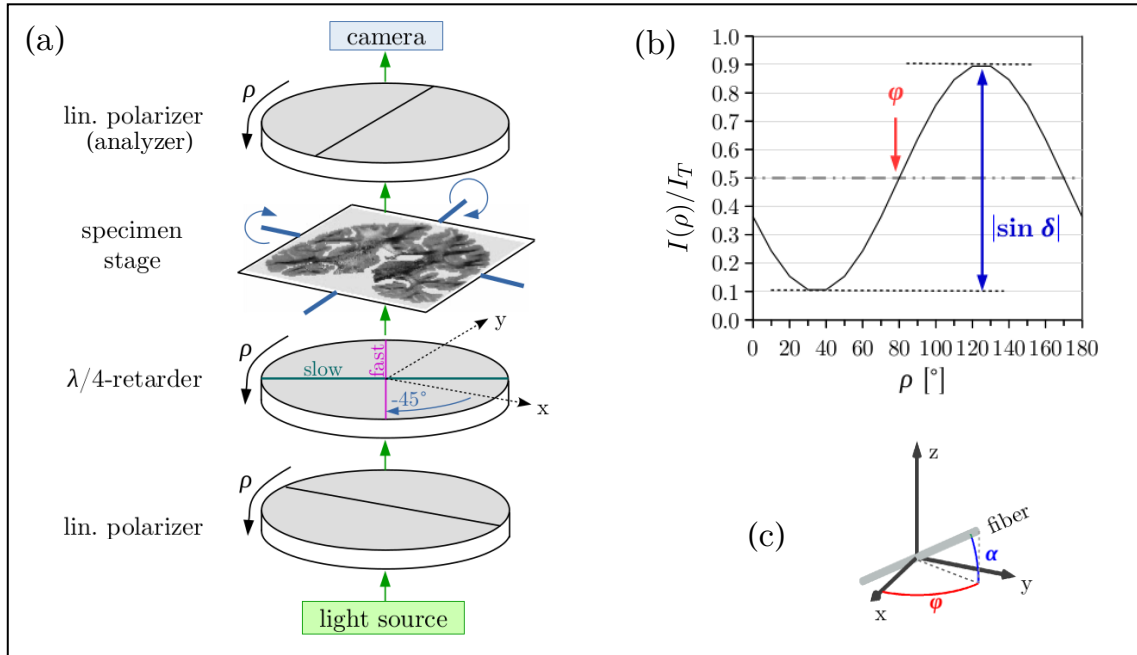


Figure 3.5: (a) Schematic of the Large-Area Polarimeter used in the INM-1 laboratory, Jülich, Germany: the specimen stage containing a brain tissue slice can be tilted around two axes and is placed between the pair of crossed linear polarizers and a quarter-wave retarder ($\lambda/4$ -retarder). During a measurement, the filters are rotated by discrete rotation angles ρ . (b, c) Measured sinusoidal signal whose phase φ (in red) correlates with the in-plane direction and amplitude with the out-of-plane inclination α (in blue) of the prevailing fiber orientation. Image adapted from (Menzel, 2018).

shift or retardance caused by the biological tissue will be discussed later in this chapter.

The polarizer and the analyser are optical elements with high diattenuation (close to one) used to create linearly polarized light, they are called *diattenuators*. Diattenuation refers to the anisotropic attenuation of light caused by absorption (dichroism) as well as scattering, further details can be found in (Chenault and Chipman, 1993; Chipman, 1995; Menzel et al., 2017) and references therein.

The quarter-wave retarder induces a retardance $\delta = \pi/2$ and is used to generate circularly polarized light from linearly polarized light. The fast axis of the retarder, see Fig. 3.5, is oriented at -45° with respect to the transmission axis of the first polarizer.

3.3 3D-PLI Signal Analysis

The experimental setup in Sect. 3.2.2 allows for the measurement of the birefringence of the studied specimen (brain tissue, myocardium, etc) and the derivation of the 3D nerve fiber orientation. To this end, the Jones (Jones, 1941) or Müller-Stokes (Mueller, 1943) formalisms can be used to describe the polarized light and to analyse the 3D-PLI signal.

3.3.1 Matrix Calculus

To mathematically describe the interaction between the polarized light and the elements of the polarimetric setup, the Jones calculus (Jones, 1941) can be used. In this formalism, the polarization state of light is represented by a 2×1 vector and each optical element by a complex 2×2 matrix. It has been used in previous 3D-PLI studies to describe the setup (Larsen et al., 2007; Axer et al., 2011a,b) and in simulations (Dohmen et al., 2015; Menzel et al., 2015). However, Jones calculus is only applicable assuming that the traversing light is *coherent* and *completely* polarized.

This assumption, though, limits its application. Therefore, the Müller-Stokes formalism is preferred (Chenault and Chipman, 1993; Desrosiers, 2014; Wiese, 2016; Menzel et al., 2017; Menzel, 2018) since it is applicable to partially polarized as well as incoherent light (as used to image the different datasets in this thesis). Moreover, whereas in the Jones formalism, the focus is on the description of the electrical field, in Müller-Stokes formalism the light intensity values recorded by the camera is directly calculated. Here, the polarization state of light is represented by a 4×1 vector or *Stokes vector* and the optical elements are described by 4×4 matrices or *Müller matrices*.

Stokes vectors: The Stokes vector is related to the electric field vector as follows (Chipman, 1995; Collett, 2005):

$$\mathbf{S} = \begin{pmatrix} S_0 \\ S_1 \\ S_2 \\ S_3 \end{pmatrix} = \begin{pmatrix} |E_x|^2 + |E_y|^2 \\ |E_x|^2 - |E_y|^2 \\ 2 \cdot \text{Re}(E_x \overline{E_y}) \\ -2 \cdot \text{Im}(E_x \overline{E_y}) \end{pmatrix}, \quad S_0^2 \geq S_1^2 + S_2^2 + S_3^2 \quad (3.6)$$

where the over-line denotes the complex conjugate and the S_i are called the Stokes polarization parameters, the first S_0 gives the total outgoing light intensity I which is used to determine the spatial orientation of the fiber, and S_1 , S_2 and S_3 describe the predominance of two orthogonal polarization states (Collett, 2005) i.e. linearly horizontal over vertical, linearly $+45^\circ$ over -45° and circularly right- over left-handed polarized light, respectively. Note that, the \geq turns into $=$ when light is completely polarized, and for partially polarized light, it is defined a *degree of polarization*

$$p = \frac{\sqrt{S_1^2 + S_2^2 + S_3^2}}{S_0}, \quad 0 \leq p \leq 1$$

Completely *unpolarized* light is described by $\mathbf{S}_{unpol} = (I, 0, 0, 0)^T$ with the degree of polarization $p = 0$. A change in the polarization state of a light beam is described by multiplying the Stokes vector with a real valued 4×4 -Müller matrix.

Müller matrices: The Müller matrix for a general wave retarder and diattenuator is given by (Chenault and Chipman, 1993; Collett, 2005):

$$\mathcal{M}(\delta, D, \tau) = \tau \begin{pmatrix} 1 & D & 0 & 0 \\ D & 1 & 0 & 0 \\ 0 & 0 & \sqrt{1-D^2} \cos \delta & \sqrt{1-D^2} \sin \delta \\ 0 & 0 & -\sqrt{1-D^2} \sin \delta & \sqrt{1-D^2} \cos \delta \end{pmatrix} \quad (3.7)$$

where δ is the retardance, D the diattenuation of the linear polarizers, and τ the *average transmittance* referring to the fraction of unpolarized light transmitted through the sample. Here, the principal axes of birefringence and diattenuation are assumed to be coincident and aligned with the x- and y-axes of the reference frame.

When the Müller matrix $\mathcal{M}(\delta, D, \tau)$ is rotated in counter-clockwise direction by an angle ξ , it yields:

$$\mathcal{M}(\xi, \delta, D, \tau) = \mathcal{R}(\xi) \cdot \mathcal{M}(\delta, D, \tau) \cdot \mathcal{R}(-\xi) \quad (3.8)$$

where $\mathcal{R}(\xi)$ is the Müller matrix of the rotator (Chipman, 1995):

$$\mathcal{R}(\xi) = \begin{pmatrix} 1 & 0 & 0 & 0 \\ 0 & \cos 2\xi & -\sin 2\xi & 0 \\ 0 & \sin 2\xi & \cos 2\xi & 0 \\ 0 & 0 & 0 & 1 \end{pmatrix}. \quad (3.9)$$

When an incident light beam represented by the Stokes vector \mathbf{S} traverses an assembly of optical elements described by \mathcal{M} , the resulting outgoing beam is given by:

$$\mathbf{S}' = \mathcal{M} \cdot \mathbf{S}, \quad (3.10)$$

where (S'_0) , the first entry of the Stokes vector \mathbf{S}' , gives the intensity of the outgoing light.

3.3.2 Application of Müller-Stoke Calculus

The Müller matrices $\mathcal{M}(\xi, \delta, D, \tau)$ for the different components of the optical setup are as follows (Menzel et al., 2017):

$$\text{Polarizer:} \quad P(\rho, D_P, \tau_P) \quad \equiv \quad \mathcal{M}(\rho, 0, D_P, \tau_P), \quad (3.11)$$

$$\text{Retarder:} \quad R(\rho, \gamma, \tau_R) \quad \equiv \quad \mathcal{M}(\rho - 45^\circ, \gamma, 0, \tau_R), \quad (3.12)$$

$$\text{Brain tissue:} \quad M(\varphi, \delta, \tau) \quad \equiv \quad \mathcal{M}(\varphi, \delta, 0, \tau), \quad (3.13)$$

$$\text{Analyzer:} \quad \Lambda(\rho, D_\Lambda, \tau_\Lambda) \quad \equiv \quad \mathcal{M}(\rho + 90^\circ, 0, D_\Lambda, \tau_\Lambda). \quad (3.14)$$

In 3D-PLI measurements, the retardance of the polarizers and the diattenuation of the retarders have been shown by (Menzel et al., 2017) to be negligible: $\delta = 0$ for the polarizers P and Λ , and $D = 0$ and $\tau = 1$ for the quarter-wave retarder R and the sample M . Moreover, ideal filter properties are assumed:

$$D_P = D_\Lambda = 1, \tau_P = \tau_\Lambda = 1/2; \gamma = \pi/2, \tau_R = 1. \quad (3.15)$$

The incident light source is assumed to be completely unpolarized and the camera to be insensitive to polarization i.e. both are represented by the Stokes vector of unpolarized light \mathbf{S}_{unpol} . Thus, one can compute the analytical expression of the transmitted light intensity by multiplying the above Müller matrices and evaluating the first entry of the Stokes vector (S'_0):

$$\mathbf{S}'(\rho) = \Lambda(\rho, D_\Lambda, \tau_\Lambda) \cdot M(\varphi, \delta, \tau) \cdot R(\rho, \gamma, \tau_R) \cdot P(\rho, D_P, \tau_P) \cdot \mathbf{S}_{unpol} \quad (3.16)$$

$$\begin{aligned} \Rightarrow I(\rho) = \tau \tau_\Lambda \tau_R \tau_P I_0 & \left[1 + D_\Lambda D_P \sin \gamma \sin \delta \sin (2(\rho - \varphi)) \right. \\ & \left. - D_\Lambda D_P \cos \gamma \left(\cos^2 (2(\rho - \varphi)) + \cos \delta \sin^2 (2(\rho - \varphi)) \right) \right] \end{aligned} \quad (3.17)$$

where I_0 is the intensity of the light source. Taking into account ideal filter assumptions (see Eq. (3.15)), the expression of the light intensity simplifies to:

$$I(\rho) = \frac{I_0}{4} \left(1 + \sin \delta \sin (2\rho - 2\varphi) \right) \quad (3.18)$$

with

$$\delta = \frac{2\pi d}{\lambda} \Delta n \cos^2 \alpha. \quad (3.19)$$

This transmitted light intensity, which is a measure of the predominant fiber orientation (φ, α), is then analyzed via a discrete harmonic Fourier analysis for each pixel.

3.3.3 Fourier Analysis of the Signal

The reconstruction of the fiber orientation which is defined in spherical coordinates by the in-plane direction angle φ and the out-of-plane inclination angle α , requests the analysis of the acquired signal using discrete harmonic Fourier analysis. At each image pixel the transmitted light intensity $I(\rho)$ in Eq. (3.18) can be expressed using the Fourier coefficients of order zero and two (Axer et al., 2011a):

$$I(\rho) = a_0 + a_2 \cos 2\rho + b_2 \sin 2\rho \quad (3.20)$$

with

$$a_0 = \frac{I_0}{4}, \quad a_2 = -\frac{I_0}{4} \sin \delta \sin 2\varphi, \quad b_2 = \frac{I_0}{4} \sin \delta \cos 2\varphi. \quad (3.21)$$

From these coefficients, different parameter maps (illustrated in Fig. 3.6) are computed:

- **Transmittance (I_T):** is the averaged transmitted light intensity over all rotations ρ :

$$I_T = 2a_0. \quad (3.22)$$

- **Direction (φ):** is the in-plane fiber orientation angle which is obtained from the phase of the intensity profile (see Fig. 3.5, in red):

$$\varphi = \frac{1}{2} \text{atan2}(-a_2, b_2) \in [0, \pi), \quad (3.23)$$

where atan2 is the two-argument variant of arctangent⁴.

- **Retardation (r):** is a measure of the birefringence of the tissue and is computed from the normalized amplitude ($I_N = I(\rho)/I_T$) of the intensity profile:

$$r \equiv |\sin \delta| = \frac{\sqrt{a_2^2 + b_2^2}}{a_0}. \quad (3.24)$$

Determination of the Fiber Inclination (α): the out-of-plane inclination angle can be calculated from the retardation according to Eq. (3.19) as $\delta \propto \cos^2 \alpha$, if wavelength λ , local birefringence Δn and section thickness d are precisely known. However in general, it is not an easy task to know these parameters. Therefore, Axer *et al.* (Axer *et al.*, 2011a) introduced the *relative thickness* d_{rel} to merge them in a single parameter. Thus, the inclination angle can be approximated as:

$$|\alpha| = \arccos \left(\sqrt{\frac{2 \cdot \arcsin(r)}{\pi \cdot d_{rel}}} \right) \quad (3.25)$$

where the relative thickness d_{rel} is defined as the ratio of the actual thickness d and the thickness at which a pure in-plane fiber with $\alpha \approx 0$ acts as an ideal quarter-wave retarder. As one can see, only the absolute value of $\alpha \in [0, \pi/2]$ can be determined from r , which leads to the *inclination sign ambiguity* in 3D-PLI. This ambiguity needs to be disentangled in order to have a correct spatial fiber orientation and this task has been the first contribution in our Ph.D work, see next chapter.

Reconstruction of the Fiber Orientation: Once the sign ambiguity of the inclination angle α is resolved (see Chap. 4), the spatial fiber orientation is defined as a vector \mathbf{v} confined on the unit sphere. This fiber orientation is parameterized in each voxel by the direction angle φ and inclination angle α :

$$\mathbf{v} = \begin{pmatrix} \cos \alpha \cdot \cos \varphi \\ \cos \alpha \cdot \sin \varphi \\ \sin \alpha \end{pmatrix}. \quad (3.26)$$

⁴The function $\text{atan2}(x, y)$ indicates the angle in radians between the positive x-axis and the point (x, y) . The angle is positive for $y > 0$ and negative for $y < 0$.

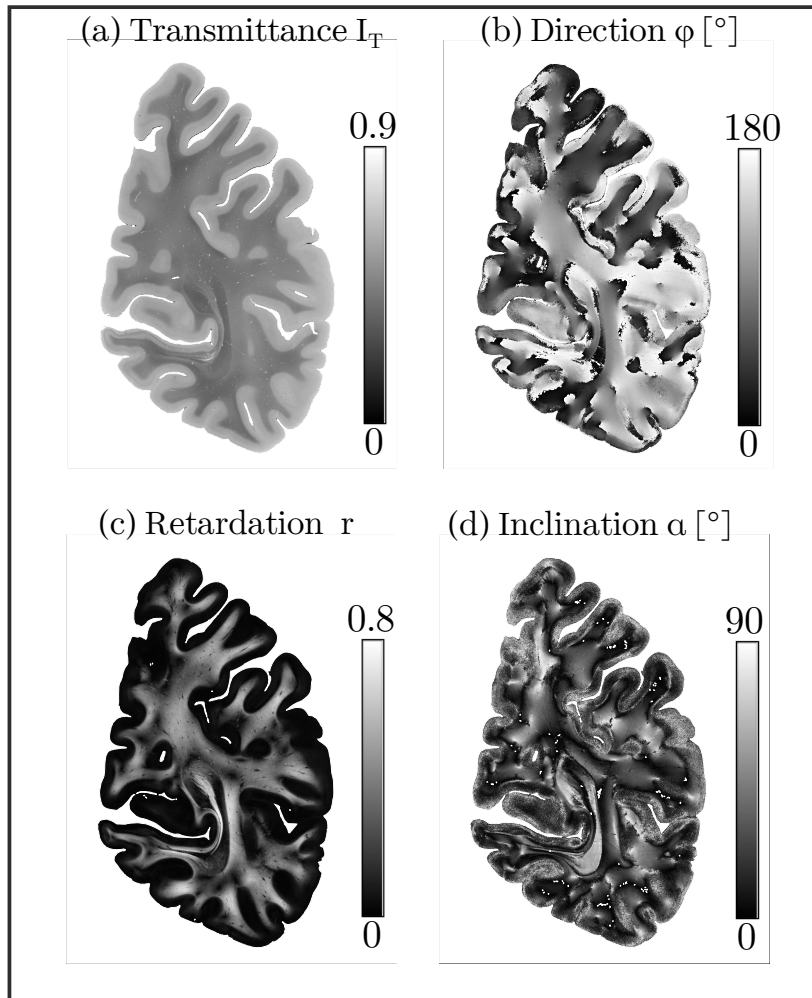


Figure 3.6: Parameter maps of a coronal section from the right hemisphere of the human brain imaged at $64 \times 64 \times 70 \mu m^3$ resolution: (a) normalized transmittance $I_N = I(\rho)/I_T$, (b) in-plane direction angle φ , (c) retardation r , and (d) out-of-plane inclination angle α .

Part III

Contributions

Chapter 4

On 3D-PLI Inclination Sign Ambiguity

In 3D-PLI, the 3D fiber orientation in each voxel is defined by the direction angle and the inclination angle whose sign is unknown. To have an accurate explanation of the fiber orientation, it is compulsory to clear up this sign ambiguity. A tilting process provides information about the true inclination sign, however, the technique is highly sensitive to noise. Here, a method based on partial differential equations is proposed: the total variation model of Rudin-Osher-Fatemi is extended to 3D orientation vector images to reduce the noise and restore the inclination sign. The proposed algorithm is evaluated on synthetic and human heart data and results show that the true sign of the inclination angle can be successfully extracted. Parts of this chapter are based on the publication ([Alimi et al., 2017b](#)).

4.1 Introduction

In this chapter, the cardiac tissue is studied instead of the brain which is investigated in the rest of this thesis. Indeed, the use of 3D-PLI is not restricted to the brain and this chapter enables to see its performance on the myocardium to extend its application to another very important human organ, the heart. Let us recall that 3D-PLI is an optical approach that utilizes the birefringence in postmortem organs to map their spatial fibers structure at sub-millimeter resolutions.

4.1.1 3D-PLI on Human Heart

Cardiac tissue birefringence In the heart muscle, the cardiac fiber consists of myosin and collagen, exhibiting positive uniaxial and negative biaxial refringence, respectively. However, the PLI system is good at detecting uniaxial birefringence ([Wang, 2013](#)). Therefore, the participation of the collagen is eliminated by embedding the heart tissue in methyl methacrylate (MMA) ([Jouk et al., 1995](#)) and the orientation of the cardiac fiber is measured

from the birefringence of the myosin.

4.1.2 Inclination Sign Estimation

To estimate the inclination angle in each voxel, the tissue sample is scanned thanks to a measurement setup as presented in the previous chapter. Linearly polarized light passes through the sample and permits to detect its birefringent structure. The outgoing light is analyzed to get the spatial fiber orientation described by a pair of angles:

- the *in-plane* or direction angle φ determining the x-y orientation of the fiber;
- the *out-of-plane* or inclination angle α , the vertical component of the fiber.

Therefore, as [Axer et al. \(2011a\)](#) mentioned, each histological section is characterized by a 3D vector field visualized as a fiber orientation map (FOM), see Fig. 4.1. The FOM shows the dominant fiber orientation in each voxel.

We recall that, the fiber orientation vector \mathbf{v} at voxel location is parameterized by the two angles φ and α as follows:

$$\mathbf{v} = \begin{pmatrix} \cos \alpha \cdot \cos \varphi \\ \cos \alpha \cdot \sin \varphi \\ \sin \alpha \end{pmatrix}. \quad (4.1)$$

The voxel dimensions are defined by the image pixel size and the section thickness.

The angles φ and α are restricted to $[0^\circ, 180^\circ]$ and $[-90^\circ, 90^\circ]$, respectively. The inclination angle α can be derived from Eq. (3.19), however, it has a nonlinear relation with the *retardation* r , and can be estimated as

$$|\alpha| = \arccos \left(\sqrt{\frac{2 \cdot \arcsin(r)}{\pi \cdot d_{rel}}} \right) \quad (4.2)$$

where d_{rel} is a reference value or relative thickness depending on the section thickness, the birefringence and the wavelength. Eq. (4.2) gives only the absolute value of α , which introduces the inclination sign ambiguity in 3D-PLI. It is compulsory to clear up this ambiguity in order to have an correct spatial fiber orientation in each voxel. Indeed, 3D-PLI based tractography can then be performed and utilized in multimodal analysis with diffusion MRI.

To address this sign ambiguity in microscope imaging, [Pajdzik and Glazer \(2006\)](#) developed a *tilting stage* to discriminate positive and negative inclination signs of crystal orientations. A similar tilting setup is built for 3D-PLI by [Axer et al. \(2011b\)](#); [Jouk et al. \(1995, 2000\)](#).

4.1.3 Tilting Process

Measurements from the tiltable specimen stage give additional information about the inclination sign at each individual pixel. The stage can be tilted in two axes, i.e. four

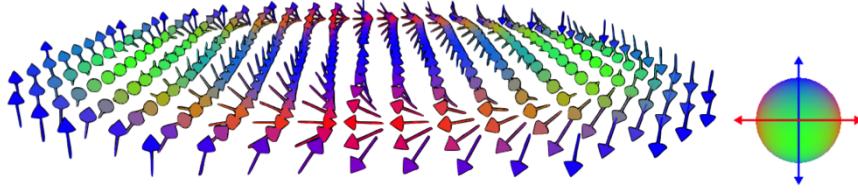


Figure 4.1: An example of simulated FOM enabling a clear vector visualization of the 3D fiber orientation vectors in a histological tissue slice. Adapted from (Dohmen, 2013)

geographical directions $\psi \in \{N = 90^\circ, W = 180^\circ, S = 270^\circ, E = 0^\circ\}$: the edge of the specimen in the specified direction ψ is tilted down towards the light source by an angle $\tau \approx 4^\circ$ to avoid strong distortions.

The sign of α can be determined most accurately when φ and ψ are similar: positively inclined fibers can be discriminated from negatively inclined ones by their decrease in absolute inclination after tilting. Otherwise, the change is less important or even inverted. Dohmen (2013) noticed that these changes are marginal and hence very sensitive to noise and proposed this signun function which describes this relationship as

$$\text{sgn}(\alpha) = \text{sgn}(|\alpha^{\psi \pm 180^\circ}| - |\alpha^\psi|) \cdot \text{sgn}(\cos(\varphi - \psi)) \quad (4.3)$$

where α^ψ denotes the tilted measurement for each tilting direction ψ and $\psi \pm 180^\circ$ which is the opposite direction.

Measurements from the tiltable specimen stage allow for the derivation of the sign of the inclination angle but the process is highly sensitive to noise. In this work, the total variation (TV) model of Rudin-Osher-Fatemi (ROF) (Rudin et al., 1992) is extended to 3D orientation vector images and proposed for noise removal and restoration of the proper sign of the out-of-plane angle.

4.2 Method: Inclination Sign Restoration

To correct the wrong inclination sign, a partial differential equations (PDEs) method, which has been widely used over the past decades with edge preservation, is considered. This is interesting because different fiber populations located within a region seem to be delimited by some edges at their intersections.

The restoration of the sign of α is performed via a PDE method which is based on a variational approach of energy functional minimization: the total variation (TV) model of Rudin-Osher-Fatemi (ROF) (Rudin et al., 1992). In this work, the ROF model is extended and applied to tackle our problem of restoring 3D orientation vectors images.

4.2.1 Rudin-Osher-Fatemi model

The total variation minimizing process of ROF is a classical variational denoising algorithm developed for scalar images. This algorithm looks for an equilibrium state of an energy functional which consists of the TV norm of the image to be recovered I and its fidelity to the noisy input image I_0 . The idea is to find the (unique) minimizer, I , of

$$\min_I E(I) = \frac{\lambda}{2} \int_{\Omega} |I_0 - I|^2 dx dy + \int_{\Omega} \Phi(|\nabla I|) dx dy, \quad x, y \in \Omega \quad (4.4)$$

with Ω the image domain and $\lambda > 0$ a scaling parameter controlling the fidelity of the solution to the input image. This is further generalized by the Φ -formulation (Deriche and Faugeras, 1995) of the functional whose associated Euler-Lagrange (EL) equation is given by

$$-F \equiv \lambda(I_0 - I) + \operatorname{div} \left(\Phi'(|\nabla I|) \frac{\nabla I}{|\nabla I|} \right) = 0 \quad (4.5)$$

where Neumann boundary conditions are assumed. The solution is usually found by

$$I_t = -F, \quad \text{and} \quad I|_{t=0} = I_0 \quad (4.6)$$

The actual Φ function used in this work is $\Phi(\bullet) = \sqrt{\epsilon^2 + \bullet^2}$ with $\epsilon > 0$ a small parameter. This removes the singularity when $|\nabla I| = 0$ by approximating $E(I)$ and allows an easy implementation by standard discretization of the Euler-Lagrange equations.

In the following section, the ROF model is adapted and applied to restore the inclination sign in pixels where the tilting process is not efficient enough. The aim is now to perform the TV minimizing process on 3D fiber orientation vector images for denoising and finding the sign of α for a given histological FOM.

Consequently, the finally *signed* inclination angle α is obtained by multiplication of the absolute angle with the sign of the restored angle α_{rof} , as follow:

$$\alpha = |\alpha| \cdot \operatorname{sgn}(\alpha_{\text{rof}}) \quad (4.7)$$

4.2.2 ROF on sectional fiber orientation map

Let us recall that in 3D-PLI each histological section is characterized by a 3D vector field visualized as a fiber orientation map (FOM) indicating the prevailing fiber orientation in each voxel (Axer et al., 2011a). Here, the TV process is extended to 3D and executed to denoise the FOM (built from the noisy tilting measurements) in order to derive the inclination angle sign. The functional to be minimized is

$$E(V) = \frac{\lambda}{2} \int_{\Omega} |V_0 - V|^2 dx dy dz + \int_{\Omega} \Phi(|\nabla V|) dx dy dz + \gamma(|V|^2 - 1), \quad x, y, z \in \Omega \quad (4.8)$$

where the third term, which is controlled by the parameter γ , constrains the recovered fiber orientation vector V in a unit sphere, i.e. $|V| = \sqrt{u^2 + v^2 + w^2} = 1$ is its unit norm, V_0 is the noisy fiber orientation vector computed from the tilting process using Eq. (4.1), V is the reconstructed orientation given by the ROF minimization of E and u , v and w are its components. The associated Euler-Lagrange equations are

$$-\lambda(V_0 - V) - \operatorname{div}\left(\Phi'(|\nabla V|)\frac{\nabla V}{|\nabla V|}\right) + 2\gamma V = 0 \text{ in } \Omega, \quad (4.9)$$

$$\text{with } \frac{\partial V}{\partial n} = 0 \text{ on the boundary of } \Omega = \partial\Omega. \quad (4.10)$$

Note that, to u , v and w are associated the respective Euler-Lagrange equations EL_u , EL_v and EL_w . The value of γ is thus determined by multiplying each component to its corresponding EL equation, to obtain uEL_u , vEL_v and wEL_w which are summed and simplified to give

$$\gamma = \frac{1}{2} \sum_{i=1}^3 \operatorname{div}\left(\Phi'(|\nabla v_i|)\frac{\nabla v_i}{|\nabla v_i|}\right) + \frac{\lambda}{2} \left(\sum_{i=1}^3 v_i v_{0i} - 1\right) \quad (4.11)$$

where v_i and v_{0i} are the components of the recovered and the noisy orientation vectors, respectively. The parameter γ is then injected in the Euler-Lagrange equations and the solution is found by simultaneously solving

$$\begin{aligned} u_t = & \lambda \left[v(vu_0 - uv_0) + w(wu_0 - uw_0) \right] \\ & - u \left[v \operatorname{div}\left(\Phi'(|\nabla v|)\frac{\nabla v}{|\nabla v|}\right) + w \operatorname{div}\left(\Phi'(|\nabla w|)\frac{\nabla w}{|\nabla w|}\right) \right] \\ & + (1 - u^2) \operatorname{div}\left(\Phi'(|\nabla u|)\frac{\nabla u}{|\nabla u|}\right) \end{aligned} \quad (4.12)$$

for component u , and similarly v_t for v and w_t for w . The sign of α is the same as the sign of the vertical component (w) of the restored 3D fiber orientation vector.

4.3 Results and discussion

4.3.1 On synthetic data

The extended ROF algorithm is evaluated on a synthetic histological FOM where orientation vectors are computed from synthetic φ and α maps chosen so as to have four fiber populations with different orientations. In the noiseless FOM, each fiber orientation unit vector \mathbf{v} is computed according to Eq. (4.1). Then noise is simulated following a zero-mean normal distribution $\mathcal{N}(0, \sigma^2)$ with variance σ^2 (Dohmen, 2013), sampled and added to the angles to get the noisy FOM ($nFOM$). The signal-to-noise ration (SNR) is such that $SNR = 1/\sigma^2$.

The algorithm is performed on ($nFOM$) to produce new orientation vectors, $tvFOM$. The idea is then to compare the amount of wrong inclination signs from $nFOM$ to those

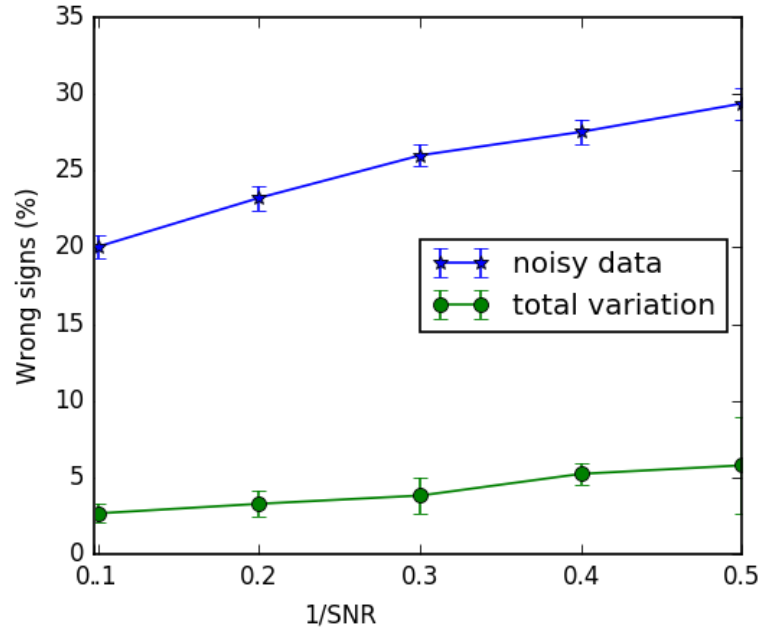


Figure 4.2: Percentage of wrongly estimated inclination signs as noise increases. Each data point corresponds to the mean and standard deviation over 100 noisy realizations.

obtained after restoration. In Fig. 4.2, results show that with different SNR, the percentage of wrong signs in $nFOM$ is highly reduced after restoration. This indicates the algorithm significantly reduces the wrong signs and therefore clears up the ambiguity.

4.3.2 On human heart data

The human data consist of PLI measurements of histological sections of a whole cardiac myocardium. The absolute inclination angle map of a ventricular slice is chosen as shown in Fig. 4.3A. The tilting process is performed and the corresponding α map is displayed in Fig. 4.3B where the wrongly estimated signs are easily visible almost everywhere on the tissue when referring to the color map.

The extended TV minimization is then applied to the noisy $nFOM$ built from the tilting measurements and the result is shown in Fig. 4.3C. Here, one can see some wrong signs but the ROF process has crucially restored them. This improvement is more observable on the zoomed region of interest in Fig. 4.3D and Fig. 4.3E where the fibers of the left and right ventricles meet the fibers of the septum.

To quantify the effect of our TV algorithm on the real data, the randomness of signs of α from the tilting measurements and the TV process has been investigated. A local entropy filter with a radius of 5 is therefore applied to both inclination maps, then the mean entropy is computed and a reduction of 46% of the randomness of signs is achieved by the extended TV process as illustrated in Fig. 4.3B and Fig. 4.3C. It is important to note that, in the absence of real heart ground truth data, the entropy filter is an appropriate quantitative measure.

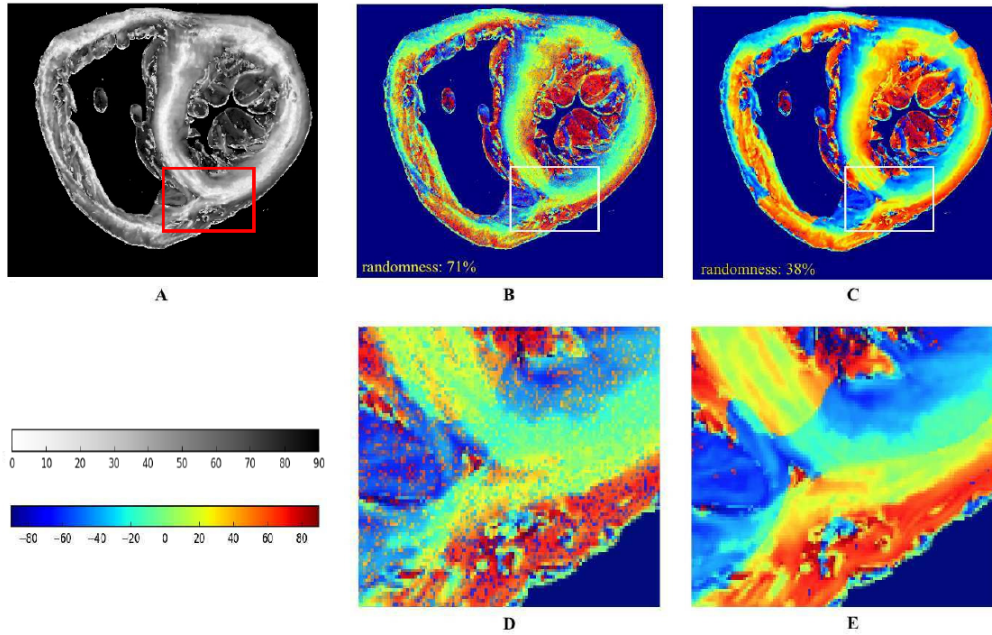


Figure 4.3: Inclination angle maps of a coronal ventricular slice: (A) Absolute inclination. (B) and (D) Signed α from tilting measurements. (C) and (E) Signed α after TV restoration. The white rectangle represents the region of interest displayed in (D) and (E). The angle is coded in gray scale (0° to 90°) in (A) and in false color (-90° to 90°) otherwise. The best results are achieved by the extended TV algorithm on these real data.

Our analysis, however, could be extended to investigate the impact of regularization in the proposed approach. In actuality, different scaling or smoothing parameters were manually tested in the synthetic experiment and finally one was chosen and re-used in the real data experiment. Indeed, an optimal smoothing parameter could be obtained using the L-curve method (Hansen, 1999) or the Generalized Cross-Validation approach (Craven and Wahba, 1978). This would highlight the effects of regularization and constitute a significant input to our work.

4.4 Conclusion

In this chapter, the proposed Total Variation model is evaluated on both synthetic and human cardiac data and results reveal that the estimation of the signs with the tiltable stage is significantly improved. Indeed, the image restoration process substantially reduces the noise and provides a better determination of the sign of the inclination angle α , and consequently resolves the sign ambiguity.

Thanks to this contribution to the inclination sign recovery and the high resolution of 3D-PLI, local fiber information from individual voxels can be properly integrated to produce a more global insight into the whole fiber architecture of the heart and, by extension, of the brain white matter.

Chapter 5

Analytical Fiber Orientation Distribution in 3D-PLI

This chapter proposes an analytical approach to compute the fiber orientation distribution (FOD) from high-resolution vector data provided by 3D-PLI. The analytical FOD –or aFOD– is modeled as a sum of K orientations/Diracs on the unit sphere, described on a spherical harmonics basis and analytically computed using the spherical Fourier transform. We evaluate and validate the aFOD on rich synthetic data and on human brain data. In particular, investigations on the right occipital lobe illustrate the ability of the aFOD to accurately reconstruct its white matter (WM) fascicles and to bridge the spatial resolution gap from microscopic 3D-PLI information to macro- or mesoscopic scales of diffusion MRI, while being a means to evaluate prospective spatial resolution limits for diffusion MRI to reconstruct region-specific WM tracts. These results demonstrate the interest and great potential of our analytical approach. Parts of this chapter are based on the publications (Alimi et al., 2018b, 2019a) –or submitted to Medical Image Analysis–.

5.1 Introduction

Diffusion MRI is the only imaging technique able to assess the structural architecture of human fibrous organs, *in vivo* and *non invasively* (Le Bihan et al., 1986; Basser et al., 1994; Tuch, 2004; Jones, 2010; Johansen-Berg and Behrens, 2013; Tournier, 2019; Leemans, 2019). However, different imaging methods at multiple scales are necessary to improve our understanding of brain and heart disorders. By providing microscopic fiber orientation measurements, 3D-PLI is not only a potential technique to validate diffusion MRI results but also a complementary imaging approach (Axer et al., 2011a; Alimi et al., 2017b). Complementing diffusion MRI with 3D-PLI measurements, therefore, requires to bridge the spatial scale information from micro to millimeter scales. Thus, the fiber orientation distribution function (fODF) –or fiber ODF–, which is widely used in the diffusion community (Tuch, 2004; Alexander, 2005; Descoteaux et al., 2007; Tournier et al., 2004; Dell’Acqua

and Tournier, 2019), is a suitable tool to compare diffusion MRI and 3D-PLI fiber orientation estimates in 3D.

On this account, Axer et al. (2016) proposed an estimate of the fiber ODF derived from high-resolution 3D-PLI, called *pliODF*. This technique enables the bridging of spatial scales from micro to macroscopic dimensions, for instance, to the millimeter resolution of diffusion MRI. pliODF benefits from the important concept of *super-voxel* (SV) which allows for the downsampling of the high-resolution orientation vectors from the fiber orientation map (FOM) (Axer et al., 2011a), and then estimating the fODF on the unit sphere by expanding a normalized directional histogram with a series of SH functions. By changing the SV size, the fODF can be computed at different spatial scales (Axer et al., 2016; Alimi et al., 2018b, 2019a). Axer et al. (2016) refer to a tissue voxel containing a single high-resolution fiber orientation as “*native voxel*” and the super-voxel regroups $K = n_x \times n_y \times n_z$ native voxels. pliODF, though, is derived from an empirically parameterized radial histogram, which makes it a discrete method. It relies on a histogram binning procedure which can introduce angular errors in the recovered fODFs (Alimi et al., 2018b), and since it is represented on a SH basis, it can also limit the order of its SH expansion (Alimi et al., 2017c). In order to overcome these issues, Alimi et al. (2017c) proposed to regularize the pliODF using the Laplace-Beltrami operator and therefore improved its results, see Appendix A.

In this chapter, we present an analytical approach to determine the FOD from 3D-PLI data in order to assess the spatial distribution of fiber orientations in each super-voxel. Our method is based on defining each fiber orientation in a native voxel as a 2D Dirac delta function on the unit sphere and the FOD as a sum of these Diracs in each SV. The aFOD is continuously described on a spherical harmonics basis and analytically computed via the spherical Fourier transform and by means of the Diracs. In the following, (1) we give a full description of our method to analytically compute the FOD, (2) and present the highly rich synthetic dataset which simulates the brain white matter fibers using a geometric model and the different performed tests to demonstrate its high angular resolution and precision and robustness to noise. (3) We then perform our technique on human brain data at different spatial scales while preserving the original high-resolution organization of WM fiber bundles and (4) finally present it as a means for diffusion MRI to assess potential spatial resolution limits to track specific fascicles in the human brain.

5.2 Analytical FOD in 3D-PLI

The fiber orientation distribution provides a comprehensive statistical description of integrated 3D-PLI vector data (Axer et al., 2016; Alimi et al., 2018b, 2019a) and positions itself as a suitable tool for multimodal analysis and comparisons (Schilling et al., 2016). As a function defined on the unit sphere \mathbb{S}^2 , the FOD can be expanded as a linear combination of spherical harmonics. In this section, we give a brief background information on spherical

harmonics before presenting the analytical approach to compute the FOD.

5.2.1 Spherical Harmonics

The spherical harmonics of order l and phase factor m are defined as

$$Y_l^m(\theta, \phi) = \sqrt{\frac{2l+1}{4\pi} \frac{(l-m)!}{(l+m)!}} P_l^m(\cos \theta) e^{jm\phi} \quad (5.1)$$

where P_l^m are the associated Legendre polynomials, the angles $\theta \in [0, \pi]$ and $\phi \in [0, 2\pi]$ are the colatitude and azimuth, respectively.

The spherical harmonics $\{Y_l^m : -l \leq m \leq l, l = 0, 1, \dots\}$ form an orthonormal basis over $L^2(\mathbb{S}^2)$ and any square integrable function $f(\theta, \phi) \in L^2(\mathbb{S}^2)$ can be expressed as

$$f(\theta, \phi) = \sum_{l=0}^{\infty} \sum_{m=-l}^l c_{lm} Y_l^m(\theta, \phi) \quad (5.2)$$

where c_{lm} are the SH coefficients of f . These coefficients are obtained by computing the spherical Fourier transform (Healy Jr et al., 1998) of f defined as

$$c_{lm} = \int_{\mathbb{S}^2} f(\mathbf{w}) \overline{Y_l^m(\mathbf{w})} d\mathbf{w} \quad (5.3)$$

for $\mathbf{w} \in \mathbb{S}^2$ and the over-bar denotes the complex conjugation. The unit vector \mathbf{w} is related to (θ, ϕ) by

$$\mathbf{w}(\theta, \phi) = [\sin \theta \cos \phi \quad \sin \theta \sin \phi \quad \cos \theta]^T \quad (5.4)$$

where \cdot^T indicates transposition. In this chapter, both functions $f(\theta, \phi)$ and $f(\mathbf{w})$ are assumed to be equal and written interchangeably to simplify notations.

5.2.2 Analytical Fiber Orientation Distribution

We demonstrate, in this section, that without any discretization which leads to loss of orientation information, the aFOD can be analytically reconstructed from high-resolution 3D-PLI orientation measurements, –as illustrated in Fig. 5.1–. We show how we model our aFOD before we obtain the exact SH coefficients which uniquely characterize it.

aFOD as sum of K Diracs In each native voxel of the fiber orientation map (visualizing the dominant fiber orientation), we propose to describe the unit fiber orientation vector as a two dimensional Dirac delta function δ on the sphere. Therefore, in a SV containing K orientations (θ_k, ϕ_k) , the fiber orientation distribution function f can be modeled as the sum of K Diracs (Deslauriers-Gauthier et al., 2016; Deslauriers-Gauthier and Marziliano, 2013), that is

$$f(\theta, \phi) = \frac{1}{K} \sum_{k=1}^K \delta(\cos \theta - \cos \theta_k) \delta(\phi - \phi_k). \quad (5.5)$$

Note that $f(\theta, \phi)$ is completely defined by parameters (θ_k, ϕ_k) of the K orientations located in the SV. In the next step, the coefficients of the SH expansion of f are determined.

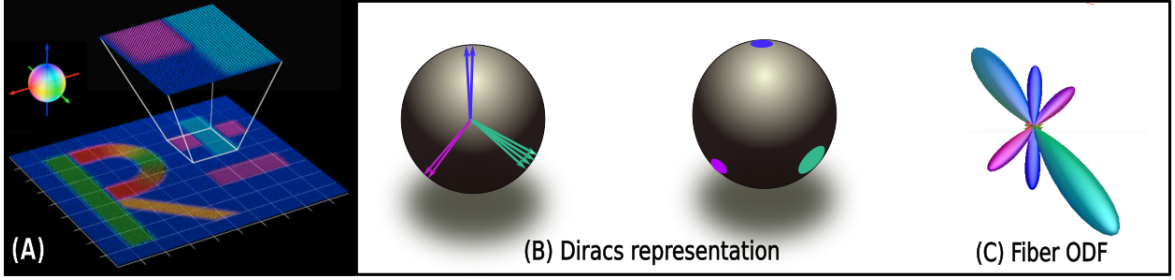


Figure 5.1: Analytical FOD reconstruction: (A) Super-voxel (SV) definition from high-resolution 3D-PLI data fiber orientation map, image taken from (Axer et al., 2016), (B) each orientation in the SV is modeled as Dirac, and aFOD as sum of these Diracs on the unit sphere, and (C) SH expansion of the aFOD in the defined SV.

Computation of the SH coefficients Unlike Axer et al. (2016) who used a linear least square method to obtain the coefficients of the SH expansion, we directly recover the coefficients that uniquely define our analytical FOD f by computing the spherical Fourier transform through Eq. (5.3) since we know the parameters (θ_k, ϕ_k) of all fiber orientation vectors determined from 3D-PLI analysis (Axer et al., 2011a; Jouk et al., 2000; Alimi et al., 2017b), in a given super-voxel. That is,

$$\begin{aligned} c_{lm} &= \int_{\mathbb{S}^2} f(\mathbf{w}) \overline{Y_l^m(\mathbf{w})} d\mathbf{w} \\ &= \int_0^{2\pi} \int_0^\pi f(\theta, \phi) \overline{Y_l^m(\theta, \phi)} \sin \theta d\theta d\phi \end{aligned}$$

then f is replaced by the collection of Diracs in Eq. (5.5) and Y_l^m by its expression in Eq. (5.1) to get

$$\begin{aligned} c_{lm} &= \frac{N_l^m}{K} \sum_{k=1}^K \int_{-1}^1 \delta(\cos \theta - \cos \theta_k) P_l^m(\cos \theta) d \cos \theta \\ &\quad \times \int_0^{2\pi} \delta(\phi - \phi_k) e^{-jm\phi} d\phi \end{aligned}$$

where $N_l^m = \sqrt{\frac{2l+1}{4\pi} \frac{(l-m)!}{(l+m)!}}$, and finally applying the sifting property of the Diracs gives

$$\begin{aligned} c_{lm} &= \frac{1}{K} \sum_{k=1}^K N_l^m P_l^m(\cos \theta_k) e^{-jm\phi_k} \\ &= \frac{1}{K} \sum_{k=1}^K \overline{Y_l^m(\theta_k, \phi_k)}. \end{aligned} \quad (5.6)$$

This solution for the c_{lm} is the analytical and continuous equivalent of the discrete one approximated for pliODF. Eq. (5.6) yields, with respect to L_{max} , the exact solution which requires no directional histogram and, therefore, all the information from the high-resolution fiber orientation vectors are taken into account in the aFOD computation. Furthermore, it can be evaluated at any L_{max} .

Using Eq. (5.2), consequently, the analytical FOD \mathbf{f} is simply computed through matrix-vector multiplication:

$$\mathbf{f} = \mathbf{Y}\mathbf{c} \quad (5.7)$$

with \mathbf{Y} the SH basis matrix and \mathbf{c} the vector of the analytically recovered SH coefficients. Note that although our reconstruction approach uses the SH to represent the FOD, it is independent of the SH basis used and here the real and symmetric basis defined in (Descoteaux et al., 2007) is considered.

5.3 Methods

5.3.1 Datasets Description

Simulations The simulated 3D-PLI dataset consists of two 3D fiber bundles intersecting at an angle X . A 3D collision check is performed to ensure that the individual fibers do not overlap. For this purpose, the fibers are divided into short segments so that two segments can be checked for a collision. In the event of a collision, the two segments are slowly pushed apart. This happens simultaneously for all colliding objects and is repeated until there is no more collisions.

The 3D models generated in this way are then used for the simulation using SimPLI tool (Dohmen et al., 2015; Menzel et al., 2015) to produce synthetic 3D-PLI datasets illustrated in Fig. 6.2, with technical details in Appendix B. The noise of the CCD camera is modelled by a negative binomial distribution in which the variance σ depends on the expected light intensity μ by $\sigma = 3\mu$ as in (Schmitz et al., 2018). From the generated 3D-PLI signal, high-resolution orientations are reconstructed based on the approaches in (Axer et al., 2011a; Schmitz et al., 2018). The generated data consists of a single slice of $60 \mu m$ thick, with a pixel resolution of $64 \times 64 \mu m^2$.

Human brain data The processed experimental data was taken from a human brain. It contains a series of 50 consecutive coronal sections of the occipital lobe from the right hemisphere. Each section has a thickness of $70 \mu m$ which was measured with a pixel size of $64 \times 64 \mu m^2$, analyzed pixel-wise for its fiber orientations and registered onto an image of the brain block before sectioning. This “post mortem human tissue sample used for this study was acquired in accordance with the local ethic committee of our partner university at the Heinrich Heine University Düsseldorf. As confirmed by the ethic committee, postmortem human brain studies do not need any additional approval, if a written informed consent of the subject is available. For the research carried out here, this consent is available”, points out Schmitz et al. (2018) who also give a full description of the dataset.

5.3.2 Performance Evaluation

As aforementioned, the synthetic data describe 2 crossing fiber populations. The crossing angle X ranges from 10° to 90° in 10° increments. The quality of our aFOD reconstruction is assessed according to three criteria: (1) its angular resolution, (2) its angular precision and (3) its robustness to noise. These evaluation metrics are largely used in the dMRI community (Tuch, 2004; Descoteaux et al., 2007; Tournier et al., 2008; Parker et al., 2013; Daducci et al., 2014).

Angular Resolution In diffusion MRI, it is generally assumed that the local maxima or peaks of the FOD coincide with the fiber directions (Tournier et al., 2004; Tuch, 2004; Descoteaux et al., 2007). Here, the angular resolution corresponds to the critical angle τ under which the *peaks* of the two crossing fiber bundles are confounded, that is, they can not be detected separately. To find the peaks of the fiber ODF, the *sh2peaks*¹ algorithm implemented in Mrtrix3 (Tournier et al., 2019) is used, with the minimum peak amplitude set to 0.5 and the other parameters to default.

Angular Precision The angular precision or angular error ϵ is defined as the angular deviation between the peaks of the reconstructed aFOD and the simulated ground-truth. It is evaluated in degrees as follows,

$$\epsilon = \frac{180}{\pi M} \sum_{m=1}^M \arccos(\mathbf{v}_m^T \mathbf{w}_m) \quad (5.8)$$

which is the average distance between \mathbf{v}_m the m^{th} ground truth orientation and \mathbf{w}_m the closest of the recovered peak orientations of the FOD and M is the number of fibers in the super-voxel.

Noise Robustness The noise robustness is actually assessed during the estimation step of the high-resolution fiber orientations in 3D-PLI analysis work-flow (Axer et al., 2011a; Kleiner et al., 2012; Wiese et al., 2014; Alimi et al., 2017b; Schmitz et al., 2018), prior to ODF reconstruction. That is, the aFOD reconstruction method does not directly deal with the noise (removal). However, it is still interesting to test our algorithm’s robustness to noise (for completeness). Therefore, we simulate a noisy dataset following Sect. 5.3.1 with 100 separate noise realizations.

¹<https://www.mrtrix.org>

5.4 Results

5.4.1 Simulations

The angular resolution and precision of the aFOD are tested in both noiseless and noisy situations.

Angular Resolution, Angular Precision The angular resolution τ of our analytical FOD, is first evaluated in noiseless synthetic data, representing two intersecting fiber populations. The result is illustrated for crossings $X = 30^\circ, 40^\circ, 60^\circ$ and 90° in Fig. 5.2 which displays the τ as a function of the SH L_{max} . Here, one can see that crossings $X \geq 60^\circ$ are correctly resolved with small $L_{max} = 6$. For $X = 40^\circ$, at least SH order 8 is required, and for angles as acute as $X = 30^\circ$, SH order 12 is necessary. These observations are quantified in Table 5.1 bellow.

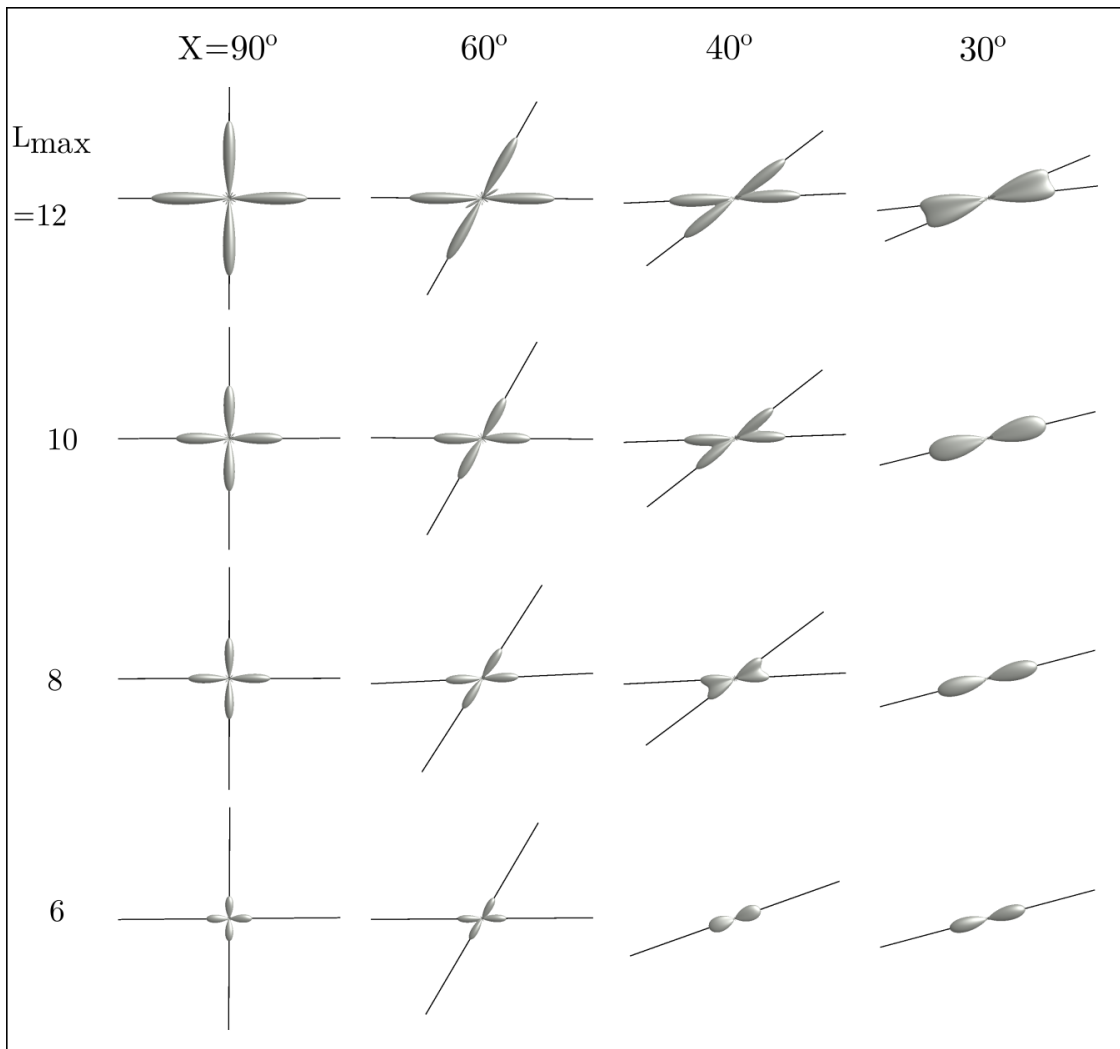


Figure 5.2: Angular resolution of the computed aFOD as a function of the spherical harmonics order L_{max} in noise-free simulations.

Table 5.1 reports quantitatively both the angular resolution τ of the computed aFODs

from noise-free data and the associated angular precision ϵ in degrees. τ improves from 50° down to 30° when L_{max} increases from 6 down to 12. However, ϵ generally ameliorates when τ is higher while being pretty low, with a highest value < 7 degrees. One will notice that when $L_{max} = 6$, the angular resolution is actually found at $X = 50^\circ$ instead of 60° as shown in Fig. 5.2 for illustrative purpose.

L_{max}	Angular Resolution	Angular Precision
6	50°	0.91°
8	40°	2.98°
10	40°	2.00°
12	30°	6.83°

Table 5.1: The angular resolution improves with L_{max} in noise-free setting and the precision is generally high i.e. low angular deviation.

Noise Robustness The effect of noise on angular resolution τ and precision ϵ of the recovered aFOD is presented in Table 5.2 which reports τ and mean \pm standard deviation of corresponding ϵ in degrees over 100 noise realizations. To assess this effect, we compare with quantitative results obtained from noise-free simulations shown in Table 5.1. It can be observed in general that the simulated noise does not introduce any significant bias in either (1) the angular resolution of the aFOD since τ is preserved in each of the 100 noise realizations with respect to L_{max} or (2) its angular precision as the average ϵ is approximately between 1° and 5° , with maximum standard deviation $< 0.2^\circ$.

Note, however, that the acute crossing $X = 30^\circ$ is actually resolved at harmonics order $L_{max} = 12$ but with a 85% success rate and an average angular precision $\epsilon \approx 10^\circ$. Table 5.2 though only presents results with 100% success rate. Therefore, higher order $L_{max} = 14$ is shown instead, with a mean angular precision of roughly 5° and standard deviation of 0.18° .

These observations about the presence of noise on τ and on ϵ of reconstructed aFOD are illustrated in Fig. 5.3 for the specific case where $L_{max} = 8$ and $X = 30^\circ, 40^\circ, 60^\circ$ and 90° .

L_{max}	Angular Resolution	Angular Precision
6	50°	$1.27^\circ \pm 0.08^\circ$
8	40°	$3.57^\circ \pm 0.11^\circ$
10	40°	$2.21^\circ \pm 0.06^\circ$
12	40°	$2.28^\circ \pm 0.03^\circ$
14	30°	$4.88^\circ \pm 0.18^\circ$

Table 5.2: Angular resolution and associated mean and standard deviation angular precision in relation to L_{max} in noisy data.

Black crosses display the orientations of the 2 fiber bundles recovered from 100 times generated noisy crossings, and the red dots represent the ground truth orientations. Our analytical technique can resolve two fiber bundles unless the crossing angle is too small ($X = 30^\circ$), and it definitely preserves the angular precision with the largest average deviation $\epsilon = 3.57^\circ \pm 0.11^\circ$ when $\tau = 40^\circ$. Note, however, the very narrow and negligible dispersion of the recovered orientations in $[-1, 1]$ degrees as compared to the ground truth.

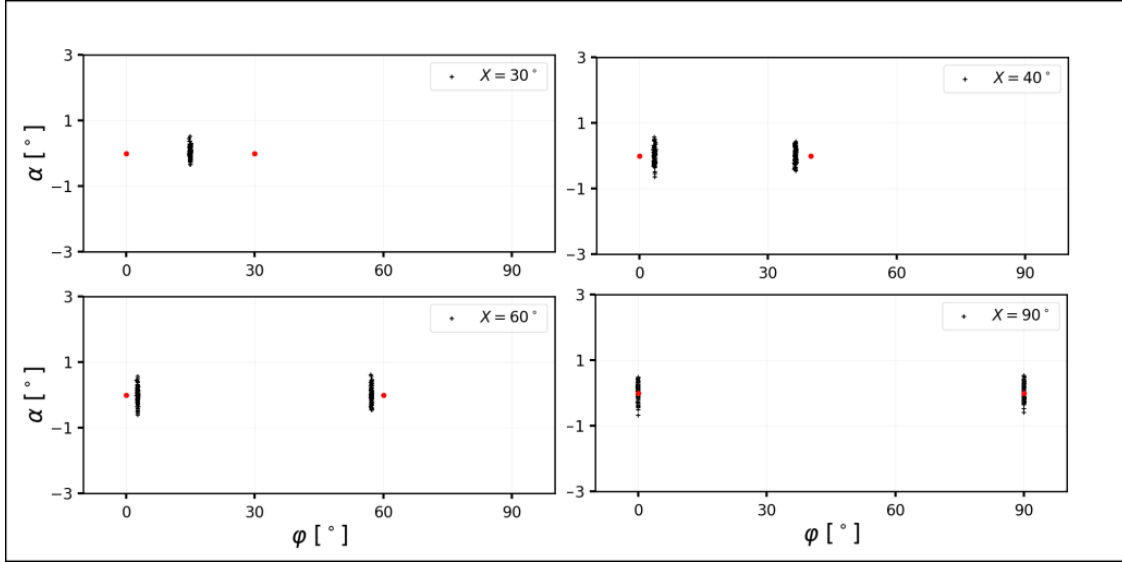


Figure 5.3: Recovered orientations (α, φ) of 2 crossing fiber bundles from 100 noisy simulations in black crosses. The red dots represent the ground truth. The SH order is $L_{max} = 8$.

5.4.2 Human Brain Data

The coronal brain slices with a pixel size of $64\mu m$ isotropic presented in Sec. 5.3.1 are used here to illustrate the ability of the analytical method to compute FODs from real 3D-PLI data at different imaging scales, while bridging the resolution gap (with diffusion MRI). The corresponding FOM contains $1350 \times 1950 \times 50$ native voxels ².

As described in the famous histological preparations of [Sachs \(1892\)](#), and more recently supported by the dissection study by [Vergani et al. \(2014\)](#), the occipital lobe consists of a rich/full network of intralobar fibers.

Stratum sagittale Fig. 5.4 shows a FOD map of the stratum sagittale (SS) which are longitudinal fibers, lateral to the ventricles. The subplot (A) displays the retardation map ([Axer et al., 2011a](#)) of a high-resolution section and the region of interest (RIO) in yellow containing the SS with FODs in purple oriented mainly out of the plane. From (B) to (D)

²The dataset is actually masked and only 38% of the voxels are considered. These voxels contain the brain tissue.

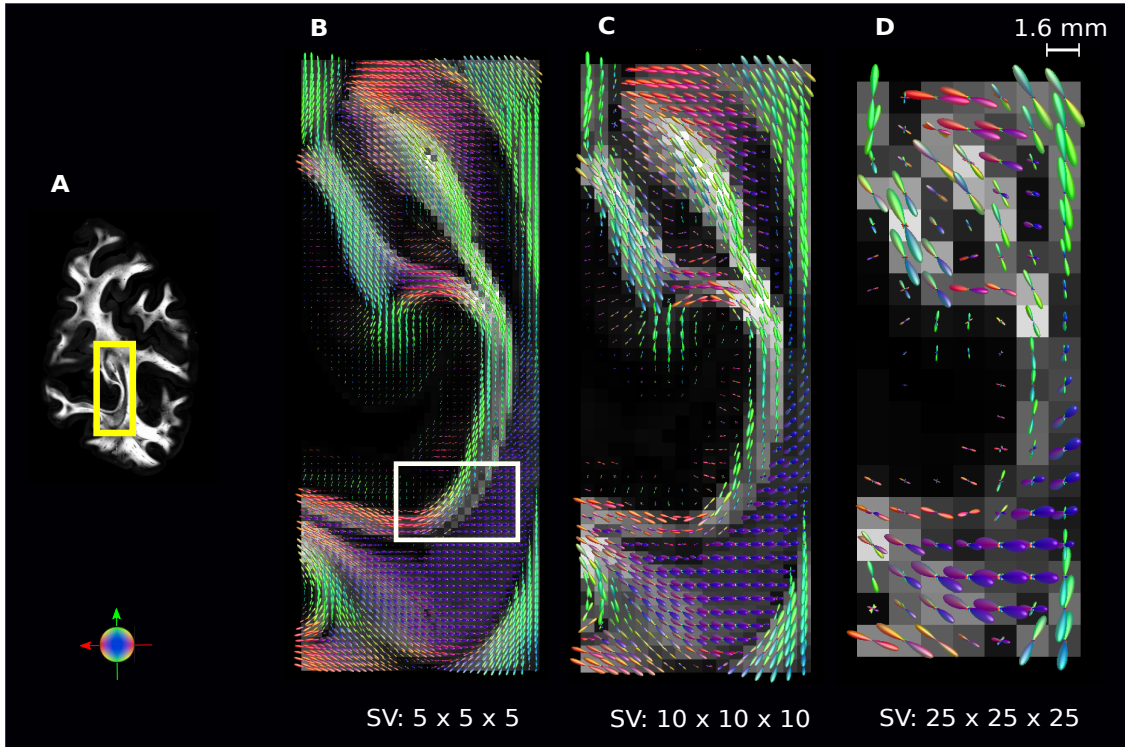


Figure 5.4: Stratum sagittale (SS) in deep WM described by fiber ODFs at different super-voxel sizes i.e. at different spatial resolutions. (A) pictures a high-resolution retardation map while (B) to (D) show the SS at SV size of 5, 10 and 25 isotropic native voxels, respectively. The global fiber organization is preserved through the scales. FODs overlay a recomputed retardation map and are colour-coded according to their local orientation (red: left-right; green: anterior-posterior; blue: inferior-superior). The white rectangular RIO is zoomed in on Fig. 5.6.

the size of the SV varies from 5 to 25 isotropic native voxels while the structure of these deep WM fibers is preserved at each resolution. A zoom in on the white RIO is displayed in Fig. 5.6.

U-shaped fibers FODs of U-shaped fibers also known as short arcuate or integrals are pictured in Fig. 5.5. Here also a high-resolution retardation map is shown in (A) and the ROI in green. (B) to (D) overlaying recomputed retardation maps, show the U-shaped fiber connection of neighbouring gyri at different spatial resolutions while keeping their original high-resolution structure. From these same maps, one can also appreciate the fibers fanning into the gyri.

Diffusion MRI resolution limit Fig. 5.6 displays a zoom in on the FOD map of the stratum sagittale. At high resolution (A), the two layers of the SS are distinguishable as shown by Vergani et al. (2014) in their postmortem dissection of the occipital lobe, even though they mentioned the difficulty to appreciate them on coronal sections. From our

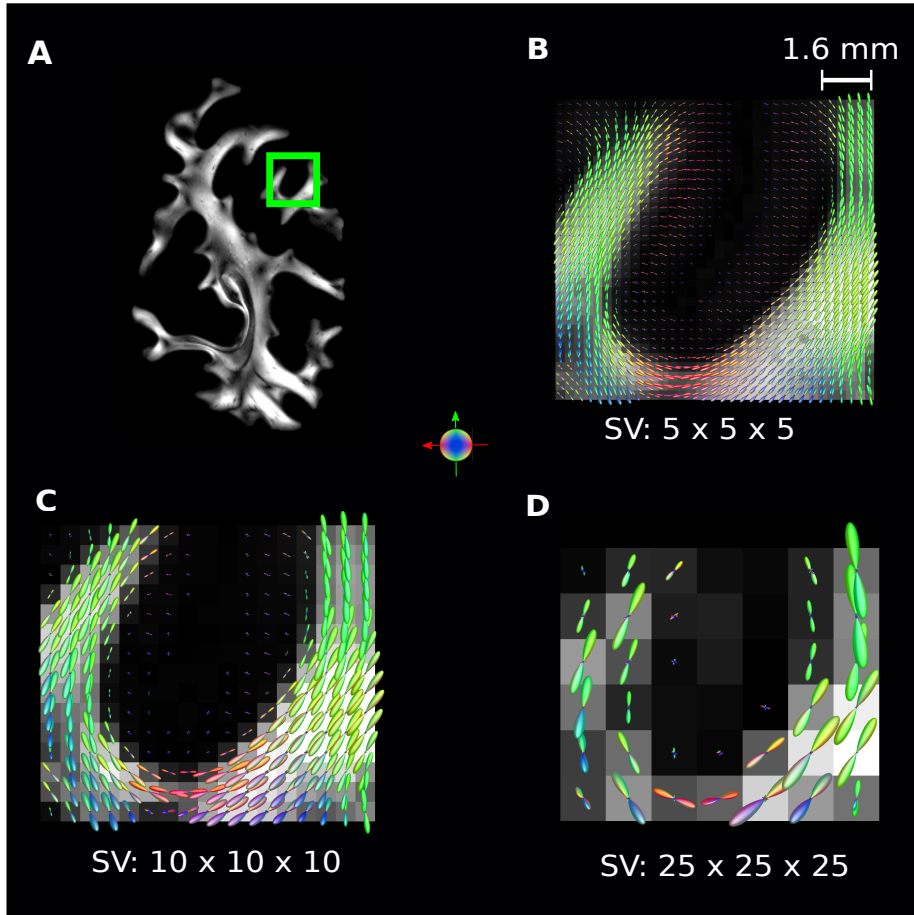


Figure 5.5: FOD map of U-shaped fibers connecting adjacent gyri at varying resolutions from (B) to (D) with a high-resolution retardation map displayed in (A). The global fiber organization is preserved through the scales. FODs overlay a recomputed retardation map and are colour-coded according to their local orientation (red: left-right; green: anterior-posterior; blue: inferior-superior).

FOD maps build from high-resolution 3D-PLI vector data, one can separately identify them up to a coarser resolution of $640 \times 640 \times 700 \mu m^3$ in (C) where the thinner layer intersect another vertical fiber bundle to form crossing FODs.

We can see loss of WM fibers at this scale, suggesting, thus, that higher resolutions of $128 \times 128 \times 140 \mu m^3$ and $320 \times 320 \times 350 \mu m^3$ could be considered as suitable spatial scales for diffusion MRI to reach and apply bundle-specific tractography (Rheault et al., 2019) of the SS. Indeed, using a SH $L_{max} = 6$ at these particular scales, the specific WM tracts of the SS can be tracked, maybe more preferably at SV size of $2 \times 2 \times 2$ equivalent to $128 \times 128 \times 140 \mu m^3$ resolution as observed in our study.

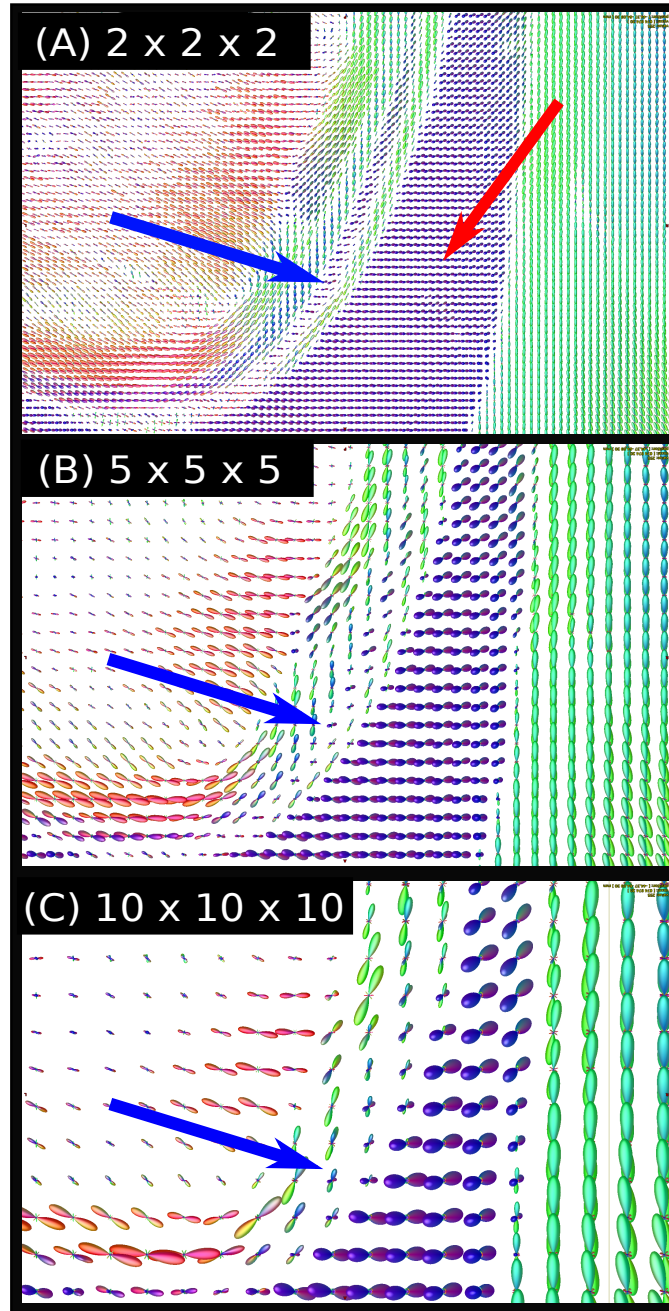


Figure 5.6: Zoom in on the white rectangle of Fig. 5.4: details about the layers of the stratum sagittale. The spatial resolution is $128 \times 128 \times 140 \mu m^3$ in (A), $320 \times 320 \times 350 \mu m^3$ in (B) and $640 \times 640 \times 700 \mu m^3$ in (C). The blue and the red arrows point the thinner and the more pronounced layers of the SS, respectively. By reducing the scale, the thinner layer form crossing FODs with a vertical fiber bundle.

5.5 Discussion and Conclusion

This chapter has introduced an analytical method to define and reconstruct the fiber orientation distribution aFOD from high-resolution 3D-PLI orientation vector data. Its performance is tested and validated on both rich synthetic and human brain 3D-PLI

datasets.

On aFOD approach and main advantage This analytical approach offers different advantages.

It does not need any discretized directional histogram to model the distribution of the 3D high-resolution fiber orientations located in a given super-voxel (SV). Instead, each of those fiber orientation is described as a 2D Dirac on the unite sphere, and the aFOD is modeled as the sum of those Diracs. This constitutes an elegant solution for fiber ODF reconstruction from 3D-PLI data since all the provided orientation measurements are taken into account in the computation without the need to empirically build a directional histogram as proposed by [Axer et al. \(2016\)](#). The use of radial histogram leads to loss of orientation information ([Alimi et al., 2017a, 2018b](#)) since only the orientations of centers of its bins are considered.

The aFOD is computationally efficient and simple: once it is continuously described on a spherical harmonics (SH) basis, the coefficients of its SH expansion are efficiently and analytically calculated using the spherical Fourier transform ([Healy Jr et al., 1998](#)) and by the means of the Diracs and, thus, the aFOD is obtained by a simple matrix-vector multiplication. Therefore, no data fitting process is required since, in the designated SV, all the single fiber orientations (α_k, φ_k) which uniquely define the FOD are known from the 3D-PLI fiber orientation determination stage (see Sect. 3.3). Furthermore, this allows our analytical approach to (theoretically) give the exact solution at a given harmonic order and to be computationally very fast as experimentally demonstrated in the next chapter in Sect. 6.4.3.

On Synthetic Data The performance of the aFOD has been investigated via its angular resolution and precision as well as its robustness to noise in synthetic experiments, with considerable findings.

First, the aFOD generally has a high angular resolution. Indeed, in noise-free simulations, the results show that our technique can reliably resolve two fiber bundles crossing at acute angles (X) when estimated at SH order as low as $L_{max} = 6$ for $\geq 50^\circ$ -crossings and (exceptionally) $L_{max} = 12$, for very small 30° -crossing, see Table 5.1. This additionally highlights the ability of the method to improve the angular resolution with increasing SH L_{max} .

Second, the aFOD produces very low angular error or angular deviation when compared to the ground truth. In all combinations of crossings and SH orders, the maximum deviation of the reconstructed noiseless crossings is smaller than 7° at $X = 30^\circ$. These findings are in good agreement with results previously shown in ([Alimi et al., 2018b](#)).

Third, our analytical method provides a FOD solution which is considerably robust to noise. Experiments on noisy datasets reveal no significant bias introduced by noise in either the angular resolution or the precision of the aFOD. Fig. 5.3, though, shows a

very narrow dispersion of the recovered orientations, bringing them out of the plane. This dispersion could be explained by the 3D aspect of the simulated fibers which try to be as realistic as possible: the theoretical inclination of the fibers is zero, however, in actuality they do not all individually remain on the XY-plane and some fibers will be bent as illustrated in Fig. 6.2 causing, thus, the fibers to be diverted in the Z-axis and leading to this negligible ‘dispersion’. This dispersion is still taken into account in the aFOD computation but yet has a very insignificant influence on its performances.

In fact, in this study we simulate the noise caused by the CCD camera in the PLI acquisition setup, and as explained earlier in Sect. 5.3.2, this is largely tackled during the fiber orientation determination process (Axer et al., 2011a; Schmitz et al., 2018; Alimi et al., 2017b). Yet our analytical method is able to give very similar results in both noisy and noiseless configurations.

These synthetic observations indicate that the aFOD, not only reliably resolves the acute angular crossing, but also has a high angular precision and is robust to noise. This is definitely beneficial to tractography applications, as well as multimodal (and multi-scale) analysis with millimeter resolution diffusion MRI.

On Human Brain Data Finally, our analytical algorithm accurately reconstructs the WM fascicles and preserves the global integrity of the WM fiber architecture in the human brain. Indeed, experiments in deep WM region in Fig. 5.4 as well as near the cortex in Fig. 5.5, where the fiber structures are well known (Sachs, 1892; Vergani et al., 2014), show the conservation of the general anatomical organization of the stratum sagittale and the U-fibers at different spatial resolutions. Conversely, further analysis of the SS illustrates the loss of its thinner layer or simply its intersection with a differently oriented fiber population to form more complex fiber configurations. This is visible at a coarse resolution of about $640 \times 640 \times 700 \mu m^3$ in Fig. 5.6C. Whereas at higher resolutions of around $128 \times 128 \times 140 \mu m^3$, both layers can be clearly appreciated. This observation would suggest a potential spatial resolution limit, for diffusion MRI to reach, at which the WM fibers of the SS could be reconstructed and possibly improve their tracking.

Limitations One limitation of representing the analytical fiber orientation distribution in a truncated SH basis is the presence of Gibbs ringing effects as discussed in a recent review by (Dell’Acqua and Tournier, 2019). However, this issue can be resolved or drastically mitigated by introducing an apodized delta function in its definition as proposed by Raffelt et al. (2012) and Dhollander et al. (2014) in diffusion MRI. Another limitation (of this study) is related to the fact that only a single slice of synthetic data was available to test the performance of the aFOD. In future works, more realistic synthetic models accounting for the 3D structure of the neuronal fibers will be considered.

Overall, we proposed an analytical method to define and reconstruct the fiber orientation distribution aFOD from high-resolution 3D-PLI datasets. To this end, the FOD is modeled

as a sum of K 2D Diracs on the sphere and the coefficients of its SH expansion are analytically and efficiently calculated using the spherical Fourier transform and by means of the Diracs. This constitutes an elegant solution for FOD reconstruction from 3D-PLI data, which will further be compared with empirically estimated pliODF ([Axer et al., 2016](#)) in the following chapter.

Chapter 6

Fiber ODF methods in 3D-PLI: performance assessment

3D-PLI allows to map the spatial fiber structure of postmortem tissue at a sub-millimeter resolution, thanks to tissue birefringence property. Thus, from 3D-PLI high-resolution vector data, different approaches have been recently proposed to reconstruct the fiber orientation distribution function. In this chapter, the analytical FOD (aFOD) and the pliODF methods are extensively compared and their performances studied on highly rich synthetic dataset which simulates the geometry of the neuronal fibers and on real brain data. The aFOD is computationally efficient and fast, and has high angular precision and angular resolution while the pliODF, as a discrete method, intrinsically depends on a large number of histogram bins to reach comparable/similar results. Parts of this chapter are submitted for journal publication to Medical Image Analysis.

6.1 Introduction

As aforementioned in this thesis, 3D-PLI provides high-resolution 3D microscopic fiber orientation measurements recovered from unstained histological tissue sections (Jouk et al., 2000; Larsen et al., 2007; Axer et al., 2011a; Reckfort et al., 2015; Alimi et al., 2017b). Therefore, it has been investigated and presented, thanks to its high spatial resolution, as a complementary and potential technique for the validation and guidance of diffusion MRI fiber orientation estimates and tractography (Alimi et al., 2019b). Different methods have recently been proposed to reconstruct the fiber orientation distribution function (fODF) from high-resolution vector data provided by 3D-PLI (Axer et al., 2016; Alimi et al., 2018b, 2019a).

In this chapter, we propose to evaluate the performance of aFOD and pliODF using metrics such as their computational runtimes, and their angular resolution and angular precision on rich synthetic datasets and human brain white matter (WM) 3D-PLI data. Although these evaluation metrics were already tested for the aFOD in the previous

chapter, they are performed here again on a new and more realistic synthetic datasets for both reconstruction methods. We recall that the *FOD* denotes a continuous representation of the fiber ODF (fODF) presented in the first chapter of this manuscript (see Sect. 2.2.3), the *aFOD*, the analytical FOD we introduced in the previous chapter and *pliODF*, the discrete approximation of the fODF from high-resolution 3D-PLI data by [Axer et al. \(2016\)](#). In this chapter, when the term *fODF* is utilized, it refers to both aFOD and pliODF at the same time, unless specified otherwise.

In the rest of the chapter, (1) the aFOD and pliODF reconstruction methods are (briefly) presented, then (2) the used datasets and the different evaluation criteria are described. Finally, results demonstrate (3) the high angular resolution and precision of the aFOD and the dependence of pliODF on its empirical histogram binning to perform similarly, and (4) that the aFOD is computationally very efficient and very fast.

6.2 Reconstruction Methods

Analytical FOD

In our analytical approach introduced in Sect. 5.2, we define each high-resolution tissue fiber orientation as 2D Dirac delta δ function on the unit sphere and the FOD f as a sum of the K Diracs in a given super-voxel,

$$f(\theta, \phi) = \frac{1}{K} \sum_{k=1}^K \delta(\cos \theta - \cos \theta_k) \delta(\phi - \phi_k) \quad (6.1)$$

where the K parameters (θ_k, ϕ_k) completely describe the FOD which is then decomposed on a truncated SH basis $f(\theta, \phi) \approx \sum_{l=0}^{L_{max}} \sum_{m=-l}^l c_{lm} Y_l^m(\theta, \phi)$ with L_{max} being the maximum SH order and c_{lm} the SH coefficients analytically and efficiently computed via the spherical Fourier transform ([Healy Jr et al., 1998](#)) and by means of the Diracs (see Eq. (5.6))

$$c_{lm} = \frac{1}{K} \sum_{k=1}^K \overline{Y_l^m}(\theta_k, \phi_k). \quad (6.2)$$

Worth recalling is this approach is independent of the SH basis used, and that in this thesis, the real and symmetric basis defined by [Descoteaux et al. \(2007\)](#) and presented in Sect. 2.2.2 is considered.

pliODF, a discrete approach

[Axer et al. \(2016\)](#) are the first group to propose an estimate of the fODF from high-resolution 3D-PLI vector data, which they called *pliODF*. For that, the fiber orientation map (FOM) ([Axer et al., 2011a](#)), is divided into super-voxels (SV) as illustrated in Fig. 6.1 and as done in the analytical method. The difference is that [Axer et al. \(2016\)](#) create a normalized directional histogram on the unit sphere which is subdivided into planar bins in order to discretize the distribution of the fiber orientations. This results in

an empirical orientation distribution density $p(\theta, \phi)$ which is then approximated using truncated spherical harmonics, $p(\theta, \phi) \approx \sum_{l=0}^{L_{max}} \sum_{m=-l}^l c_{lm} Y_l^m(\theta, \phi)$. The pliODF is thus obtained by determining the SH coefficients via a linear least square method by minimizing $\|\mathbf{h} - \mathbf{Y}\mathbf{c}\|^2$, yielding

$$\mathbf{c} = (\mathbf{Y}^T \mathbf{Y})^{-1} \mathbf{Y}^T \mathbf{h} \quad (6.3)$$

where, in matrix format, \mathbf{Y} is the SH basis matrix, \mathbf{h} the vector entries of the directional histogram, and \mathbf{c} the coefficients vector of the expansion up to order L_{max} . This solution, consequently, gives a discrete approximate of the empirical fODF. The real and symmetric SH basis (Descoteaux et al., 2007) is used for its implementation in this study.

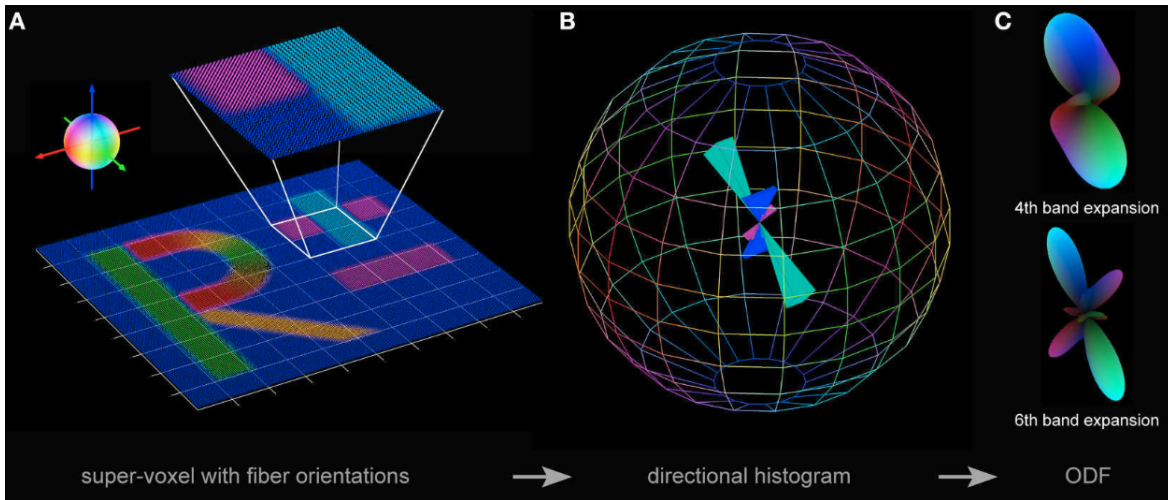


Figure 6.1: pliODF generation steps. (A) High-resolution FOM is divided into regular domains or super-voxels (SV). (B) Then for each SV, a normalized directional histogram is created on the unit sphere with a discretized binning. (C) Finally, the directional histogram is approximated using a spherical harmonics expansion to give pliODFs with features dependent on L_{max} . Step (A) is common to both pliODF and aFOD. Image taken from (Axer et al., 2016).

6.3 Performance Assessment

6.3.1 Synthetic Data Experiments

Simulation The synthetic dataset is generated using the process described in the previous chapter (Sect. 5.3.1) where, however, only a single slice of $60 \mu m$ thick was simulated. Here, we take full advantage of the 3D functionality of the simulator (Matuschke et al., 2019) to generate 10 slices of data, with a pixel resolution of $64 \times 64 \mu m^2$. This results in more realistic tissue fibers as illustrated in Fig. 6.2. More details on the fiber generation process can be found in Appendix B.

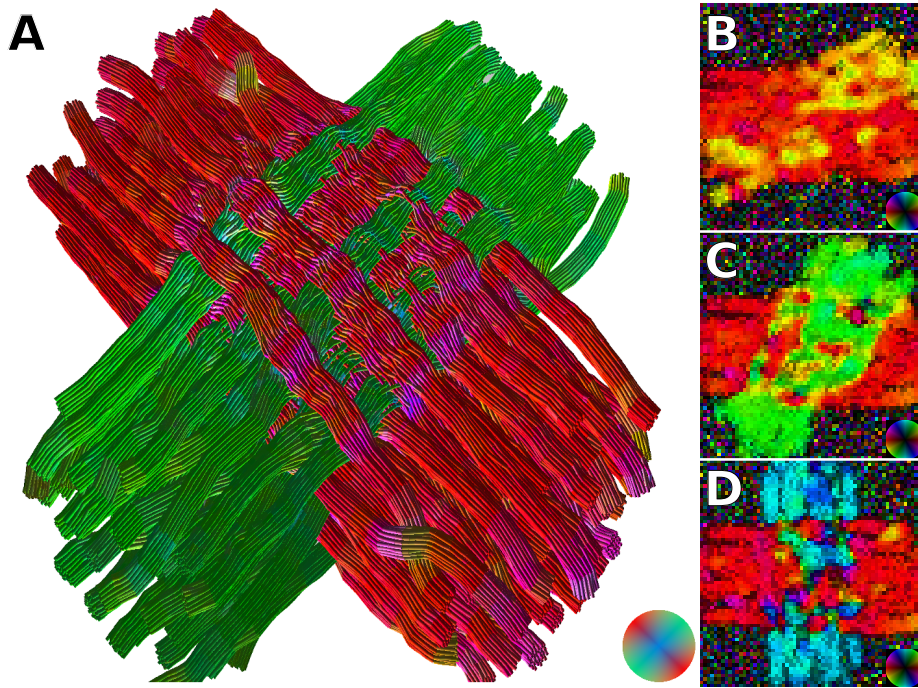


Figure 6.2: (A) 3D visualization of the simulated fiber bundles crossing at angle $X = 90^\circ$. (B)-(D) The resulting Fiber Orientation Maps of 3D-PLI simulations through $60 \mu\text{m}$ sections with a crossing at $X = 30^\circ, 60^\circ$ and 90° , respectively.

Angular Precision Let ‘single fiber’ denote a bundle of coherently organized/oriented fibers. The angular precision ϵ is the deviation or angular error of the peak of the reconstructed fODF from the simulated ground-truth. Here we investigate the ϵ of both aFOD and pliODF, as well as the effect of the directional histogram bin width on ϵ . As in the previous chapter (Sect. 5.3.2), the angular precision ϵ is calculated in degrees as follows,

$$\epsilon = \frac{180}{\pi M} \sum_{m=1}^M \arccos(\mathbf{v}_m^T \mathbf{w}_m) \quad (6.4)$$

which is the average distance between \mathbf{v}_m the m^{th} ground truth orientation and \mathbf{w}_m the closest of the recovered peak orientations of the fODF and M is the number of fibers in the super-voxel.

Angular Resolution It gives the critical angle τ under which the peaks of the two crossing fiber bundles can not be distinguished. Noise-free data are generated with the crossing angles X ranging from 0° to 90° in 10° increments. To find the peaks of the fODF, the *sh2peaks*¹ algorithm implemented in Mrtrix3 (Tournier et al., 2019) is used with the minimum peak amplitude set to 0.5 and the other parameters to default.

¹<https://www.mrtrix.org>

6.3.2 Human Brain Data Experiments

The 50 coronal brain slices with a pixel size of $64 \mu m$ isotropic which are presented in Sect. 5.3.1 are used again here to test the computational speed of the reconstruction algorithms and to assess the shapes of the fODF computed in the stratum sagittale (SS) located in the right occipital lobe. The full FOM contains $1350 \times 1950 \times 50$ native voxels².

Computational Runtimes In order to ensure a fair comparison and due to the large size of 3D-PLI human brain data, both reconstruction algorithms are performed on the *JURECA* (Jülich Supercomputing Centre, 2016) supercomputer at Forschungszentrum Jülich, in Germany. The supercomputer consists of 1872 compute nodes and each node is equipped with two Intel Xeon E5-2680 v3 Haswell 24-core processors operating at 2.5 GHz. The considered compute nodes contain 128 GB of main memory each, and their number is set to 5, for a total of 120 cores in order to keep the compute time in an acceptable range. The super-voxel size and the spherical harmonics bandlimit L_{max} are taken as parameters, plus the histogram bin size for the pliODF generation.

6.4 Results

6.4.1 Single Fiber Orientation

We recall that *single fiber* refers to a single bundle of fibers. Fig. 6.3 depicts, using this simulated single fiber dataset, the fODF angular precision ϵ from both methods as a function of the directional histogram bin size in degrees. The red dotted curve represents the ϵ of pliODF while the green horizontal line is the constant ϵ of analytical FOD. The ϵ of discrete pliODF converges to the ϵ of aFOD as the bin size decreases, regardless of the considered spherical harmonics L_{max} , see (A) to (C). Moreover, in (D) is zoomed in the blue square in (C) to show that with $L_{max} = 12$ and small bin sizes ($< 5^\circ$), both pliODF and aFOD have angular precision smaller than 1° and when the bin size gets smaller, ϵ of pliODF decreases as well. Therefore, in the rest of the experiments, in order to get results closer to our analytical approach, bin widths of 3.6° (consistent with (Axer et al., 2016)) and 1.8° will be considered for the estimation of the pliDOFs.

The previous observations –and choices of bin width– are corroborated in Table 6.1 which quantitatively compares the ϵ of recovered aFOD and pliODF for the single fiber population with varying SH L_{max} . The angular precision of the aFOD is always $\epsilon < 1^\circ$ regardless of L_{max} . This applies to the ϵ of pliODF, except for $L_{max} = 4$ when bin size is 1.8° , and $L_{max} \leq 6$ for a bin width of 3.6° . Note, though, that the pliODF produces more erroneous results (e.g. up to $\epsilon > 30^\circ$) when larger bin width are used (Fig. 6.3).

²Again, the dataset is masked.

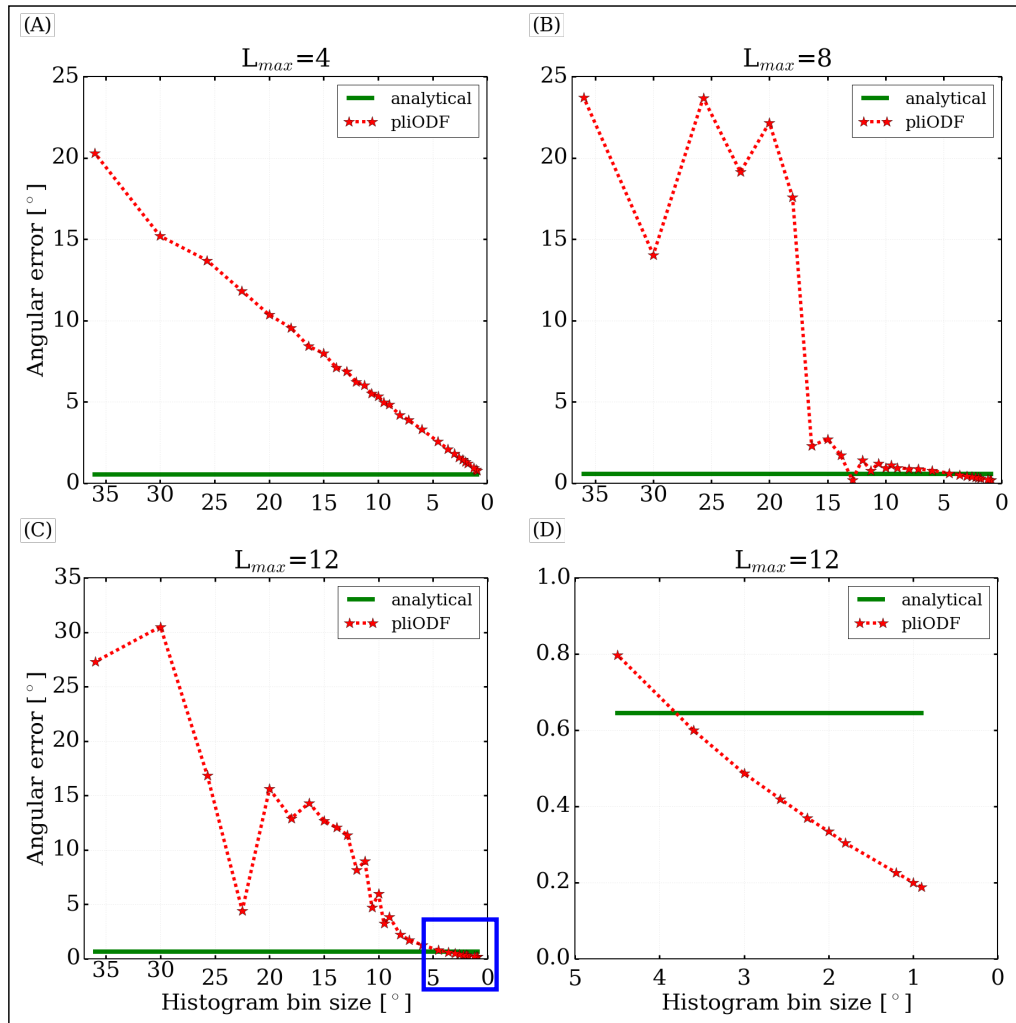


Figure 6.3: Angular precision ϵ of single fiber ODFs as a function of the directional histogram bin size, in degrees. (A)–(C) For decreasing bin size, the ϵ of pliODF (red dotted line) converges to the constant $\epsilon < 1^\circ$ of aFOD, in green horizontal line. At $L_{max} = 12$, when bin size is very small, for both fODFs $\epsilon < 1^\circ$, this is illustrated in (D) where the blue square in (C) is zoomed in.

6.4.2 Crossing Fiber Orientations

Angular Resolution Fig. 6.4 displays the angular resolution of both aFOD and pliODF relative to L_{max} . It can be observed that 90° -crossings can be separated at any SH $L_{max} \geq 4$, and at least $L_{max} = 6$ is necessary to discriminate 60° -crossings and $L_{max} = 10$ for 40° -crossings. These observations are valid for the aFOD as well as the pliODF with the selected bin widths, though only results for bin size 3.6° are shown for illustration. Moreover, one can also notice shape differences between the aFOD and the pliODF at 40° - and 60° -crossings.

Angular Precision Fig. 6.5 displays the angular precision ϵ of the fODF reconstructed from crossing fiber bundles using both methods at different spherical harmonics L_{max} .

L_{max}	Angular Error ϵ [°]		
	analytical FOD	pliODF (1.8°)	pliODF (3.6°)
4	0.55°	1.33°	2.12°
6	0.57°	0.78°	1.24°
8	0.59°	0.34°	0.52°
10	0.62°	0.03°	0.09°
12	0.64°	0.33°	0.60°

Table 6.1: Single fiber angular precision ϵ in degrees [°] as a function of L_{max} . For aFODs ϵ is always $< 1^\circ$, and the difference with ϵ of pliODFs is not very significant with regard to the considered bin sizes.

The green curve represents the ϵ of analytical FOD and the red and black dotted curves represent the ϵ of pliODF estimated with bin sizes of 3.6° and 1.8° , respectively. The following observations can be made. First, globally for all algorithms, ϵ decreases as the crossing angle X increases going from around 7° at $X = 40^\circ$ and $L_{max} = 10$ down to less than 1.5° at $X = 90^\circ$ and $L_{max} = 6$. Second, in all combinations of X and L_{max} , the aFODs have a smaller angular error than pliODFs have, except for crossing $X = 40^\circ$ and $L_{max} = 10$ as can be seen in the plot at the right of Fig. 6.5. Third, as for pliODF, the smaller the bin size, the lower the angular error. Finally, as seen qualitatively in Fig. 6.4 for both methods, the crossing at $X = 90^\circ$ can be correctly reconstructed at any SH order with a maximum error $\epsilon = 1.3^\circ$, the $X = 60^\circ$ is resolved when $L_{max} \geq 6$ with maximum $\epsilon < 6^\circ$ and, the $X = 40^\circ$ only when $L_{max} \geq 10$ with maximum error $\epsilon \approx 7^\circ$.

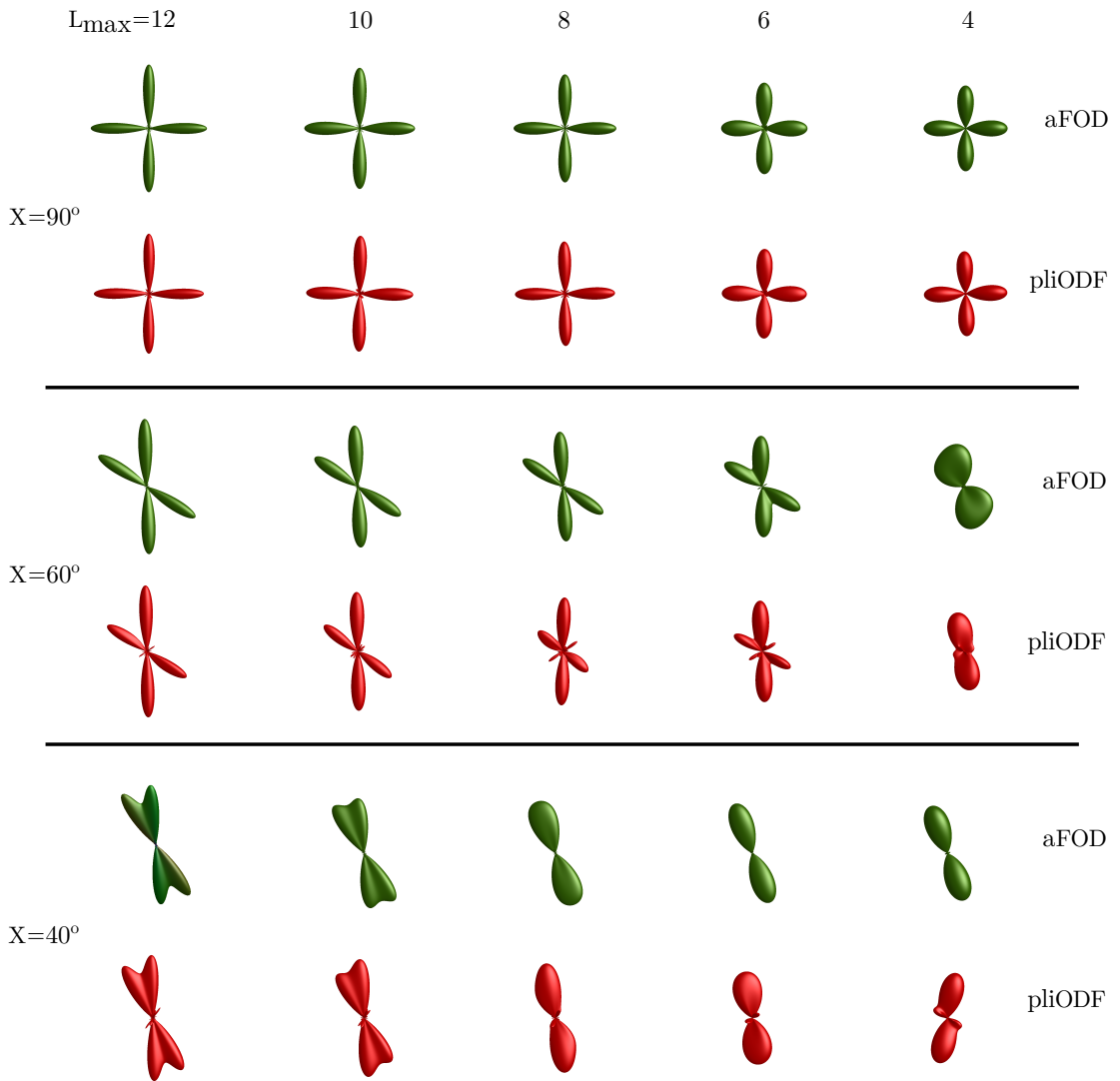


Figure 6.4: Effects of SH L_{max} on the angular resolution of the aFOD and the pliODF with bin size 3.6° estimated at different crossing configurations.

6.4.3 Computational Runtimes

The computational runtime measurements of the fODF are done on the system *JURECA* (Jülich Supercomputing Centre, 2016) and presented in Table 6.3 in minutes:seconds. The test is performed on human brain data consisting of 50 coronal slices of 1950×1350 native voxels³ each. Concerning pliODF, the directional histogram bin size is set to 1.8° , equivalent to 20000 bins in order to get closest results to the analytical solution. The following observations are made. First, the execution time increases with the SH order L_{max} for both reconstruction techniques as previously reported in (Axer et al., 2016; Alimi et al., 2019a). Second, at high resolution, the analytical method is faster than the

³The dataset is actually masked and only 38% of the voxels are considered. These voxels contain the brain tissue.

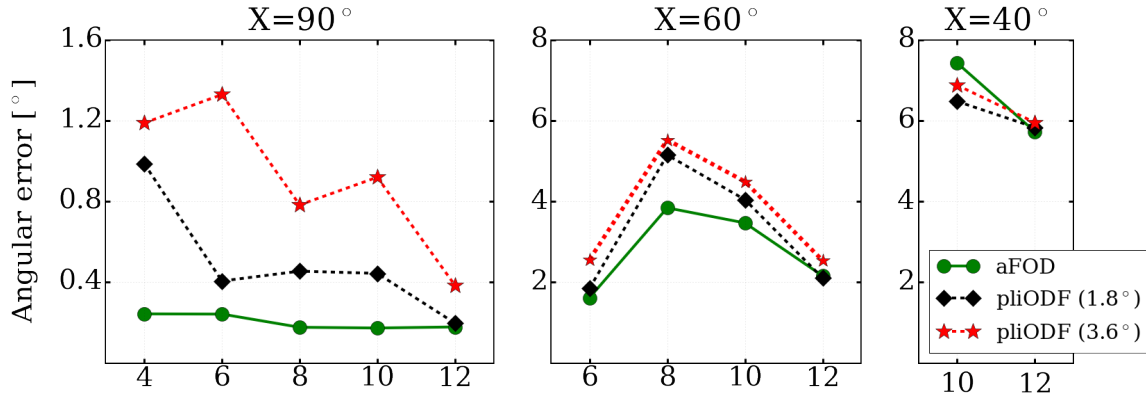


Figure 6.5: Angular precision of the fODF reconstructed at varying SH L_{max} from different crossing fiber configurations X .

pliODF technique by a factor between 24 and 73 at SV size of $5 \times 5 \times 5$ corresponding to $320 \times 320 \times 350 \mu m^3$ resolution (in Table 6.2). Third, when the SV size is > 25 isotropic native voxels, it is 3 to 6 times faster to generate pliODFs than analytical FODs, and both reconstruction approaches are completed within seconds. In between these SV sizes, the analytical solution runs faster. This could be accounted for the continuous setting of the analytical approach, which makes it compute the SH coefficients from every native voxel located in the super-voxel, regardless of its size. However, the discrete pliODF approach estimates the SH coefficients from the defined directional histogram in the considered super-voxel (Axer et al., 2016; Hänel et al., 2017). Therefore, pliODF runs moderately faster when the SV size is large, at least 50 isotropic native voxels since the number of super-voxels in the whole dataset decreases i.e. there is a few directional histograms to estimate the SH coefficients from. Conversely, with a small SV size, the number of super-voxels as well as histograms is large, thus the analytical technique is faster.

6.4.4 Brain Deep White Matter

In Fig. 6.6 is shown an fODF map of the stratum sagittale (SS) which consists of longitudinal fibers (going out of the plane), lateral to the ventricles and located in the deep WM region of the occipital lobe, as seen in the previous chapter (Sect.5.4.2). It can be reported that:

Super-voxel size	Resolution [mm^3]
$1 \times 1 \times 1$	$.064 \times .064 \times .07$
$5 \times 5 \times 5$	$.32 \times .32 \times .35$
$10 \times 10 \times 10$	$.64 \times .64 \times .7$
$25 \times 25 \times 25$	$1.6 \times 1.6 \times 1.75$
$50 \times 50 \times 50$	$3.2 \times 3.2 \times 3.5$

Table 6.2: Imaging spatial resolutions resulting from super-voxels.

	L_{max}	Super-voxel size [in voxels]			
		$50 \times 50 \times 50$	$25 \times 25 \times 25$	$10 \times 10 \times 10$	$5 \times 5 \times 5$
pliODF	4	0:01.23	0:01.57	0:17.29	2:07.52
	6	0:01.90	0:02.89	0:33.50	4:08.71
	8	0:02.92	0:04.98	0:58.72	7:16.63
	10	0:04.26	0:07.71	1:30.81	11:15.95
	12	0:06.00	0:11.10	2:12.14	16:23.47
Analytical	4	0:04.80	0:01.27	0:01.51	0:05.25
	6	0:09.03	0:02.41	0:02.34	0:07.69
	8	0:15.66	0:04.13	0:03.73	0:09.66
	10	0:24.97	0:06.45	0:05.82	0:11.38
	12	0:37.47	0:09.70	0:07.87	0:13.37

Table 6.3: A comparison of runtime measurements in minutes:seconds. All the analytical FODs are run in the order of seconds regardless of the super-voxel size and the SH L_{max} . pliODF takes minutes to run in small sized SV and a few seconds when the resolution is coarser. The execution time generally increases with L_{max} .

1) Going from smaller $SV = 5 \times 5 \times 5$ (B) to larger $SV = 50 \times 50 \times 50$ (C,D), the spatial resolution gets (10 times) coarser ($3.2 \times 3.2 \times 3.5 \text{ mm}^3$, see Table 6.2), however, the global WM tissue structure of the SS is conserved by both the pliODF (C) and the aFOD (D) with crossings. 2) Overall, the shapes of the aFOD and pliODF are very similar, although the latter sometimes presents some spurious lobes at the center of the crossings. 3) The aFOD is more sharply defined as the spherical harmonics L_{max} increases as shown in (E). This observation is also valid for pliODF (but not displayed), with eventual small spurious lobes.

6.5 Discussion and Conclusion

In this chapter, we quantitatively compare the performances of our analytical FOD approach and the pliODF discrete method. We perform experiments both on highly rich synthetic and human brain 3D-PLI datasets.

On Angular Precision, Angular Resolution As pointed out by (Parker et al., 2013), “characterisation of any error in the resolution of the single fiber orientation will provide an easy way of identifying any underlying systematic problems inherent in certain (ODF reconstruction) techniques...”. Thus, both reconstruction techniques are performed on a *single fiber* synthetic model. Results show that, unlike our analytical FOD, pliODF is dependent on the number bins of its discretized directional histogram. This demonstrates

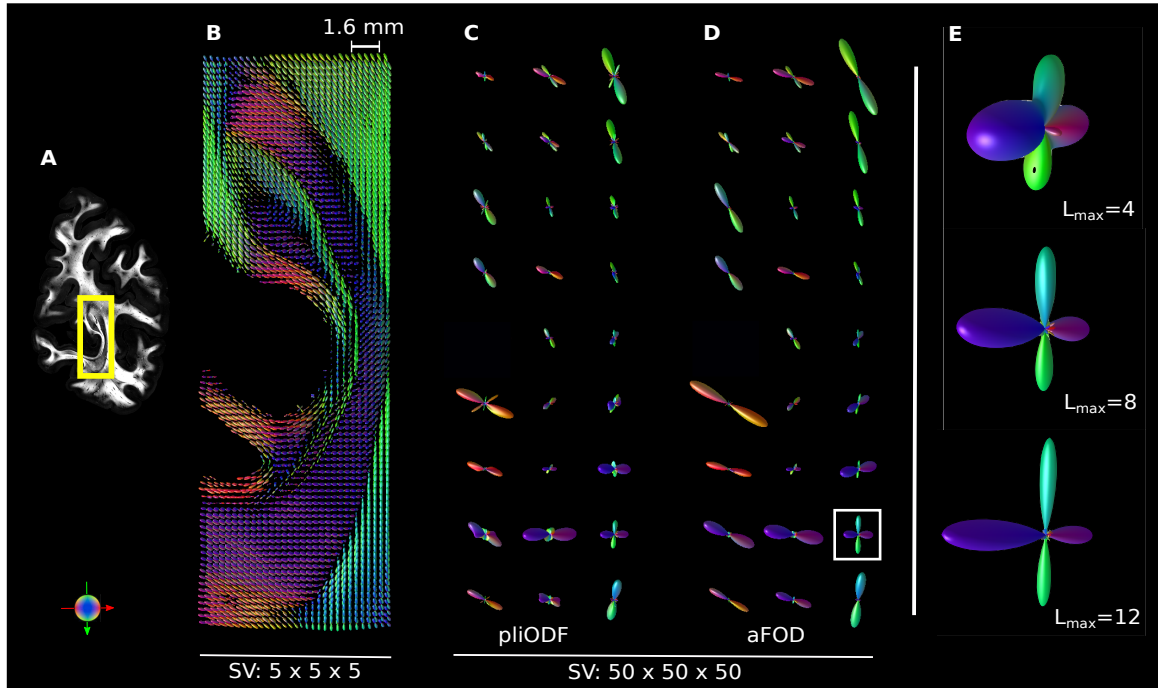


Figure 6.6: Stratum sagittale (SS) in deep WM described by fODF at different super-voxel sizes i.e. at different spatial resolutions. (A) pictures a high-resolution retardation map while (B) to (D) show the SS at SV sizes of 5 and 50 isotropic native voxels. The global fiber organization is preserved through the scales. fODFs are colour-coded according to their local orientation (red: left-right; green: anterior-posterior; blue: inferior-superior). The white square RIO in (D) is zoomed in (E) to present a voxel containing a crossing fiber ODF computed at different SH L_{max} .

that pliODF requires high number of bins to reach results similar to the analytical solution. Indeed, in this experiment (see Sect. 6.4.1), the angular precision ϵ of aFOD is always smaller than 1° while the ϵ of pliODF converges to the aFOD's by decreasing its bin width.

Our aFOD is analytically defined, therefore the produced angular errors in the single and crossing fiber experiments could be explained by the truncation of the spherical harmonics basis as reported in the previous chapter (and by potential biases from the fODF peaks detection method). In the multiple fiber context, except for $X = 60^\circ$ -crossing where ϵ increases when L_{max} goes from 6 to 8, the angular precision improves when the SH truncation order increases, independent of the crossing configuration. In the particular cases of crossing at $X = 0^\circ$ and $X = 90^\circ$, the deviation is always very low, i.e. less than 1° . Moreover, using high SH orders helps sharpen the aFOD (and pliODF with proper bin width) and gives more defined peaks very useful in fiber-tracking applications (Tournier, 2019).

As for pliODF, the presence of angular error can be attributed to the SH basis truncation as well, however, it could be mainly due to its discrete nature. pliODF

by definition uses an arbitrary discretized directional histogram and only provides an approximate of the fiber ODF (Axer et al., 2016), which is the main limitation of the approach. Indeed, the directional histogram is defined by its bin centers and the number of native orientation vectors falling in each bin is dependent on the bin size or corresponding dihedral angle. This could explain the fact that, in the single fiber experiment when the histogram bin size is $< 4^\circ$, pliODF has lower ϵ than aFOD does. In fact, the closer this bin center to the orientation of single fiber ground truth, the smaller the angular error of pliODF. Conversely, the further the bin center, the larger the ϵ as shown in Fig. 6.3 and Table 6.1. In the crossing fiber experiment, results in Fig. 6.5 show again that the aFOD presents less angular deviation than the pliODF.

The use of the discretized directional histogram has also a significant influence on the angular resolution of the pliODF in the crossing fiber experiment, but the bin sizes we have selected (3.6° and 1.8°) are ‘empirically’ chosen so as to get pliODF results close to the aFOD solution. As said earlier, when the bin width gets smaller, i.e. the number of histogram bins gets larger, pliODF is expected to behave as well as our the analytical FOD (Fig. 6.4, Fig. 6.5). Nevertheless, one should be cautious about possible over-binning of the directional histogram which could eventually cause some undesirable effects such as the appearance of spurious lobes (Fig. 6.4, Fig. 6.6) or eventual extended computation runtimes.

As aforementioned, the value of the spherical harmonics order L_{max} determines the maximum achievable fiber ODF angular resolution. By increasing L_{max} , more acute crossing fiber populations could be resolved as shown in Sect.6.4.2. Here again we set the directional histogram bin size and both fODF approaches give very similar angular resolutions τ but aFOD in general demonstrates better angular precision ϵ (Fig. 6.5).

On Noise Robustness In the previous chapter, we tested our analytical FOD computation method on noisy synthetic dataset and it was revealed very little influence of noise on both its angular resolution and angular precision. Moreover, as seen before in Chap. 3 and Chap. 4, the noise in 3D-PLI data comes from the CCD camera and its removal is performed during the estimation of the high-resolution fiber orientation vector (Axer et al., 2011a,b; Kleiner et al., 2012; Wiese et al., 2014; Alimi et al., 2017b; Schmitz et al., 2018). Therefore, the noise robustness test is not repeated here but we can expect pliODF to perform as well as our aFOD does, if the good number of radial histogram bins is used.

On computation runtimes The analytical approach is very fast and computationally efficient. This is due to the choice of defining each fiber orientation as a $2D$ Dirac function on the unit sphere, which simplifies and accelerates the computation of the SH coefficients, analytically. Note that in this study, only a subset of the human brain was analysed. An entire human brain of about 1200 cm^3 has, however, about 100 times more voxels when scanned at $64 \times 64 \times 70\ \mu\text{m}^3$ resolution and it would theoretically last about 100 times

longer to calculate the fODF. Moreover, at a (ultra) higher resolution of $1.3 \times 1.3 \times 70 \mu m^3$ the dataset gets about 2×10^5 times larger and the computations will require more time. We recall that to reach millimeter resolutions, the SV size should be very large, therefore, pliODF runs faster as seen in Sect. 6.4.3 and might still be applicable, given a suitable bin size is used. However, since the calculation time at this scale is already quite fast (seconds for the current dataset) for both techniques, the use of the analytical ODF is advocated, since it gives the exact solution and has no bias of the histogram binning.

On Stratum Sagittale Experiments on human brain WM indicate that both methods of reconstruction conserve the integrity of the anatomical organization of the stratum sagittale (SS) through the spatial scales. This is in agreement with the studies of (Sachs, 1892) and (Vergani et al., 2014) as seen in the previous chapter. It is noticed though that the pliODF sometimes presents some spurious lobes, which could be due to the empirical (over- or under-) binning of the directional histogram: one main limitation of this discrete estimate of the fiber ODF. At high SV size of 50 isotropic native voxels corresponding to imaging resolution of $3.2 \times 3.2 \times 3.5 mm^3$, the SS intersects with neighboring fiber bundles to form crossings which become more sharply defined when the SH L_{max} increases. Indeed, high SH orders improve the sharpness of the FOD as well as its angular precision and resolution as demonstrated in the simulations (Fig. 6.4, Fig. 6.5), and commonly known in diffusion MRI (Tournier et al., 2007; Descoteaux, 2008).

Limitations of the Simulated Data A limitation of the study is related to the available synthetic dataset. The simulated fiber bundles remain in the xy-plane despite the fact that multiple slices of data are generated to give a more realistic representation of the neuronal fibers. In future studies, it would be interesting to perform tests taking into account the inclination angle of the simulated fiber bundles even though the determination of the (absolute) inclination angle remains a challenging and open question so far (Kleiner et al., 2012; Wiese et al., 2014; Alimi et al., 2017b; Schmitz et al., 2018; Menzel, 2018). The brain data though involves the full 3D information about the WM fiber inclination angle.

The observations made from this study could suggest that both fODF reconstruction methods in 3D-PLI could be considered as complementary if, of course, the suitable histogram bin size is used for pliODF. However, finding this suitable bin size remains an empirical task (Axer et al., 2016) which could lead to over-binning (and its undesirable consequences). Therefore, we advocate the use of the analytical approach to compute the FOD in 3D-PLI since it is, in this sens, parameter free, it gives the exact solution and is less prone to angular errors. Now that the accurate fiber orientations can be recovered, our analytical FOD is used, in the next chapter, for fiber-tracking applications.

Chapter 7

Multiscale Analysis: bridging the diffusion MRI–3D-PLI resolution gap

The analytical FOD can be computed at multiple spatial resolutions, as demonstrated in the previous chapters. Here, we perform fiber-tracking and show how tractograms obtained at varied spatial resolutions from 3D-PLI human brain data can be inspected using homology theory in order to carry out their quantitative comparison at different scales. This paves the way for the validation of tractography obtained from diffusion MRI using multiscale fiber tracking based on 3D-PLI. Parts of this chapter are based on the publications ([Alimi et al., 2019b](#), [2020](#)).

7.1 Introduction

Three-dimensional Polarized Light Imaging has been investigated as a potential and adequate tool ([Axer et al., 2016](#)) for the validation of diffusion MRI-based fiber orientation estimation and tractography. As seen in Chap. 3, 3D-PLI is an optical imaging technique which gives high-resolution fiber orientation measurements at micrometer scale. In ([Alimi et al., 2019b](#)), we qualitatively demonstrated that the “global” structural organization of the human brain WM tracts can be preserved while decreasing the spacial resolution, proving, thus, the ability to bridge the resolution gab between diffusion MRI and 3D-PLI via tractography. The study of the *brain fiber network* from the topological point of view has seen an increasing interest in the last years ([Lee et al., 2012](#); [Sizemore et al., 2018](#); [Chung et al., 2017](#)). In this chapter, we show how tractograms obtained at different spatial scales using 3D-PLI human brain data can be inspected using *homology theory* to perform a quantitative comparison between them. In particular, we investigate the persistence of the *number of connected components* in brain networks estimated at different resolutions.

7.2 Methods

7.2.1 Analytical FOD

From 3D-PLI dataset, FODs can be reconstructed at different spatial scales by changing the size of the so-called super-voxel (SV), which allows downsampling the micrometer resolutions up to the millimeter scales of diffusion MRI, see Table 7.2.2. As previously demonstrated in Chap. 5 and Chap. 6, our analytical approach is computationally efficient and allows fast computations of FODs from 3D-PLI data. Here, we integrate this local information to obtain more global information via streamline tractography.

7.2.2 Multi-scale fiber-tracking

By varying the SV size, tractography can be performed at different resolutions ([Alimi et al., 2019b](#)). Seeding from the gray matter-white matter interface (GM-WMi), we obtained 10 million streamlines at each resolution using the iFOD2 algorithm implemented in Mrtrix3 ([Tournier et al., 2019](#)). A weight was associated to each streamline using SIFT2 ([Smith et al., 2015](#)) to re-establish the balance between its density and the fiber density computed from the FODs.

Connectivity matrix The chosen atlas is defined at the GM-WMi with a super-voxel $SV = 100 \times 100 \times 25$, and every voxel of the atlas is considered as different region. In this way, proximity in the atlas is coupled with proximity of assigned labels. Finally, a weighted connectivity matrix was computed at each resolution corresponding respectively to super-voxel sizes $SV_5 = 5 \times 5 \times 5$, $SV_{10} = 10 \times 10 \times 10$ and $SV_{25} = 25 \times 25 \times 25$, using the defined streamline weights and the atlas.

3D-PLI resolution [μm^3]	Super-voxel size SV	dMRI resolution [mm^3]
$64 \times 64 \times 70$	$1 \times 1 \times 1$	$.064 \times .064 \times .07$
	$5 \times 5 \times 5$	$.32 \times .32 \times .35$
	$10 \times 10 \times 10$	$.64 \times .64 \times .7$
	$25 \times 25 \times 25$	$1.6 \times 1.6 \times 1.75$

Table 7.1: Imaging spatial resolutions: from 3D-PLI’s micrometer to diffusion MRI’s millimeters by varying super-voxel dimensions. The tissue consists of 50 coronal sections, for a total of $1350 \times 1950 \times 50$ native voxels.

7.2.3 Homology analysis

Betti numbers The Betti numbers are topological invariants which count the number of topological features such as the *connected components* or 0th Betti number (β_0), the *holes* or 1st Betti number (β_1), the *voids* or 2nd Betti number (β_2), etc, in a given graph as pictured in Fig. 7.1 with associated barcodes for β_0 and β_1 for illustration. Here we focus our analysis on the β_0 .

Graph filtration Associating a weight to each streamline provides an additional information whose incorporation in the network analysis is a challenge (Sizemore et al., 2018). One approach is to set a single threshold on the streamline weights and only consider those above this threshold. But this approach is fairly ad-hoc (Lee et al., 2012; Chung et al., 2017). Here we threshold at levels defined by the unique values of the streamline weights or edge weights in the network and count the number of connected components β_0 at each threshold.

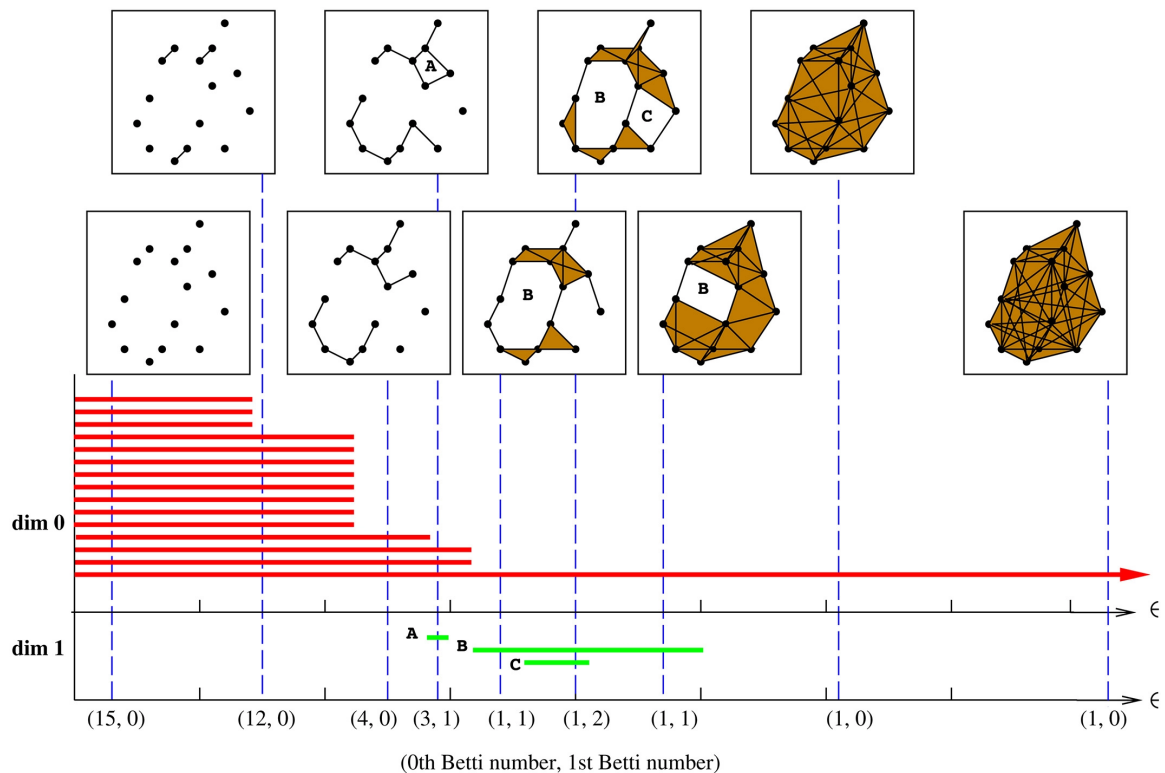


Figure 7.1: The number of connected components i.e. the zeroth Betti (β_0) in red and the number of holes i.e. the first Betti (β_1) in green are encoded in barcodes for varying thresholds (x-axis). Each threshold level, represented by a vertical dashed line, indicates the level of granulation of the graph illustrated in the square at its top. The barcodes are equivalent to the curves in Fig. 7.4. In the remainder of the analysis, the zeroth Betti β_0 and the threshold are the parameters of interest. Image taken from (Hylton et al., 2019).

The analysis of the homology of the obtained networks is performed by measuring the persistence of the β_0 on this natural filtration of the graph. For every SV size, the evolution of the β_0 is given by a *Betti curve* (see Fig. 7.4) to provide an insight on the robustness of β_0 , with respect to threshold.

7.2.4 Human brain dataset

The studied dataset consists of 50 unstained coronal slices from the right hemisphere and previously presented in Sect. 5.3.1. Each slice is $70 \mu m$ thick with an in-plane resolution of $64 \times 64 \mu m^2$. Note that the spatial resolution corresponding to SV_{25} closes the gap with diffusion MRI's *mm* resolution.

7.3 Results and Discussion

Tractography Fig. 7.2 displays the generated streamlines from the 3D-PLI high-resolution up to the relatively low diffusion resolution with, on the left, the transmittance on top and the corresponding WM mask on the bottom. From (A) to (C), the spatial scale decreases whereas the integrity of the brain fiber pathways are preserved.

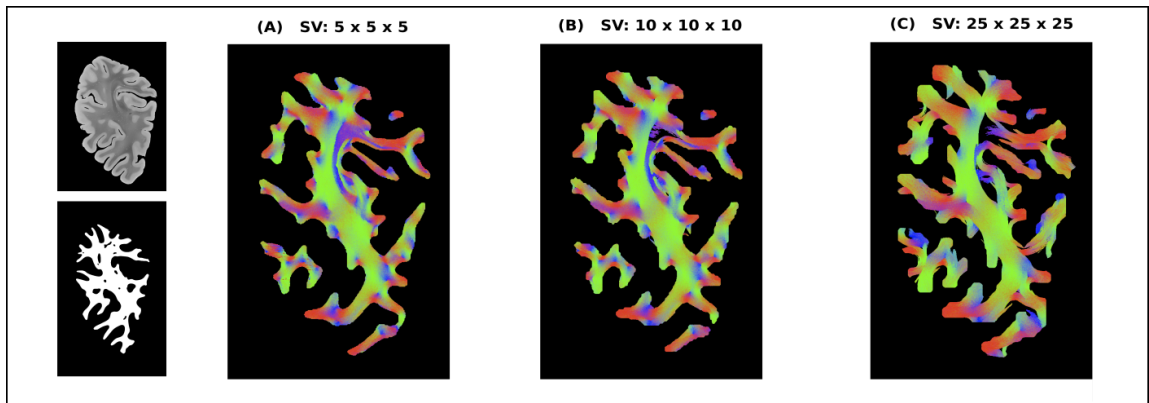


Figure 7.2: Panels (A) to (C) illustrate the streamlines passing through the central coronal slice of the studied dataset with the usual orientation-based colouring. It is possible to notice the different white matter structures that are generated at different SV sizes or resolutions. The figure on the top left is the transmittance image resulting from 3D-PLI analysis and the one on the bottom left is the used white matter mask

Connectivity matrices The first row of Fig. 7.3 shows the connectivity matrices computed at different SV sizes. Notice the pervasive presence of small communities of regions at every resolution. This is due to the existence of many U-fibers in the occipital lobe as described in the histological preparations of [Sachs \(1892\)](#), more recently supported by the dissection studies of [Vergani et al. \(2014\)](#). Moreover, the second row illustrates the sparsity pattern of the weighted connectivity matrices, highlighting the presence of weaker connections

between further regions. These weaker connections are more present in the connectome computed at the lowest resolution, at SV_{25} .

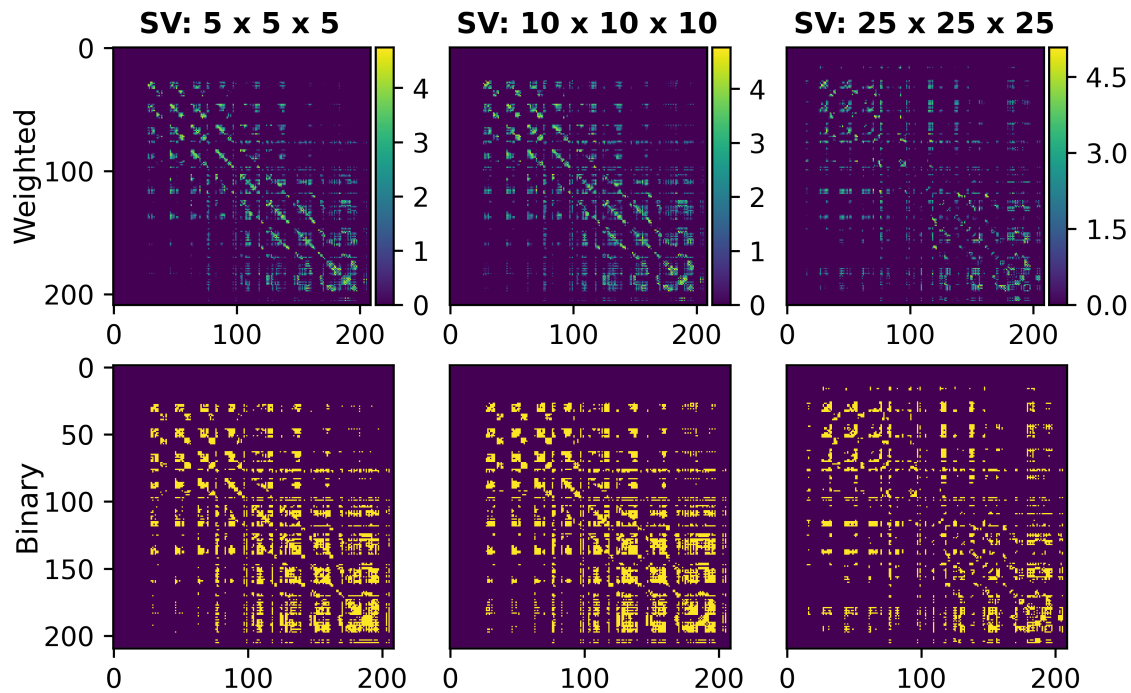


Figure 7.3: The first row shows the weighted connectivity matrices corresponding to the tractograms obtained at the three studied resolutions or super-voxel sizes SV_5 , SV_{10} and SV_{25} . The second row shows the sparsity pattern of the connectomes from the first row.

Homology analysis Fig. 7.4 pictures the evolution of the 0th Betti number β_0 with respect to the thresholding level applied to the matrices. The value of β_0 for the original connectomes (threshold equal to 0) is 67, 64 and 63 for the highest (SV_5), intermediate (SV_{10}) and lowest resolution (SV_{25}), respectively. Since each region of the atlas is composed of one single voxel ($SV = 100 \times 100 \times 25$), these differences correspond to minimal changes in the tractograms and should not be interpreted as structural differences caused by the diverse SV sizes. Up to a threshold level of around 15000 units the three Betti curves have a similar behaviour, showing how thresholding at low levels does not affect the comparability of the β_0 features of the connectomes. On the contrary, as soon as the 15000 units level is reached, the number of connected components in the tractogram computed from the highest resolution (SV_5) increases much faster than its homologous in the other two connectomes. The comparability is restored for high threshold values, where the connectome is reduced to a graph made, almost uniquely, of isolated nodes. This case is not interesting for our comparison and is included only to show the correct termination of the analysis.

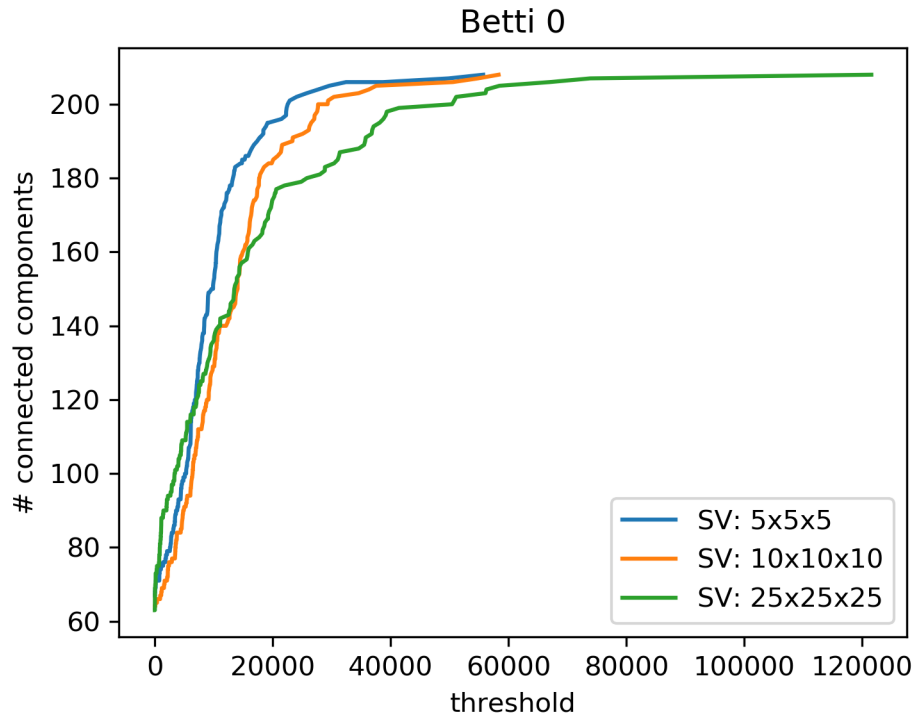


Figure 7.4: The β_0 curves associated to the connectomes obtained at specific SV sizes. The value of the three curves at zero threshold is 67 for the resolution corresponding to SV_5 , 64 for SV_{10} and 63 for SV_{25} . The fact that the three curves terminate at different thresholds occurs because the maximal entry in the respective connectivity matrix is different for each connectome.

7.4 Conclusion

Our results indicate that the connectomes obtained at different resolutions are endowed with a topological structure which is very similar with respect to the number of connected components. Nevertheless, the study of the persistence of the number of connected components suggests that analogies in β_0 between connectomes computed at different resolutions may be observed only if the corresponding networks are thresholded up to a relatively small value, hence taking into account both the stronger and the weaker connections regardless of the chosen spatial resolution. Thus, high-resolution 3D-PLI-based tractography and the topological invariants β_0 can be used to guide diffusion MRI fiber-tracking of the human brain WM. Note, however, that this study deals with a 3D-PLI dataset acquired only from the occipital lobe of a single hemisphere of the brain. Further investigations involving the whole brain connectome would definitely be more informative and conclusive. Nevertheless, this work paves the way for multimodal tractography quantitative analysis between diffusion MRI and 3D-PLI at different spatial scales.

Part IV

Conclusion

Chapter 8

Conclusion

Contributions

In this thesis, we investigated three-dimensional polarized light imaging (3D-PLI) and the possibilities to close the spatial resolution gap with diffusion MRI and metrics for quantitative comparison of the tractograms obtained from each modality. This sets the foundations for multimodal brain imaging analysis across the scales.

To this end, we began with introducing some background knowledge on both diffusion MRI and 3D-PLI. We started with an overview on the principles of diffusion MRI and its common methods to estimate the local fiber information and to integrate them through fiber-tracking. Then, the physics of 3D-PLI is presented as well as means to acquire its signal and how to analyse it in order to obtain the high-resolution fiber orientations.

During our introduction to 3D-PLI, we found out an inherent issue to this optical imaging technique: the sign ambiguity of the inclination angle. A PDE-based image restoration approach is proposed, therefore, to restore the inclination sign for the accurate reconstruction of the fiber orientation in each native voxel. Satisfying results have been obtained from experiments on both synthetic and human heart data.

We then introduced an analytical approach to calculate the fiber orientation distribution function (FOD) from these 3D-PLI high-resolution fiber orientations and use the super-voxel to navigate across the scales. Results demonstrated that our method is computationally efficient and very fast as compared to the discrete pliODF approach, outperforms this latter and gives the exact solution for the FOD.

Finally, using our analytical FOD, we performed 3D-PLI-based fiber-tracking at multiple scales. Results showed the preservation of the global architecture of white matter fascicles in the right occipital lobe of the human brain. This is confirmed quantitatively by application of homology theory via comparison of the associated connected components of the tractograms obtained at different resolutions.

Perspectives

Our first contribution in this thesis concerns the restoration of the sign of 3D-PLI inclination angle. Note that there is still an open question about the determination of the inclination angle (Wiese, 2016; Schmitz et al., 2018; Menzel, 2018). A great avenue would be to investigate how to analytically reconstruct the inclination angle itself and avoid the sign ambiguity at the same time. This would be very useful, especially for super high resolution PLI imaging (Axer et al., 2011b) where the in-plane resolution is $1.3 \mu m^2$ while the thickness of the tissue slices is around $70 \mu m$.

Now that the foundations for multimodal and multiscale analysis between 3D-PLI and diffusion MRI are set, an important perspective is to acquire images using both MRI and PLI from the SAME human brain (or heart). Ex-vivo MRI acquisitions must be done before applying invasive PLI measurements to the tissue. From this point, the perspectives of our work are manifold and future studies could be focused on:

- Multimodal FODs registration using spherical harmonics' rotation invariances (Zucchelli et al., 2020) as metric on a half or full brain dataset.
- Fiber-tracking assisted by high-resolution 3D-PLI information to improve, complement or validate diffusion MRI tractography.
- Full brain tractograms generated from 3D-PLI dataset at different resolutions, to be used as potential ground-truth for diffusion MRI and other imaging techniques.

This thesis work can also have some perspectives in the emerging diffusion *microstructure imaging*. For instance, multimodal fiber orientation dispersion can be investigated using, maybe, the FODs computed from both modalities and described on spherical harmonics basis.

Appendices

Appendix A

Regularizing the pliODF

Regularizing the ODF Estimate with the Laplace-Beltrami operator in 3D Polarized Light Imaging

Abib Alimi

Samuel Deslauriers-Gauthier

Rachid Deriche

Université Côte d’Azur, Inria, France

Introduction

3D-Polarized Light Imaging (3D-PLI) is an optical approach that utilizes the birefringence in postmortem organs (brain/ heart) to map their spatial fiber structure at a submillimeter resolution [1]. Recently, Axer et al. [2] proposed a strategy to bridge it to relatively low diffusion MRI spatial resolution by introducing an estimate of the fiber orientation distribution functions (pliODF) from high-resolution 3D-PLI vector data. However, this method introduces angular errors by discretizing the directional histogram (DH), which limits the spherical harmonics (SH) expansion order. In this work, we propose to improve the angular resolution by making use of the Laplace-Beltrami (LB) operator to regularize the SH coefficients which define the fiber ODF at higher orders.

Methods

pliODFs: Axer et al. [2] introduced an estimate of the fiber ODF derived from 3D-PLI high-resolution vector data. Their approach consists of 1. the definition of super-voxels to downsample the high-resolution data, 2. the creation of a normalized directional histogram on a unit sphere from discretized distribution of fiber orientation vectors in each super-voxel, and 3. the use of spherical harmonics expansion to approximate the directional histogram within each super-voxel: $h(\theta, \phi) = \sum_{l=0}^{L_{max}} \sum_{m=-l}^l c_{lm} Y_l^m(\theta, \phi)$ where c_{lm} are the coefficients of the truncated SH Y_l^m of maximum order L_{max} and phase factor m . In matrix format, the problem is $H = BC$ where C is the coefficients vector, B is the SH basis matrix, and H is the normalized DH entries. The least-square solution for C needs B to be invertible even at high L_{max} , which is an inherent limitation of this approach.

Laplace-Beltrami regularized fiber ODF: We therefore propose to use higher SH orders and to regularize the corresponding SH coefficients, which define more accurately the fiber ODF h , by using the Laplace-Beltrami operator Δ_b . This LB operator satisfies the relation $\Delta_b Y_l^m = -l(l+1)Y_l^m$. It sharpens the fiber ODF [3] and consequently improves the angular precision. The solution of the regularized SH coefficients writes $C = (B^T B + \lambda L)^{-1} B^T H$ where L denotes the regularization matrix and λ its weight.

Experiments

To evaluate the performance of our approach, we apply our implementation to the simulated dataset as in [2] and directly compare the results to those of *pliODF* by Axer *et al.* Fig.1 displays a zoomed compartment (a) mimicking a crossing fiber configuration. This compartment corresponds to a super-voxel composed of $40 \times 40 \times 1$ native voxels representing three prevailing fiber orientation populations. Recall that each native voxel contains a single fiber orientation. The proportions of the fiber populations in this super-voxel are as follows: 25% (in blue) oriented in $(\theta, \phi) = (90^\circ, 0^\circ)$, 25% (magenta) in $(-45^\circ, 0^\circ)$ and 50% (cyan) in $(45^\circ, 90^\circ)$. The SH order is fixed to $L_{max} = 6$ for *pliODF* in (b) and $L_{max} = [8, 10, 12]$ with $\lambda = 2e-5$ for our regularized fiber ODF. From the results, the LB regularized fiber ODF give a higher angular resolution and better estimates of the volume fractions of the fiber populations as shown in (c), (d) and (e).

Conclusion

We propose an analytical Laplace-Beltrami regularization process of the SH coefficients which enables us to describe the fiber ODF in 3D-PLI. The experiments show that the LB regularized ODF enhances each underlying fiber compartment and considerably improves the extraction of fibers. This opens the door to integration with diffusion MRI across scales.

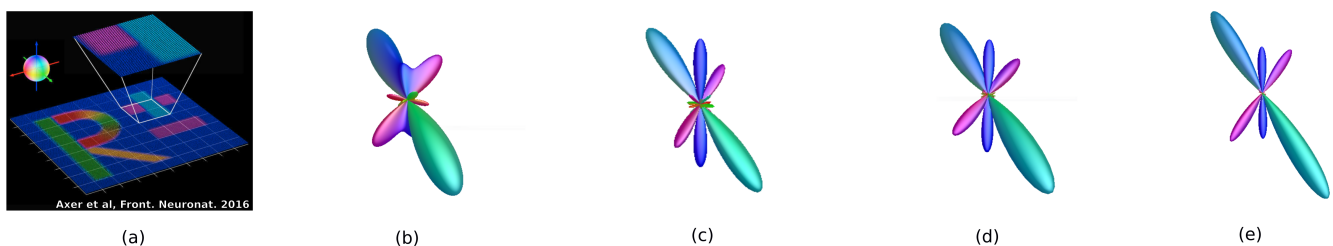


Figure 1: Fiber ODF estimates. (a) ground truth super-voxel containing $40 \times 40 \times 1$ native voxels with three prevailing fiber orientations. (b) 6th order *pliODF* reproduced from [2]. (c), (d) and (e) represent 8th, 10th and 12th order Laplace-Beltrami regularized fiber odf.

Acknowledgments: This work was partly supported by ANR ”MOSIFAH” under ANR-13-MONU-0009-01, the ERC under the European Union’s Horizon 2020 research and innovation program (ERC Advanced Grant agreement No 694665:CoBCoM).

References [1] Axer M *et al*, *Neuroimage*, vol. 54, no. 2, pp. 10911101, 2011. [2] Axer M *et al*, *Frontiers in neuroanatomy*, vol. 10, 2016. [3] Descoteaux M *et al*, *Magnetic Resonance in Medicine*, vol. 58, Issue 3, pp. 497-510, 2007.

Appendix B

Synthetic Data Generation

The nerve fiber model imitates two fiber bundles in the XY-plan crossing at an angle X which varies from 0° to 90° , with 10° increments. To build this configuration, the following steps were performed:

1. Two initial fiber bundles with a length of $3840 \mu m$ and a radius of $640 \mu m$ were placed at an crossing angle X .
2. These initial fiber bundles were then filled with smaller fiber bundles with a radius of $64 \mu m$, on which the collision algorithm (Matuschke et al., 2019) was performed for 25 steps, to allow a ‘macroscopic’ weave pattern.
3. The resulting fiber bundles were then filled one last time with fibers with a radius of $10 \mu m$. In this state, each fiber is spatially divided into $20 \mu m$ segments. To limit the curvature of each fiber, the minimum radius of a bending fiber is limited to $40 \mu m$.

This configuration runs with the collision solving algorithm until no collision are detected.

The resulting fiber configuration, for instance as pictured in Fig. 6.2A where $X = 90^\circ$, is then used for the 3D-PLI simulation to generate the resulting FOM. For the simulation, the model is discretized on a volume of $3840 \times 3840 \times 600 \mu m^3$ to allow the calculations performed by *simPLI* (Dohmen et al., 2015; Menzel et al., 2015). Each fiber is modelled as a filled cylindrical object with an absorption coefficient $\mu = 1/mm^3$ and a birefringence $\Delta n = -0.001$. The deriving microscopic images have a in-plane resolution of $60 \times 60 \mu m^2$. The signal noise was calculated with a gain factor of $g = 3$ (see (Schmitz et al., 2018)) and an initial light intensity of $26000 a.u.$ The signal from the 3D-PLI pipeline is then analyzed to calculate the FOM.

Appendix C

Publications

Journal publication

Alimi, A., Deslauriers-Gauthier, S., Matuschke, F., Schmitz, D., Axer, M., Deriche, R.: Analytical and Fast Fiber Orientation Distribution Reconstruction in 3D Polarized Light Imaging. (**Submitted Medical Image Analysis**)

Conference proceedings

Alimi, A., Deslauriers-Gauthier, S., Deriche, R.: Quantitative assessment of multi-scale Tractography: bridging the resolution gap with 3D-Polarized Light Imaging, ISMRM 2020 - International Society for Magnetic Resonance in Medicine, 2020, Sydney, Australia. (**Digital poster**) [Link to paper](#)

Alimi, A., Deslauriers-Gauthier, S., Deriche, R.: Towards validation of diffusion MRI tractography: bridging the resolution gap with 3D Polarized Light Imaging, ISMRM 2019 - International Society for Magnetic Resonance in Medicine, M 2019, Montreal, Canada. (**Oral presentation**) [Link to paper](#)

Alimi, A., Deslauriers-Gauthier, S., Matuschke, F., Schmitz, D., Axer, M., Deriche, R.: Analytical Fiber ODF Reconstruction in 3D PolarizedLight Imaging: Performance Assessmen. ISBI 2018-IEEE International Symposium on Biomedical Imaging, 2019, Venice, Italy. (**Poster**) [Link to paper](#)

Alimi, A., Usson, Y., Jouk, P.S., Michalowicz, G., Deriche, R.: An analytical fiber ODF reconstruction in 3D Polarized Light Imaging. ISBI 2018-IEEE International Symposium on Biomedical Imaging, 2018, Washington D.C., USA. (**Oral presentation**) [Link to paper](#)

Alimi, A., Pizzolato, M., Fick, RHJ., Deriche, R.: Solving the inclination sign ambiguity in three-dimensional Polarized Light Imaging with a PDE-based method. ISBI 2017-IEEE International Symposium on Biomedical Imaging, 2017, Melbourn, Australia. (**Oral presentation**) [Link to paper](#)

Alimi, A., Deslauriers-Gauthier, S., Deriche, R.: Regularizing the ODF estimate with the Laplace-Baltrami operator in Polarized Light Imaging. CoBCoM 2017-Computational Brain Connectivity Mapping Winter School Workshop, 2017, Juan-les-Pins, France. **(Poster)** [Link to poster](#)

Publications not directly related to the contributions presented in this thesis.

Alimi, A., Fick, F., Wassermann, D., Deriche, R.: Dmipy, a Diffusion Microstructure Imaging toolbox in Python to improve research reproducibility. MICCAI 2018 – Workshop on Computational Diffusion MRI, Sep 2018, Granada, Spain. **(Poster)** [Link to paper](#)

Alimi, A., Petiet, A., Santin, M., Philippe, A.C., Lehericy, S., Deriche, R., Wassermann, D.: Towards the assessment of myelination using time-dependent diffusion MRI indices. Joint Annual Meeting ISMRM-ESMRMB 2018, Paris Expo Porte de Versailles, Paris, France. **(Poster)** [Link to paper](#)

Petiet A., Genovese G., **Alimi**, A., Palombo M., Santini M., Felfli M., Abdoukader N., Langui D., Aigrot M-S. Millecamps A., Philippe A-C., Lehericy S., Branzoli F., Wassermann D., Baron A., Stankoff B.: Validation of new MRI markers of white matter microstructure in cuprizone mice. Multiple Sclerosis (MS) Conference 2018, Paris, France.

Award

Magna Cum Laude Award for the work entitled: “Towards Validation of Diffusion MRI Tractography: Bridging the Resolution Gap with 3D-Polarized Light Imaging” at the 27th Annual ISMRM Meeting – Montreal, Canada 2019

Bibliography

- Daniel C Alexander. Multiple-fiber reconstruction algorithms for diffusion mri. *White Matter in Cognitive Neuroscience: Advances in Diffusion Tensor Imaging and Its Applications*, 1064:113–133, 2005.
- Abib Alimi, Samuel Deslauriers-Gauthier, and Rachid Derich. Regularizing the ODF estimate with the Laplace-Beltrami operator in 3D Polarized Light Imaging. CoBCoM 2017 - Computational Brain Connectivity Mapping Winter School Workshop, November 2017a. URL <https://hal.inria.fr/hal-01659253>.
- Abib Alimi, Marco Pizzolato, Rutger HJ Fick, and Rachid Deriche. Solving the inclination sign ambiguity in three dimensional polarized light imaging with a pde-based method. In *2017 IEEE 14th International Symposium on Biomedical Imaging (ISBI 2017)*, pages 737–740. IEEE, 2017b.
- Abib Alimi, Alexandra Petiet, Mathieu Santin, Anne-Charlotte Philippe, Stéphane Lehéricy, Rachid Deriche, and Demian Wassermann. Towards the assessment of myelination using time-dependent diffusion mri indices. 2018a.
- Abib Alimi, Yves Ussou, Pierre-Simon Jouk, Gabrielle Michalowicz, and Rachid Deriche. An analytical fiber odf reconstruction in 3d polarized light imaging. In *2018 IEEE 15th International Symposium on Biomedical Imaging (ISBI 2018)*, pages 1276–1279. IEEE, 2018b.
- Abib Alimi, S Deslauriers-Gauthier, F Matuschke, D Schmitz, M Axer, and R Deriche. Analytical fiber odf reconstruction in 3d polarized light imaging: Performance assessment. In *ISBI 2019-IEEE International Symposium on Biomedical Imaging*, 2019a.
- Abib Alimi, Samuel Deslauriers-Gauthier, and Rachid Deriche. Towards validation of diffusion mri tractography: bridging the resolution gap with 3d polarized light imaging. In *ISMRM 2019 - International Society for Magnetic Resonance in Medicine*, 2019b. URL <https://hal.inria.fr/hal-02070912>.
- Abib Alimi, Matteo Frigo, Samuel Deslauriers-Gauthier, and Rachid Deriche. Quantitative assessment of multi-scale tractography: bridging the resolution gap with 3d-polarized

- light imaging. In *ISMRM 2020 - International Society for Magnetic Resonance in Medicine*, 2020.
- Abib OY Alimi, Samuel Deslauriers-Gauthier, and Rachid Deriche. Regularizing the ODF estimate with the Laplace-Beltrami operator in 3D Polarized Light Imaging. CoBCoM 2017 - Computational Brain Connectivity Mapping Winter School Workshop, November 2017c. URL <https://hal.inria.fr/hal-01659253>.
- Yaniv Assaf, Heidi Johansen-Berg, and Michel Thiebaut de Schotten. The role of diffusion mri in neuroscience. *NMR in Biomedicine*, 32(4):e3762, 2019.
- Markus Axer, Katrin Amunts, David Grässel, Christoph Palm, Jürgen Dammers, Hubertus Axer, Uwe Pietrzyk, and Karl Zilles. A novel approach to the human connectome: ultra-high resolution mapping of fiber tracts in the brain. *Neuroimage*, 54(2):1091–1101, 2011a.
- Markus Axer, David Grässel, Melanie Kleiner, Jürgen Dammers, Timo Dickscheid, Julia Reckfort, Tim Hütz, Björn Eiben, Uwe Pietrzyk, Karl Zilles, et al. High-resolution fiber tract reconstruction in the human brain by means of three-dimensional polarized light imaging. *Frontiers in neuroinformatics*, 5:34, 2011b.
- Markus Axer, Sven Strohmer, David Gräßel, Oliver Bücken, Melanie Dohmen, Julia Reckfort, Karl Zilles, and Katrin Amunts. Estimating fiber orientation distribution functions in 3d-polarized light imaging. *Frontiers in neuroanatomy*, 10:40, 2016.
- Peter J Basser, James Mattiello, and Denis LeBihan. Mr diffusion tensor spectroscopy and imaging. *Biophysical journal*, 66(1):259–267, 1994.
- Richard S Bear and Francis O Schmitt. The optics of nerve myelin. *JOSA*, 26(5):206–212, 1936.
- Christian Beaulieu. The basis of anisotropic water diffusion in the nervous system—a technical review. *NMR in Biomedicine: An International Journal Devoted to the Development and Application of Magnetic Resonance In Vivo*, 15(7-8):435–455, 2002.
- Max Born and Emil Wolf. *Principles of optics: electromagnetic theory of propagation, interference and diffraction of light*. Elsevier, 2013.
- Paul T. Callaghan. *Principles of nuclear magnetic resonance microscopy*. Oxford University Press on Demand, 1993.
- Paul T Callaghan, CD Eccles, and Y Xia. Nmr microscopy of dynamic displacements: k-space and q-space imaging. *Journal of Physics E: Scientific Instruments*, 21(8):820, 1988.

- David B Chenault and Russell A Chipman. Measurements of linear diattenuation and linear retardance spectra with a rotating sample spectropolarimeter. *Applied optics*, 32(19):3513–3519, 1993.
- RA Chipman. Polarimetry handbook of optics vol 2, 2nd edn, ed m bass, 1995.
- Moo K Chung, Hyekyoung Lee, Victor Solo, Richard J Davidson, and Seth D Pollak. Topological distances between brain networks. In *International Workshop on Connectomics in Neuroimaging*, pages 161–170. Springer, 2017.
- Edward Collett. Field guide to polarization. Spie Bellingham, WA, 2005.
- Peter Craven and Grace Wahba. Smoothing noisy data with spline functions. *Numerische mathematik*, 31(4):377–403, 1978.
- Alessandro Daducci, Erick Jorge Canales-Rodrı, Maxime Descoteaux, Eleftherios Garyfallidis, Yaniv Gur, Ying-Chia Lin, Merry Mani, Sylvain Merlet, Michael Paquette, Alonso Ramirez-Manzanares, et al. Quantitative comparison of reconstruction methods for intra-voxel fiber recovery from diffusion mri. *IEEE transactions on medical imaging*, 33(2):384–399, 2014.
- Benedicto de Campos Vidal, Maria Luiza Silveira Mello, Alberto Costa Caseiro-Filho, and Carlos Godo. Anisotropic properties of the myelin sheath. *Acta histochemica*, 66(1):32–39, 1980.
- Flavio Dell’Acqua and J-Donald Tournier. Modelling white matter with spherical deconvolution: How and why? *NMR in Biomedicine*, 32(4):e3945, 2019.
- Flavio Dell’Acqua, Giovanna Rizzo, Paola Scifo, Rafael Alonso Clarke, Giuseppe Scotti, and Ferruccio Fazio. A model-based deconvolution approach to solve fiber crossing in diffusion-weighted mr imaging. *IEEE Transactions on Biomedical Engineering*, 54(3):462–472, 2007.
- Rachid Deriche and Olivier Faugeras. Les edp en traitement des images et vision par ordinateur. 1995.
- Maxime Descoteaux. *High angular resolution diffusion MRI: from local estimation to segmentation and tractography*. PhD thesis, 2008.
- Maxime Descoteaux, Elaine Angelino, Shaun Fitzgibbons, and Rachid Deriche. Regularized, fast, and robust analytical q-ball imaging. *Magnetic resonance in medicine*, 58(3):497–510, 2007.
- Maxime Descoteaux, Rachid Deriche, Thomas R Knosche, and Alfred Anwander. Deterministic and probabilistic tractography based on complex fibre orientation distributions. *IEEE transactions on medical imaging*, 28(2):269–286, 2008.

- Samuel Deslauriers-Gauthier and Pina Marziliano. Sampling signals with a finite rate of innovation on the sphere. *IEEE Transactions on Signal Processing*, 61(18):4552–4561, 2013.
- Samuel Deslauriers-Gauthier, Pina Marziliano, Michael Paquette, and Maxime Descoteaux. The application of a new sampling theorem for non-bandlimited signals on the sphere: Improving the recovery of crossing fibers for low b-value acquisitions. *Medical image analysis*, 30:46–59, 2016. doi: 10.1016/j.media.2016.01.002.
- Paul Audain Desrosiers. *Simulation de l’imagerie en lumière polarisée: Application à l’étude de l’architecture des “fibres” du myocarde humain*. PhD thesis, INSA de Lyon, 2014.
- Thijs Dhollander, Louise Emsell, Wim Van Hecke, Frederik Maes, Stefan Sunaert, and Paul Suetens. Track orientation density imaging (todi) and track orientation distribution (tod) based tractography. *NeuroImage*, 94:312–336, 2014.
- Melanie Dohmen. *Towards the Reconstruction of Fiber Tracts in the Human Brain by Means of 3D Polarized Light Imaging*. PhD thesis, Universität Wuppertal, Fakultät für Mathematik und Naturwissenschaften . . . , 2013.
- Melanie Dohmen, Miriam Menzel, Hendrik Wiese, Julia Reckfort, Frederike Hanke, Uwe Pietrzyk, Karl Zilles, Katrin Amunts, and Markus Axer. Understanding fiber mixture by simulation in 3d polarized light imaging. *NeuroImage*, 111:464–475, 2015.
- Philippe Douek, Robert Turner, James Pekar, Nichoias Patronas, and Denis Le Bihan. Mr color mapping of myelin fiber orientation. *J Comput Assist Tomogr*, 15(6):923–929, 1991.
- A Einstein. Über die von der molekularkinetischen theorie der wärme geforderte bewegung von in ruhenden flüssigkeiten suspendierten teilchen ann. phys. 17 549–560; english translation in: Einstein a 1956 investigations on the theory of the brownian movement, 1905.
- Albert Einstein. *Investigations on the Theory of the Brownian Movement*. Courier Corporation, 1956.
- Shawna Farquharson, J-Donald Tournier, Fernando Calamante, Gavin Fabinyi, Michal Schneider-Kolsky, Graeme D Jackson, and Alan Connelly. White matter fiber tractography: why we need to move beyond dti. *Journal of neurosurgery*, 118(6):1367–1377, 2013.
- Rutger HJ Fick, Demian Wassermann, Emmanuel Caruyer, and Rachid Deriche. Mapl: Tissue microstructure estimation using laplacian-regularized map-mri and its application to hcp data. *NeuroImage*, 134:365–385, 2016.

- Gabriel Girard, Kevin Whittingstall, Rachid Deriche, and Maxime Descoteaux. Towards quantitative connectivity analysis: reducing tractography biases. *Neuroimage*, 98:266–278, 2014.
- Gustaf Fredrik Göthlin. *Die doppelbrechenden Eigenschaften des Nervengewebes: ihre Ursachen und ihre biologischen Konsequenzen*. Almqvist & Wiksells Boktryckeri, 1913.
- Henry Gray. *Anatomy of the human body*, volume 8. Lea & Febiger, 1878.
- Patric Hagmann, Lisa Jonasson, Philippe Maeder, Jean-Philippe Thiran, Van J Wedeen, and Reto Meuli. Understanding diffusion mr imaging techniques: from scalar diffusion-weighted imaging to diffusion tensor imaging and beyond. *Radiographics*, 26(suppl_1):S205–S223, 2006.
- Claudia Hänel, Ali C Demiralp, Markus Axer, David Gräbel, Bernd Hentschel, and Torsten W Kuhlen. Interactive level-of-detail visualization of 3d-polarized light imaging data using spherical harmonics. 2017.
- Per Christian Hansen. The l-curve and its use in the numerical treatment of inverse problems. 1999.
- Dennis M Healy Jr, Harrie Hendriks, and Peter T Kim. Spherical deconvolution. *Journal of Multivariate Analysis*, 67(1):1–22, 1998.
- Eugene Hecht. Optics 4th edition. optics. *Addison Wesley Longman Inc*, 1:1998, 1998.
- Alan Hylton, Gregory Henselman-Petrusek, Janche Sang, and Robert Short. Tuning the performance of a computational persistent homology package. *Software: Practice and Experience*, 49(5):885–905, 2019.
- Ben Jeurissen, Alexander Leemans, Jacques-Donald Tournier, Derek K Jones, and Jan Sijbers. Investigating the prevalence of complex fiber configurations in white matter tissue with diffusion magnetic resonance imaging. *Human brain mapping*, 34(11):2747–2766, 2013.
- Ben Jeurissen, Jacques-Donald Tournier, Thijs Dhollander, Alan Connelly, and Jan Sijbers. Multi-tissue constrained spherical deconvolution for improved analysis of multi-shell diffusion mri data. *NeuroImage*, 103:411–426, 2014.
- Ben Jeurissen, Maxime Descoteaux, Susumu Mori, and Alexander Leemans. Diffusion mri fiber tractography of the brain. *NMR in Biomedicine*, 32(4):e3785, 2019.
- Heidi Johansen-Berg and Timothy EJ Behrens. *Diffusion MRI: from quantitative measurement to in vivo neuroanatomy*. Academic Press, 2013.
- Derek K Jones. *Diffusion mri*. Oxford University Press, 2010.

- R Clark Jones. A new calculus for the treatment of optical systems. description and discussion of the calculus. *Josa*, 31(7):488–493, 1941.
- P-S Jouk, Yves Usson, Gabrielle Michalowicz, and Laurence Grossi. Three-dimensional cartography of the pattern of the myofibres in the second trimester fetal human heart. *Anatomy and embryology*, 202(2):103–118, 2000.
- Pierre-Simon Jouk, Yves Usson, Gabrielle Michalowicz, and Franck Parazza. Mapping of the orientation of myocardial cells by means of polarized light and confocal scanning laser microscopy. *Microscopy research and technique*, 30(6):480–490, 1995.
- Jülich Supercomputing Centre. JURECA: General-purpose supercomputer at Jülich Supercomputing Centre. *Journal of large-scale research facilities*, 2, A62, 2016.
- Melanie Kleiner, Markus Axer, David Gräßel, Julia Reckfort, Uwe Pietrzyk, Katrin Amunts, and Timo Dickscheid. Classification of ambiguous nerve fiber orientations in 3d polarized light imaging. In *International Conference on Medical Image Computing and Computer-Assisted Intervention*, pages 206–213. Springer, 2012.
- Luiza Larsen, Lewis D Griffin, David GRäßel, Otto W Witte, and Hubertus Axer. Polarized light imaging of white matter architecture. *Microscopy research and technique*, 70(10):851–863, 2007.
- Denis Le Bihan and Heidi Johansen-Berg. Diffusion mri at 25: exploring brain tissue structure and function. *Neuroimage*, 61(2):324–341, 2012.
- Denis Le Bihan, Eric Breton, Denis Lallemand, Philippe Grenier, Emmanuel Cabanis, and Maurice Laval-Jeantet. Mr imaging of intravoxel incoherent motions: application to diffusion and perfusion in neurologic disorders. *Radiology*, 161(2):401–407, 1986.
- Hyekeyoung Lee, Hyejin Kang, Moo K Chung, Bung-Nyun Kim, and Dong Soo Lee. Persistent brain network homology from the perspective of dendrogram. *IEEE transactions on medical imaging*, 31(12):2267–2277, 2012.
- Alexander Leemans. Diffusion mri of the brain: The naked truth. *NMR in Biomedicine*, 32(4):e4084, 2019.
- Bradley J MacIntosh, Simon J Graham, and P Eng. Magnetic resonance imaging to visualize stroke and characterize stroke recovery: a review. *Frontiers in neurology*, 4: 60, 2013.
- Klaus H Maier-Hein, Peter F Neher, Jean-Christophe Houde, Marc-Alexandre Côté, Eleftherios Garyfallidis, Jidan Zhong, Maxime Chamberland, Fang-Cheng Yeh, Ying-Chia Lin, Qing Ji, et al. The challenge of mapping the human connectome based on diffusion tractography. *Nature communications*, 8(1):1349, 2017.

- Felix Matuschke, Kévin Ginsburger, Cyril Poupon, Katrin Amunts, and Markus Axer. Dense fiber modeling for 3d-polarized light imaging simulations, 2019.
- Miriam Menzel. *Finite-difference time-domain simulations assisting to reconstruct the brain's nerve fiber architecture by 3D polarized light imaging*. PhD thesis, RWTH Aachen University, 2018.
- Miriam Menzel, Kristel Michielsen, Hans De Raedt, Julia Reckfort, Katrin Amunts, and Markus Axer. A jones matrix formalism for simulating three-dimensional polarized light imaging of brain tissue. *Journal of the Royal Society Interface*, 12(111):20150734, 2015.
- Miriam Menzel, Julia Reckfort, Daniel Weigand, Hasan Köse, Katrin Amunts, and Markus Axer. Diattenuation of brain tissue and its impact on 3d polarized light imaging. *Biomedical optics express*, 8(7):3163, 2017.
- Susumu Mori and Peter CM Van Zijl. Fiber tracking: principles and strategies—a technical review. *NMR in Biomedicine: An International Journal Devoted to the Development and Application of Magnetic Resonance In Vivo*, 15(7-8):468–480, 2002.
- Susumu Mori, Barbara J Crain, Vadappuram P Chacko, and Peter CM Van Zijl. Three-dimensional tracking of axonal projections in the brain by magnetic resonance imaging. *Annals of Neurology: Official Journal of the American Neurological Association and the Child Neurology Society*, 45(2):265–269, 1999.
- Michael E Moseley, Yoram Cohen, J Kucharczyk, J Mintorovitch, HS Asgari, MF Wendland, J Tsuruda, and D Norman. Diffusion-weighted mr imaging of anisotropic water diffusion in cat central nervous system. *Radiology*, 176(2):439–445, 1990.
- Hans Mueller. Memorandum on the polarization optics of the photoelastic shutter. *Report of the OSRD project OEMsr-576*, 2, 1943.
- Evren Özarlan, Cheng Guan Koay, Timothy M Shepherd, Michal E Komlos, M Okan İrfanoğlu, Carlo Pierpaoli, and Peter J Basser. Mean apparent propagator (map) mri: a novel diffusion imaging method for mapping tissue microstructure. *NeuroImage*, 78: 16–32, 2013.
- LA Pajdzik and AM Glazer. Three-dimensional birefringence imaging with a microscope tilting-stage. i. uniaxial crystals. *Journal of applied crystallography*, 39(3):326–337, 2006.
- Geoffrey JM Parker, Hamied A Haroon, and Claudia AM Wheeler-Kingshott. A framework for a streamline-based probabilistic index of connectivity (pico) using a structural interpretation of mri diffusion measurements. *Journal of Magnetic Resonance Imaging: An Official Journal of the International Society for Magnetic Resonance in Medicine*, 18(2):242–254, 2003.

- Greg D Parker, David Marshall, Paul L Rosin, Nicholas Drage, Stephen Richmond, and Derek Kenton Jones. A pitfall in the reconstruction of fibre odds using spherical deconvolution of diffusion mri data. *Neuroimage*, 65:433–448, 2013.
- David Raffelt, J-Donald Tournier, Stuart Crozier, Alan Connelly, and Olivier Salvado. Reorientation of fiber orientation distributions using apodized point spread functions. *Magnetic Resonance in Medicine*, 67(3):844–855, 2012.
- Julia Reckfort, Hendrik Wiese, Uwe Pietrzyk, Karl Zilles, Katrin Amunts, and Markus Axer. A multiscale approach for the reconstruction of the fiber architecture of the human brain based on 3d-PLI. *Frontiers in Neuroanatomy*, 9, September 2015. doi: 10.3389/fnana.2015.00118. URL <https://doi.org/10.3389/fnana.2015.00118>.
- Francois Rheault, Etienne St-Onge, Jasmeen Sidhu, Klaus Maier-Hein, Nathalie Tzourio-Mazoyer, Laurent Petit, and Maxime Descoteaux. Bundle-specific tractography with incorporated anatomical and orientational priors. *NeuroImage*, 186:382–398, 2019.
- Leonid I Rudin, Stanley Osher, and Emad Fatemi. Nonlinear total variation based noise removal algorithms. *Physica D: nonlinear phenomena*, 60(1-4):259–268, 1992.
- Heinrich Sachs. *Das Hemisphärenmark des menschlichen Grosshirns: Der Hinterhauptlappen. Mit einem Vorwort von C. Wernicke*. G. Thieme, 1892.
- Kurt Schilling, Vaibhav Janve, Yurui Gao, Iwona Stepniewska, Bennett A Landman, and Adam W Anderson. Comparison of 3d orientation distribution functions measured with confocal microscopy and diffusion mri. *Neuroimage*, 129:185–197, 2016.
- Daniel Schmitz, Sascha EA Muenzing, Martin Schober, Nicole Schubert, Thomas Lippert, Katrin Amunts, and Markus Axer. Derivation of fiber orientations from oblique views through human brain sections in 3d-polarized light imaging. *Frontiers in neuroanatomy*, 12:75, 2018.
- Ann E Sizemore, Chad Giusti, Ari Kahn, Jean M Vettel, Richard F Betzel, and Danielle S Bassett. Cliques and cavities in the human connectome. *Journal of computational neuroscience*, 44(1):115–145, 2018.
- Robert E Smith, Jacques-Donald Tournier, Fernando Calamante, and Alan Connelly. Anatomically-constrained tractography: improved diffusion mri streamlines tractography through effective use of anatomical information. *Neuroimage*, 62(3):1924–1938, 2012.
- Robert E Smith, Jacques-Donald Tournier, Fernando Calamante, and Alan Connelly. Sift2: Enabling dense quantitative assessment of brain white matter connectivity using streamlines tractography. *Neuroimage*, 119:338–351, 2015.

- Edward O Stejskal and John E Tanner. Spin diffusion measurements: spin echoes in the presence of a time-dependent field gradient. *The journal of chemical physics*, 42(1):288–292, 1965.
- EO Stejskal. Use of spin echoes in a pulsed magnetic-field gradient to study anisotropic, restricted diffusion and flow. *The Journal of Chemical Physics*, 43(10):3597–3603, 1965.
- J-Donald Tournier. Diffusion mri in the brain–theory and concepts. *Progress in Nuclear Magnetic Resonance Spectroscopy*, 2019.
- J-Donald Tournier, Fernando Calamante, David G Gadian, and Alan Connelly. Direct estimation of the fiber orientation density function from diffusion-weighted mri data using spherical deconvolution. *NeuroImage*, 23(3):1176–1185, 2004.
- J-Donald Tournier, Fernando Calamante, and Alan Connelly. Robust determination of the fibre orientation distribution in diffusion mri: non-negativity constrained super-resolved spherical deconvolution. *Neuroimage*, 35(4):1459–1472, 2007.
- J-Donald Tournier, Chun-Hung Yeh, Fernando Calamante, Kuan-Hung Cho, Alan Connelly, and Ching-Po Lin. Resolving crossing fibres using constrained spherical deconvolution: validation using diffusion-weighted imaging phantom data. *Neuroimage*, 42(2):617–625, 2008.
- J Donald Tournier, Fernando Calamante, and Alan Connelly. Improved probabilistic streamlines tractography by 2nd order integration over fibre orientation distributions. In *Proceedings of the international society for magnetic resonance in medicine*, volume 18, page 1670. ISMRM, 2010.
- J-Donald Tournier, Fernando Calamante, and Alan Connelly. Mrtrix: diffusion tractography in crossing fiber regions. *International journal of imaging systems and technology*, 22(1):53–66, 2012.
- J-Donald Tournier, Robert Smith, David Raffelt, Rami Tabbara, Thijs Dhollander, Maximilian Pietsch, Daan Christiaens, Ben Jeurissen, Chun-Hung Yeh, and Alan Connelly. Mrtrix3: A fast, flexible and open software framework for medical image processing and visualisation. *NeuroImage*, page 116137, 2019.
- David S Tuch. Q-ball imaging. *Magnetic resonance in medicine*, 52(6):1358–1372, 2004.
- David S Tuch, Timothy G Reese, Mette R Wiegell, Nikos Makris, John W Belliveau, and Van J Wedeen. High angular resolution diffusion imaging reveals intravoxel white matter fiber heterogeneity. *Magnetic Resonance in Medicine: An Official Journal of the International Society for Magnetic Resonance in Medicine*, 48(4):577–582, 2002.

- Francesco Vergani, Sajedha Mahmood, Cristopher M Morris, Patrick Mitchell, and Stephanie J Forkel. Intralobar fibres of the occipital lobe: a post mortem dissection study. *Cortex*, 56:145–156, 2014.
- Lihui Wang. *Modeling and simulation of diffusion magnetic resonance imaging for cardiac fibers*. PhD thesis, INSA de Lyon, 2013.
- Van J Wedeen, Patric Hagmann, Wen-Yih Isaac Tseng, Timothy G Reese, and Robert M Weisskoff. Mapping complex tissue architecture with diffusion spectrum magnetic resonance imaging. *Magnetic resonance in medicine*, 54(6):1377–1386, 2005.
- Hendrik Wiese. *Enhancing the Signal Interpretation and Microscopical Hardware Concept of 3D Polarized Light Imaging*. PhD thesis, University of Wuppertal, 2016.
- Hendrik Wiese, David Gräßel, Uwe Pietrzyk, Katrin Amunts, and Markus Axer. Polarized light imaging of the human brain: a new approach to the data analysis of tilted sections. In *Polarization: Measurement, Analysis, and Remote Sensing XI*, volume 9099, page 90990U. International Society for Optics and Photonics, 2014.
- Mauro Zucchelli, Samuel Deslauriers-Gauthier, and Rachid Deriche. A computational framework for generating rotation invariant features and its application in diffusion mri. *Medical Image Analysis*, 60:101597, 2020.